UNIVERSITÀ DEGLI STUDI DI TRENTO
DIPARTIMENTO DI FISICA

LOCALIZATION AND SPREADING

OF MATTER WAVES

IN DISORDERED POTENTIALS

Ph.D. thesis by
Marco Larcher

A Sandra e Lino, i miei genitori.

Contents

Introduction

Disorder is ubiquitous in nature and affects the properties of many physical systems. A deep understanding of its effects is therefore of fundamental importance. This is particularly true for quantum systems, where disorder can influence dramatically the transport properties of electrons leading to a phenomenon that today is known as Anderson localization [1]. This type of localization is a subtle effect that arises from an interference process due to coherent multiple scattering from the disorder. It leads to a complete absence of diffusion and to exponentially localized single-particle wavefunctions [2]. Anderson's discovery represented a breakthrough in the study of transport properties of quantum particles, since it introduced a completely new approach to the problem. Previous theories of transport considered disorder just as a weak perturbation, predicting a diffusive motion determined by incoherent scattering [3].

Shortly after the discovery of Anderson localization it has been shown that, in one dimensional systems, localization takes place for all quantum states [4, 5]. This is counterintuitive especially when the energy of a given state is much larger than the typical energy fluctuations associated to the disorder. A proper understanding of localization in higher dimensions required more time, but nowadays it is finally accepted that also in two dimensional systems all states are localized, while in three dimensions a metal-insulator transition can occur, as already suggested by Anderson in his original paper [6, 7].

The phenomenon of Anderson localization has been originally introduced in the context of electrons propagating in disordered solid state materials. Only later it has been realized that the same type of localization also occurs with classical waves, such as light or sound [8, 9]. This led to the first observations of Anderson localization in optics [10, 11] and acoustics [12].

Nowadays the study of Anderson localization is still a very active research field. Since its discovery many issues have been discussed and understood, but there are also several important questions that are still open. Few years ago a new boost to the study of Anderson localization and the related open problems have been given by experiments with ultracold atoms. Since the realization of the first Bose-Einstein condensate with dilute and cold gases [13, 14, 15], the experimental techniques aimed to manipulating and observing these quantum gases in different geometries have been enormously improved; at present, ultracold atoms can be considered as a benchmark for the study of many phenomena in the realm of quantum physics. Among the first examples of remarkable results obtained in this field are the observation of interference fringes in the expansion of two overlapping Bose-Einstein condensates

[16] and the formation of quantized vortices [17]. More recently a great interest is focused on properties of many-body systems, where new quantum phases can emerge. Examples are the observation of a Tonks-Girardeau gas in one dimension [18, 19] or the transition from superfluid to Mott insulator [20].

The great success of ultracold atoms is mostly due to the high degree of control that can be reached in experiments [21]. Both bosonic and fermionic atoms can be cooled down to degeneracy and external trapping potentials can be used to control the dimensionality of the system. Feshbach resonances are used to tune the interaction between atoms and many different observables can be detected ranging from the atomic density to the momentum distribution. Laser light can be used to design different kind of potentials for the atoms, such as perfect periodic optical lattices in different dimensionalities [22].

Recently optical potentials have been used also for the generation of controlled random potentials [23] and a new field of study started with the first direct observation of Anderson localization of matter waves in two different research groups [24, 25]. This observation represented a remarkable result and showed that ultracold atoms can represent a powerful experimental tool for exploring a number of problems related to the theory of localization [26, 27, 28].

In this thesis we will concentrate on two main issues, namely the interplay between localization and interaction in disordered systems and the problem of localization in correlated random potentials. The former is a long standing problem that has been raised shortly after the discovery of Anderson localization [29], because of its fundamental importance in electron transport in disordered solids, where Coulomb interaction between electrons can not be neglected. One naively expects that interaction acts against localization, but a detailed study of this interplay is highly nontrivial. The study of the role played by correlations in the localization process is also of great interest, since, strictly speaking, in real world uncorrelated potentials do not exist. It is known that correlations can lead to delocalization effects, however, a full understanding is still missing and one of the most challenging questions is whether or not they can introduce a metal-insulator transition already in one dimension, where the effect of disorder is known to be the strongest [30]. The possibility to design different kind of disordered potentials and to control the interatomic interactions are the two key features that makes ultracold atoms particularly suitable to tackle these two problems.

1.1 Outline of the thesis

The main objective of this thesis is to give a contribution to the understanding of the physics of disordered systems studying, from a theoretical and numerical point of view, problems and models that can be directly investigated in feasible experiments with ultracold atoms. As we have previously anticipated the main two topics that we will investigate are the role played by interactions and correlations in the determination of the localization properties of disordered quantum systems.

The outline of the thesis is the following :

○ In chapter 2 we present the basic concepts of the theory of localization of quantum particles in disordered systems. We introduce the phenomenon of Anderson localization and the concept of mobility edge in three dimensional systems. We discuss the role played by the dimensionality in relation to the problem of localization with special focus to the one dimensional case, that is the most relevant for this thesis. We introduce different models of disorder and discuss their implementations with ultracold atomic gases. Finally we review the experimental observations of Anderson localization.

○ In chapter 3 the problem of localization in quasiperiodic systems is discussed. After introducing the Aubry-André model and explaining in detail its connection with ultracold atoms in bichromatic optical lattices, we review its localization properties. We then consider the spreading of an initially localized wavepaket, both in real and momentum space, as a possible tool to study the localization properties of the Aubry-André model. Special attention is given to properties which are observable in experiments. Part of the results presented in this chapter are published in:

M. Larcher, F. Dalfovo, and M. Modugno, "Effects of interaction on the diffusion of atomic matter waves in one-dimensional quasiperiodic potentials", *Physical Review A*, **80**, 053606 (2009) [31].
M. Larcher, M. Modugno, and F. Dalfovo, "Localization in momentum space of ultracold atoms in incommensurate lattices", *Physical Review A*, **83**, 013624 (2011) [32]

○ Chapters 4 is devoted to the study of the effects of interaction on the spreading of an ultracold atomic gas in a bichromatic optical lattice. This is done by considering a discretized mean-field equation, which generalizes the Aubry-André model by adding a nonlinear term that includes the interaction between atoms. This model is also known as discrete nonlinear Schrödinger equation (DNLS). We solve this equation numerically and analyze the interplay between two competing effects of the interaction, namely, self-trapping and destruction of Anderson localization. Finally we compare the numerical results that can be extracted from this model with experimental measurements performed in Florence. The results of this chapter have been published in the first paper mentioned above as well as in:

E. Lucioni, B. Deissler, L. Tanzi, G. Roati, M. Zaccanti, M. Modugno, M. Larcher, F. Dalfovo, M. Inguscio, and G. Modugno, "Observation of subdiffusion in a disordered interacting system", *Physical Review Letters*, **106**, 230403 (2011) [33].

○ The focus of chapter 5 is still on the interplay between localization and interaction. We use again the DNLS model to tackle this problem, but here

more attention is devoted to the investigation of the spreading behaviour of wavepackets, that were localized in the noninteracting case. We characterize in detail the phenomenon of destruction of Anderson localization and the resulting subdiffusive expansion induced by the interaction, identifying different spreading regimes and predicting the associated spreading laws. Finally an extensive numerical analysis is performed and the results are compared with the theoretical expectations. The content of this chapter has been published in:

M Larcher, T. Laptyeva, J. Bodyfelt, F. Dalfovo, M. Modugno and S. Flach, "Subdiffusion of nonlinear waves in quasiperiodic potentials", *New Journal of Physics*, **14**, 103036 (2012) [34].

○ In chapter 6 we propose a model of disorder that can be realized experimentally using dipolar ultracold gases and that presents correlation properties that leads to interesting delocalization effects. The model is first introduced and its statistical properties are characterized. In particular we show that both short and long correlations are naturally present in the disordered system that we propose. We then study its localization properties calculating the localization length of the eigenstates by means of an exact renormalization-decimation technique. Using these results, we discuss the role of short and long range correlations and their interplay. The material in this chapter is the basis for a paper which will be soon submitted:

M. Larcher, C. Menotti, B. Tanatar and P. Vignolo, "A metal-insulator transition induced by random dipoles", *in preparation* [35].

Localization properties in disordered quantum systems

It was first realized by Anderson that disorder can have a dramatic impact on the transport properties of a quantum particle. More precisely, by studying the conductance of electrons in solids, he discovered that disorder can lead to a complete absence of diffusion and a consequent metal-insulator transition. This phenomenon is known as Anderson localization [1]. Since the revolutionary discovery by Anderson a huge activity on the physics of quantum disordered system has started and nowadays it is still an active research field that involves many areas of physics [36, 26].

This chapter is devoted to the introduction of the localization problem in disordered quantum systems. We will review some basic concepts that will form the background for the understanding of the results presented in the others chapters of this thesis. In section 2.1 we outline the main achievements of the theory of localization for noninteracting quantum particles and classical waves. In section 2.2 we specialize to the localization properties of one dimensional systems, which is the dimensionality that we will consider for the rest of this thesis. In section 2.3 we review the experimental observations of Anderson localization with a special focus on the localization of matter waves and ultracold atomic systems.

2.1 Disorder induced localization

In this section we present some of the key results of the quantum theory of localization. There are a number of interesting introductions to this field that can be found in the scientific literature (see for instance [37, 3, 38, 36, 39]).

In particular we first introduce the problem of quantum transport in disordered systems from a comparison with the classical case. We then present the concepts of Anderson localization and of mobility edge and discuss the role played by the dimensionality of the system starting from the results of the scaling theory of localization. Finally we introduce some models of disorder in connection with the field of ultracold atomic gases.

Classical vs. Quantum

We start to deal with the problem of the behaviour of a quantum particle in a disordered potential considering a comparison with the classical case. This can
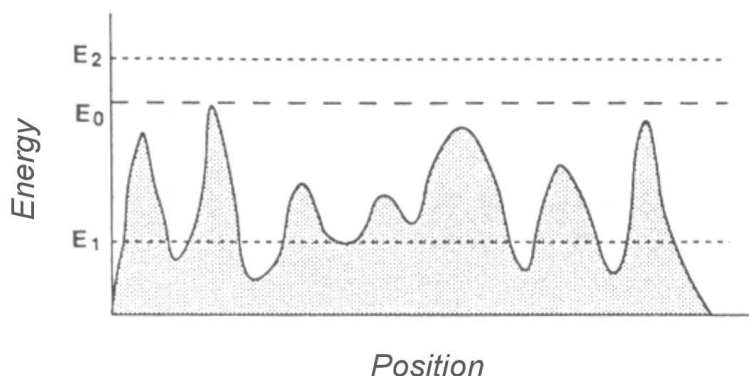
Figure 2.1: *Localization properties of a classical particle in a disordered potential depending on the value of its energy. If the energy of the particle is smaller than the highest barriers of the potential ($E_1 < E$) the motion of the particle is restricted to a finite region of space. Conversely if the energy of the particle is larger than the highest barriers of the potential ($E_2 > E_0$) the motion of the particle is unbounded and it will propagate through the disordered potential. Figure taken from Ref. [2].*

give an intuition of why the study of Anderson localization is highly nontrivial and introduces the two main effects that play a key role for the determination of the transport behaviour of a quantum particle.

Let us consider a classical particle in a disordered potential $V(x)$ (we considered the one dimensional case for simplicity) like the one that is depicted in Fig. 2.1 and let us consider the situation where the potential is upper bounded by a maximum value that we call E_0. The behaviour of the classical particle can be easily determined by a simple comparison of the energy of the particle with the maximum value assumed by the potential. In particular if the energy of the particle is smaller than E_0 the motion will be bounded in a finite region of space between two barriers of the potential, transport over long distances is suppressed and localization takes place. On the contrary if the energy is larger than E_0 the particle will fly above the barriers of the disordered potential and on average the motion will be ballistic.

For a quantum particle, where the wave nature of matter comes into play, this simple picture is completely modified. On the one hand a quantum particle can tunnel through potential barriers and therefore we do not expect that a disordered potential can bound and freeze its motion. This delocalization due to tunneling is what happens, for instance, in periodic potentials, where, no matter how high are the potential barriers, but the particle will always propagate ballistically [40]. On the other hand, even if a quantum particle has an energy much larger than the typical potential barriers, we know that there will always be a finite reflection and transmission probability. This can lead to nontrivial interference effects that tend to localize particles. We will see that an example of localization due to interference

is Anderson localization [1, 2].

Anderson localization

The effects of disorder on the propagation of quantum particles has been initially studied in the context of condensed matter physics for the description of the propagation of electrons in solids. The natural starting point for the analysis of this problem is a perfect crystal, whose properties are well known and are governed by the Bloch theorem. In particular the eigenstates of the system are extended Bloch waves that can propagate through the crystal [40].

The traditional view, before the discovery of Anderson localization, considered as a starting point for the study of the effects of disorder the extended waves of a perfect crystal [36]. As a consequence in the semiclassical theory of electronic transport, electrons are still considered as waves whose wavefunction remains extended throughout the sample but the propagation is modified by incoherent scattering due to the presence of disorder in the system. The result of these collisions causes a loss of the phase coherence of the waves on the length of the mean free path ℓ. This leads to a diffusive motion of electrons through the disordered potential, which allows electrons to propagate to infinity and results in a finite conductance of the sample. An increase of the strength of the disorder leads to a decrease of the mean free path ℓ and to a consequent decrease of the diffusion constant and of the conductance of the sample. This turns out to be true when interference effects can be neglected.

The first to understand that interference effects play a key role for the determination of the transport behaviour of a quantum particle was Philip Anderson in 1958. He showed that the consequence of these destructive interference processes between different scattered waves is not a simple reduction of the conductivity but a complete absence of diffusion [1].

In his seminal paper he considered the transport of a particle (spin) in a discretized lattice that can tunnel via quantum jumps between different sites and disorder is introduced by requiring that the on-site energies associated with the different lattice sites varies randomly. More precisely Anderson introduced the following model for the description of the propagation of the particle (spin)

$$i\frac{\partial \psi_j}{\partial t} = \varepsilon_j \psi_j - \sum_{k \neq j} J_{j,k} \psi_k \tag{2.1}$$

where ψ_j is the probability amplitude that a particle is on site j, $J_{j,k}$ describes the hopping amplitude between different sites and ε_j are the random on-site energies characterized by a probability distribution $P(\varepsilon)$.

He considered the transport problem of an initially localized probability distribution $|\psi_j(0)|$ that occupies just a finite region of space and he tried to answer the following question: "how fast, if at all, does the probability distribution diffuse away from its initial position?" He found that if the hopping amplitude $J_{j,k}$ falls off faster

than $1/|j-k|^3$ and if the disorder W is strong enough if compared with the average value of the hopping amplitude J then there will be a complete absence of diffusion. The initial amplitude $|\psi_j(0)|$ stays localized around the initially occupied sites and falls off exponentially with the distance.

This absence of diffusion is associated with the fact that the single-particle eigenstates of a disordered system are exponentially localized if disorder is strong enough [3]. More precisely, this means that, on the average, the envelopes of their amplitudes are exponentially decaying in space at infinity

$$|\phi(\vec{r})| \sim e^{-|\vec{r}-\vec{r}_o|/L_{loc}} \tag{2.2}$$

where $\vec{r}_0$ is the localization center and L_{loc} is the localization length. Particle described by these kind of states cannot contribute to transport since they occupy a finite region of space in opposition to particles in extended states that can escape to infinity. Therefore the main two manifestations of Anderson localization, which are closely connected, are the absence of diffusion and the fact that the single particle eigenstates are exponentially localized.

Mobility edge

Anderson already understood that complete localization takes place only if the disorder is strong enough [1]. In this situation all the single particle eigenstates are localized. Below a certain disorder strength, instead, localization takes place only for a fraction of states while the remaining states are extended.

Ten years after the publication of the paper by Anderson, Mott introduced the concept of *mobility edge* [6] which represents an energy which separates localized and extended states. He understood that no localized states can exist in an energy region of extended states with the following argument. Assume that it is possible to
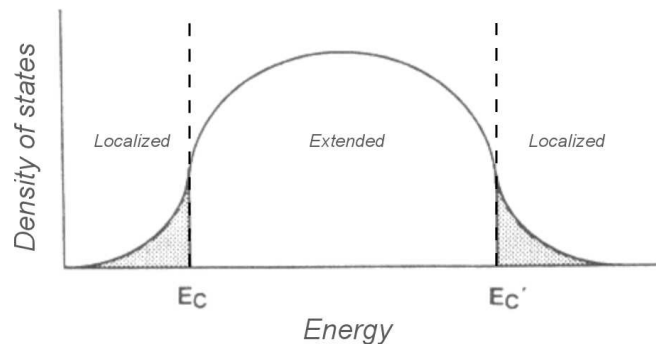
Figure 2.2: *Schematic representation of the concept of mobility edge. The states are localized in energy regions where the density of states is small $E < E_c$ and $E > E_c'$. Conversely they are extended in energy regions where the density of states is large. The two energies E_c and E_c' represent the mobility edges of the system.*
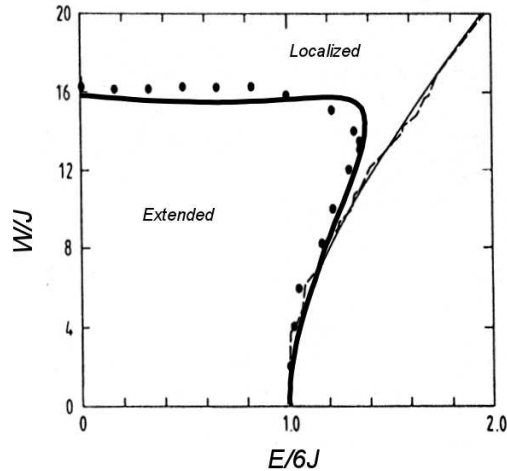
Figure 2.3: *Phase diagram for the three dimensional Anderson model as a function of the disorder stength W and of the energy of the states E. The states in the spectrum of the system are divided in two regions and can be extended or localized. The points and the thick solid line represents the mobility edge, i.e. the critical energy that separates these two regions of the spectrum. More precisely the points are the result of an exact numerical calculation, while the thick solid line is the outcome of the self consistent theory of localization. The thin line indicates the position of the upper edge of the spectrum, only the region on the left of this line belongs to the spectrum. Figure taken from Ref. [41].*

find a localized state and an extended state with infinitely close energies for a given configuration of disorder, then an infinitesimal change of the configuration would hybridize them, forming two extended states. Hence, for a given energy, almost all states should be either localized or extended.

In Fig. 2.2 we show a pictorial view of the concept of mobility edge for a tight binding model similar to Eq. (2.1). The vertical dashed lines represent the position of the two mobility edges E_c and E'_c while the solid line represents the density of states of the system. The regions with the localized states are those where the density of states is small. As the disorder strength is increased the mobility edges move towards the band center and eventually, for a critical value of the disorder strength, they meet at the center of the band. Above this critical value of disorder there are no more extended states in the system.

In Fig. 2.3 we instead show a quantitative calculation of the mobility edge for the model considered by Anderson in its original paper. The phase diagram reported in Fig. 2.3 shows the localized or extended nature of the states depending on their energy E and on the strength of the disorder W. The points are extracted from an exact numerical calculation and represent the mobility edge, i.e. the energy that divide extended and localized states. The thick line is the result for the mobility edge given by an approximate theory. The thin line

indicates instead the upper bound of the spectrum. This quantitative calculation confirms the qualitative picture that we have just described. One can see that as the disorder strength is increased the localized states appear at the edge of the spectrum and then move gradually towards the center of the band. Above $W/J \approx 16$, which represents the critical disorder strength for the three dimensional Anderson model under consideration, there are only localized states in the spectrum.

Role of dimensionality: scaling theory

The dimensionality of the system, d, plays a rather important role for the determination of the localization properties of a quantum disordered system. In particular one of the main results of the theory of localization is that in one dimensional (1D) and two dimensional (2D) systems all the single particle eigenstates are exponentially localized while in three dimensions (3D) both extended and localized states can exist.

This result has been first suggested by Abrahams, Anderson, Licciardello and Ramakrishnan who gave a first formulation of the so called *one-parameter scaling theory of localization* [7]. A scaling theory describes the relevant properties of a physical system under a change of size $L \to bL$ ($b > 1$).

In particular Abrahams *et al.* introduced a dimensionless conductance $g = G\hbar/e^2$ by noting that the conductance G of a sample is dimensionless once is expressed in units of $e^2/\hbar$. They described the behaviour of the dimensionless con-
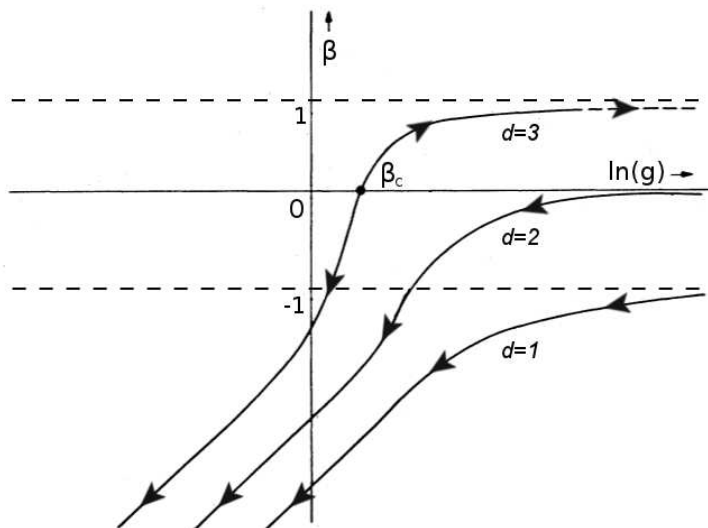
Figure 2.4: *The scaling function $\beta(g)$ in dimensions $d = 1, 2, 3$. The dimensionless conductance g grows with the size of the system L if $\beta > 0$ but decreases for $\beta < 0$. For $d = 3$ a critical point exists where $\beta = 0$; this correspond to the presence of a transition from a localized regime to an extended regime.*

ductance of a hypercube of size L^d as a function of the system size L by defining its logarithmic derivative

$$\beta = \frac{d \ln g}{d \ln L}. \tag{2.3}$$

and assuming that it depends only on the dimensionless conductance itself and not on the other microscopic properties of the sample. This is the main assumption at the basis of the theory and it is known as the one parameter scaling hypothesis. The behaviour of $\beta(g)$ is qualitatively obtained by Abrahams *et al.* starting from the two limiting behaviours for strong and weak disorder. In particular for weak disorder the classical (i.e. without interference) behaviour of the conductance g is assumed. This corresponds to the Ohm's law namely the conductance depends on the surface $A = L^{d-1}$ of the sample and on its length L according to

$$g \sim \sigma \frac{A}{L} = \sigma L^{d-2} \tag{2.4}$$

where σ is the conductivity of the sample, which is an intensive quantity independent on the system size. In the opposite limit of strong disorder, exponential localization is assumed in all dimensions and therefore conductivity is also expected to decay exponentially with the system size

$$g \sim e^{-L/L_{loc}}. \tag{2.5}$$

From Eqs. (2.4) and (2.5) one obtains

$$\beta(g) \sim \begin{cases} d-2 & \text{weak disorder} \\ \ln g + const. & \text{strong disorder} \end{cases} \tag{2.6}$$

Interpolating between the two limiting behaviours and assuming that $\beta(g)$ is a continuous and monotonically increasing function one obtains the result depicted in Fig. (2.4). If $\beta(g) > 0$ the value of the dimensionless conductance increases with the system size, one is therefore in the extended/conducting regime. Conversely for $\beta(g) < 0$ the conductance decreases with the system size and one ends up in the localized/insulating regime where $g \to 0$. The presence of a fixed point g_c where $\beta(g_c) = 0$ signals the presence of a transition from an extended to a localized regime. One can see from Fig. (2.4) that such a transition exits in the 3D case. This is consistent with the results on the presence of a mobility edge in the general three dimensional case that we have previously discussed earlier in this chapter. In the 1D and 2D case the theory does not predict the presence of fixed points and $\beta(g)$ is always smaller than zero. This means that no extended regime can exist for $d = 1, 2$ and one has always Anderson localization, no matter how small is the disorder strength.

The qualitative shape of the diagram first proposed by Abrahams *et al.* and that we presented in Fig. (2.4) was confirmed quantitatively few years later by an extrapolation from the weak disordered limit [42].

Models of disorder

Disorder can be introduced in a variety of different ways in a physical system. Here we just mention few models of disorder that are closely related with the Hamiltonians that can be experimentally realized using ultracold atoms.

In the most general case, let us assume that a single particle is governed by the Hamiltonian

$$H = -\frac{\hbar^2}{2m}\nabla^2 + V(\vec{r}) \tag{2.7}$$

where $V(\vec{r})$ is a quenched disordered potential, i.e. a static disordered potential that does not evolve in time. The random potential is defined by a probability distribution $P(V)$ and by a set of correlation functions $\langle V(\vec{r_1})V(\vec{r_2})\ldots V(\vec{r_n})\rangle$. Here we indicated with $\langle\ldots\rangle$ an average over many different disorder realizations. A disorder realization is a particular outcome of the process of choosing the potential value $V(\vec{r})$ for all the values of $\vec{r}$. The disordered potential is usually assumed to be spatially homogeneous in the sense that its statistical properties do not depend on the specific position in the system. As a consequence the average value of the potential $\langle V\rangle$ does not depend on $\vec{r}$ and in general the n-point correlation function depends only on $n-1$ relative coordinates only $C_n(\vec{r_1}, \vec{r_2}, \ldots, \vec{r_n})$. In particular the two point correlation function, which we simply indicate with $C(\vec{r})$, depends only on one variable:

$$C(\vec{r}) = \langle V(\vec{r_0} + \vec{r})V(\vec{r_0})\rangle. \tag{2.8}$$

In atomic gases Hamiltonian (2.7) can be realized using an optical speckle potential [43, 44, 45, 24]. Optical potentials can be created using laser light that induces an atomic dipole moment and a consequent dipolar force on the atoms which is proportional to the intensity of the laser field [21, 22]. The speckle pattern, in particular, is produced by shining a coherent laser beam through a ground-glass plate which is then focused on the atoms using a converging lens. The ground-glass plate transmits the laser light without altering the intensity, but imprints a random phase profile on the emerging light. Then, the electric field $E(\vec{r})$ on the focal plane results from the coherent superposition of many independent waves with equally distributed random phases. This result is a random pattern of the transmitted light that directly translates in a disordered potential $V(\vec{r})$ for the atoms. Both the modulus and sign of $V(\vec{r})$ can be controlled experimentally by changing the light intensity and the detuning of the laser frequency with respect to the atomic transition. A detailed analysis of the statistical properties of a typical speckle potentials used for ultracold gases experiments can be found in [46, 47]

Disorder can be also introduced in a natural way by using a perfect lattice as a starting point. A typical example of a lattice Hamiltonian with compositional disorder is provided by

$$H = \sum_j \varepsilon_j \mid j\rangle\langle j\mid + \sum_{j,k} J_{j,k}\mid j\rangle\langle k\mid \tag{2.9}$$

where ε_j are the on-site energies while $J_{j,k}$ describe the hopping between different sites of the lattice. The diagonal part of the Hamiltonian corresponds to the potential energy and the non-diagonal part to the kinetic energy in the continuous space description (2.7). Let us note that the time dependent Schrödinger equation associated to Hamiltonian (2.9) corresponds to the model considered by Anderson in his original paper (2.1) [1]. Disorder can be introduced by taking the site energies or the hopping terms at random. Also in this case one characterizes the disorder by means of a probability distribution and a set of correlation functions. A typical choice in the study of disordered system is

$$P(\varepsilon) = \begin{cases} 1/W & \text{if} \quad |\varepsilon| < W/2 \\ 0 & \text{otherwise} \end{cases} \quad (2.10)$$

and constant hopping J restricted just to nearest neighbouring sites. In this case Hamiltonian (2.9) is indicated as the Anderson model.

A discretized space for ultracold atoms can be produced again using an optical field [21, 22]. In this case, two counterpropagating laser beams are used. Due to the interference between the two laser beams, an optical standing wave is formed, in which atoms can be trapped. In this way the atoms feel the presence of a perfect one dimensional optical lattice. Adding a pair of lasers also in the other directions gives the possibility to create optical lattices in 2D and 3D. If the laser field is strong enough one creates a deep optical lattice and enters the so called *tight binding regime*. In this regime the space can be discretized and the atoms are governed by an Hamiltonian which is very similar to (2.9) but with contant on site energies $\varepsilon_j = \varepsilon$ and typically the hopping term is approximated to be constant and different from zero only on nearest neighbouring sites $J_{j,k} = J$ [1] [21, 48]. At this point disorder can be introduced by randomly shifting the on-site energies. This might be done by superimposing a speckle potential to the optical lattice. Another possibility is to introduce another optical lattice with a different lattice spacing with respect to the first one [49, 25]. This realizes a bichromatic optical lattice and introduces a shift of the on-site energy which is not fully random but still very interesting from the point of view of the localization properties. We will discuss more in detail these kind of systems, which are called quasiperiodic, in chapter 3.

Another interesting proposal for the creation of a disordered potential for ultracold atoms is to use a mixture of two different atomic species (or two different internal states of the same atom) [50, 51]. The atoms of one of the two species are trapped at random positions in the wells of a very deep optical lattice. As a consequence their dynamic is frozen and they cannot tunnel between different sites. These trapped atoms play the role of "impurities". The other species instead feels the presence of a weaker optical lattice or it does not feel the lattice at all and it is therefore free to move. This atomic species play the role of "test particle". Due to the interaction between the two atomic species, the test particles feel a random

---

[1] A detailed derivation of a tight binding Hamiltonian similar to (2.9) starting from a deep periodic potential will be given in section 3.1.

potential formed by the impurities which are trapped in the optical lattice. This model can be described with a free space Hamiltonian similar to (2.7) if the test particles do not feel the optical lattice. Conversely if also the test particle feel the presence of the lattice (although much shallower that the lattice felt by the impurities) a tight binding Hamiltonian (2.9) is used for the description of the system. A detailed analysis of an impurity model will be given in chapter 6.

2.2   One dimensional disordered systems

One dimensional systems play a key role in the understanding of the physics of disorder [52, 53, 2]. First of all, it is the dimensionality where disorder have stronger effects, moreover many properties of the eigenstates and related to transport can be discussed rigorously. Finally numerical calculations are faster and easier to implement.

In 1D localization is always expected no matter how strong the random potential is. Mott and Twose [54] were the first who suggested that all the single particle eigenstates might be exponentially localized in 1D but they just provided a qualitative argument to support their statement. The first rigorous proof of this result has been given by Borland [5] few years later. Nowadays the conclusion that all single particle states are localized in a 1D random potentials is well established as it has been obtained with a variety of different methods.

A standard way to prove localization in 1D is to use random matrix techniques developed by Oseledec and Furstenberg in the sixties for the calculation of the Lyapunov exponent, which is the inverse of the localization length

$$\Lambda = \frac{1}{L_{loc}} \tag{2.11}$$

Consider the eigenvalue problem associated to the one dimensional Anderson model (2.9)

$$- J(\psi_{j+1} + \psi_{j-1}) + \varepsilon_j \psi_j = E \psi_j \tag{2.12}$$

with $\psi_j = \langle j \mid \psi \rangle$. Equation (2.12) is equivalent to

$$\Psi_j = M_j \Psi_{j-1}, \tag{2.13}$$

where Ψ_j represents a two component vector and M_j a 2×2 matrix

$$\Psi_j = \begin{pmatrix} \psi_j \\ \psi_{j+1} \end{pmatrix} \qquad M_j = \begin{pmatrix} 0 & 1 \\ -1 & (\varepsilon_j - E)/J \end{pmatrix}. \tag{2.14}$$

By using this relation recursively, one can show that the vector Ψ_j, for large values of j, is determined by a product of a series of random matrices M_j similar to the one that we have defined in (2.14), that is $\Psi_j = M_j \ldots M_2 M_1 \Psi_0$. Two theorems by Furstenberg [55] and Oseledec [56] are used to determine the behaviour of the product of the random matrices. They state that, for almost all realizations of the
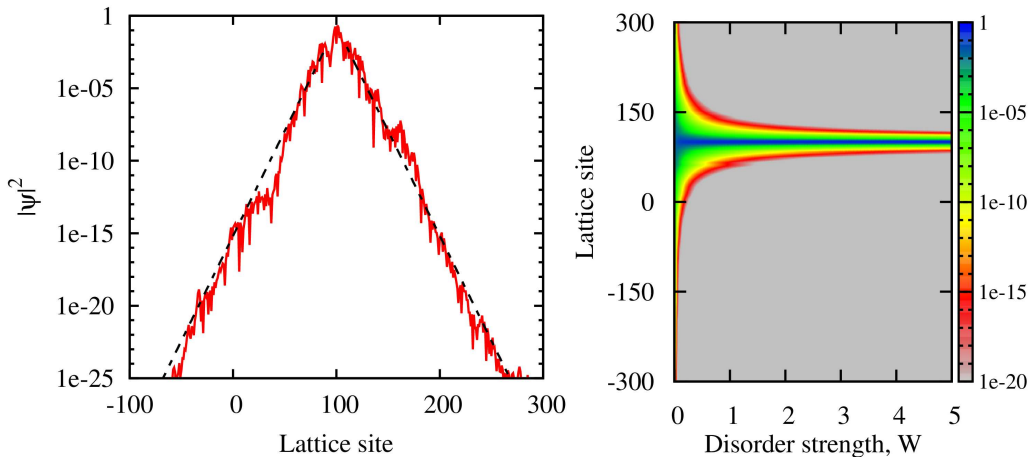
Figure 2.5: *Localized eigenstates of the one dimensional Anderson model obtained by direct numerical diagonalization. In the left panel we show an example of state with energy close to the center of the band $E \approx 0$ for $W = 4$. The state has a typical exponentially decaying profile. The localization length obtained numerically is in agreement with the one obtained with the approximate expression (2.16) (black dashed line). In the right panel we show the ground state of the system for increasing disorder strength W.*

random potential, an initial vector Ψ_j grows or decays asymptotically as $e^{\pm\Lambda(E)j}$, where $\Lambda(E)$ is a positive, non-random quantity that is known as the Lyapunov exponent. The solution at energy E is an exponentially localized solution of the spectrum only when there are two vectors $\Psi_0^{\pm}$ that decay respectively for $j \to +\infty$ and $j \to -\infty$ and that coincide at some site. This assures the existence of a solution of energy E that decays exponentially on both sides of the system with localization length $L_{loc}(E) = 1/\Lambda(E)$. If these two vectors do not exist for a given energy E, this energy does not belongs to the spectrum of the system.

The eigenvalue problem defined by Eq. (2.14) can also be solved numerically by direct diagonalization. The result of a numerical diagonalization of Eq. (2.12) with on-site energies given by (2.10) is shown in Fig. 2.5. In particular in the left panel of the figure we show the shape of a typical localized eigenstate close to the center of the band for a disorder strength $W = 4$. The linear decay of the envelope of the wavefunction in semi-log scale is a clear signature of the exponential localization. In the right panel one can see how the ground state of the system changes as the disorder strength is increased. With a color density plot we show that already for very small values of the disorder strength the ground state has a localized profile that decays exponentially on both sides of the system. As the disorder strength W is increased the localization becomes stronger, the localization length becomes smaller and consequently the regions of space occupied by the ground state is reduced.

A very useful relation that connects the spectral properties of a 1D system to

the localization properties of the eigenstates was first derived by Herbert and Jones [57] in the case of the Anderson model and subsequently it has been generalized by Thouless [58]. This relation is

$$\Lambda(E) = \int_{-\infty}^{\infty} \ln(E - E')\rho(E') \, dE' \tag{2.15}$$

where $\Lambda(E)$ is the Lyapunov exponent and $\rho(E)$ the density of states. When applied to Eq. (2.12) with ε_l uniformly distributed in $[-W/2, W/2]$ and in second order perturbation theory, Eq. (2.15) gives [59]

$$\Lambda(E) = \frac{(W/J)^2}{24[4 - (E/J)^2]}. \tag{2.16}$$

This relation is valid for small W and results in a localization length at the center of the band equal to $L_{loc}(E = 0) = 96J^2/W^2$. States situated at the center of the band, i.e. with energy $E = 0$, are thus localized on longer length scales.

The result of the perturbation theory can be compared with the direct numerical diagonalization. This is done in Fig. 2.5 where the two black dashed lines represent an exponential decay with localization length given by (2.16). The result that the localization length diverges as W^{-2} for small W is a general result in one dimensional system and does not apply only to the case of the Anderson model.

2.3   Experimental observations of Anderson localization

Anderson localization was initially introduced for noninteracting quantum particles [1], but its observation remained elusive for many years. It was lately realized that Anderson localization is actually ubiquitous in wave physics, and therefore it can be applied also to classical waves such as light or sound [9, 36]. This paved the way for the first observations of Anderson localization. Localization of classical waves has been reported so far for ultrasounds [12, 60], for electromagnetic waves propagating in "free space" in the microwaves regime [10, 61] as well as in the optical regime [11, 62, 63] and for light in photonic crystals [64, 65, 66].

The first direct observation of Anderson localization of matter waves in real space has been reported in experiments with ultracold gases [24, 25]. These systems have some important advantages. In most of the experiments with classical waves, for instance, absorption mechanisms are almost unavoidable, producing decay processes whose effects are hardly separable form the effects of Anderson localization. Moreover the propagation of classical waves usually takes place in solid materials which have to be engineered in order to contain a controlled amount of disorder. In practice, this is often complicate and significantly reduces the possibility to change the relevant parameters, such as the strength of the disorder, at will. Conversely, ultracold atoms offer the advantage that light can be used to create optical disordered potentials for the atoms, with almost negligible absorption effects. In addition the disorder strength can be easily changed on a wide range of values simply varying
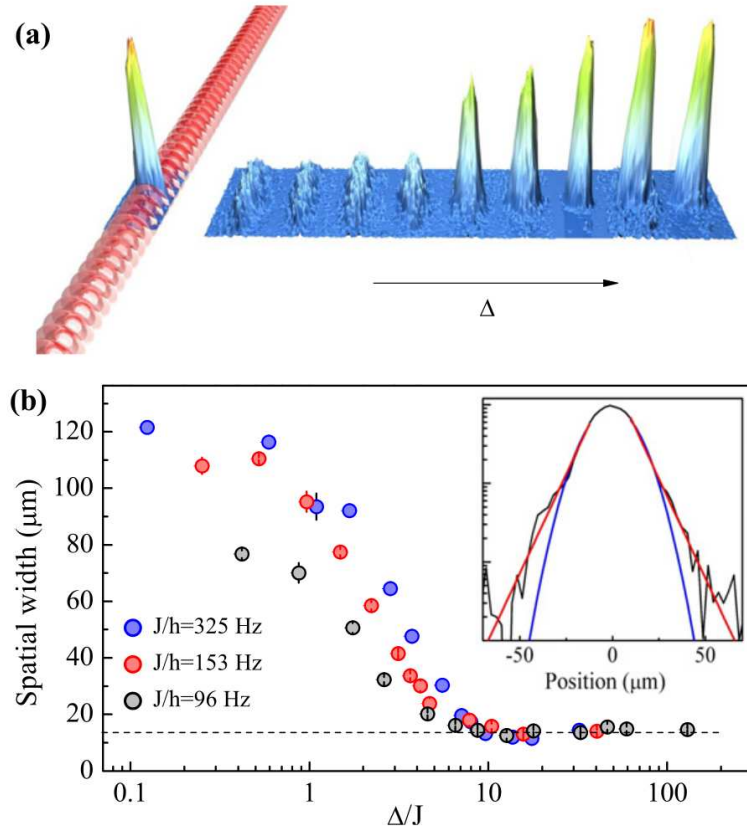
Figure 2.6: *(a) Schematic representation of the expansion of an ultracold atomic gas in a bichromatic optical lattice, as realized in Ref. [25]. The condensate is initially confined in a finite region of space (left) and then its released along the quasiperiodic potential. As the strength of the secondary lattice (which plays the role of disorder strength) is increased the size of the condensate after a fixed expansion time is reduced (right). (b) Axial size of the condensate after 700 ms of expansion as a function of the strength of the secondary lattice for different values of the tunneling energy J. Inset: typical exponentially decaying profile of the atomic cloud in the regime of localization. Figure taken from Ref. [27].*

the intensity of the laser field which produces the external potential for the atoms. The use of Feshbach resonances allows one to control the interatomic interaction by applying an external magnetic field. Another advantage is that one can directly measures different observables: in situ absorption imaging gives the possibility to directly detect the square modulus of the wavefunction, correlations measurements can be performed and the momentum distribution of the atoms can be observed thanks to time of flight measurements. Finally the dimensionality of the system can be controlled using strong confinements in one or two directions.

As said before, ultracold atoms lead to the first observation of Anderson local-
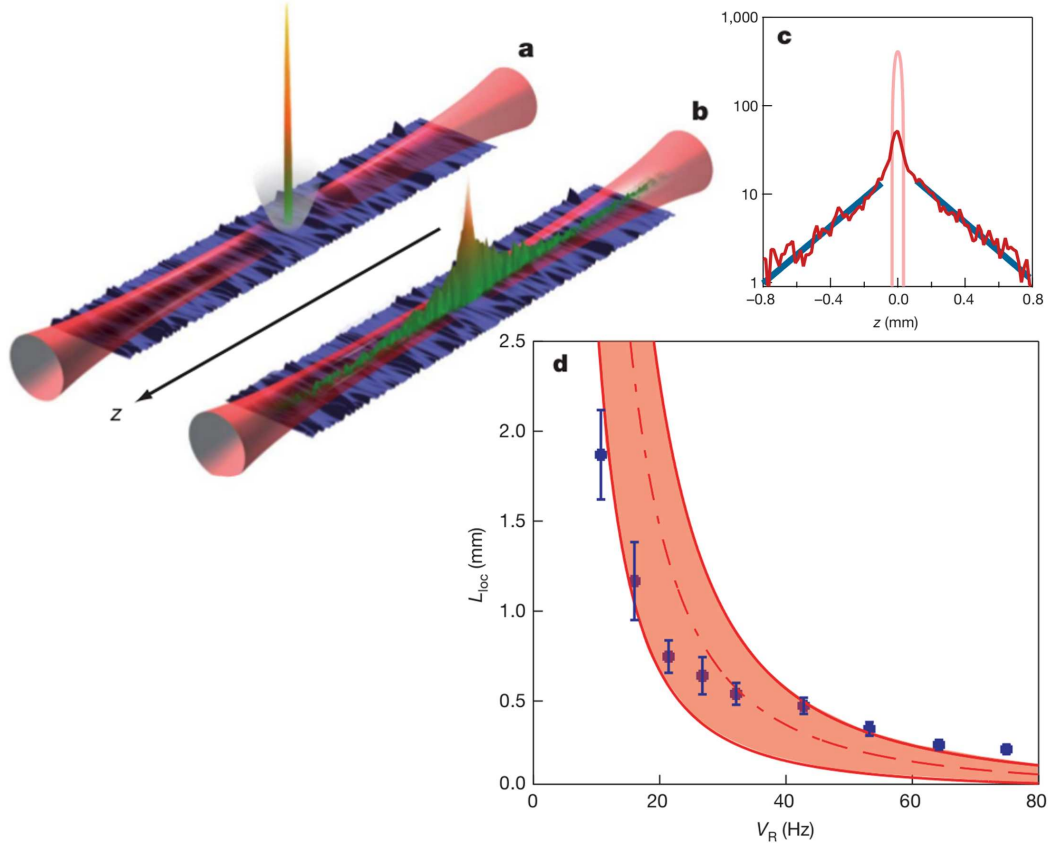
Figure 2.7: *(a), (b) Cartoon of the typical experimental procedure of Ref. [24]. The atomic cloud is initially confined by an harmonic confinement and then it is suddenly released into the speckle potential. (c) Density profiles of the localized atomic cloud one second after its release, the exponential nature of the localization is clearly observed. (d) Localization length L_{loc} fitted from the measured profiles as a function of the disorder strength. The shaded area represents the theoretical prediction with the relative uncertainty deriving from the estimation of the experimental parameters. Figure taken from Ref. [24]*

ization of matter waves. In particular the first experiments considered a one dimensional setup and introduced disorder using a bichromatic lattice [25] or a speckle potential [24]. In both experiments, one of the key elements was the study of the expansion of an initially localized cloud. The condensate is initially created into an harmonic trap that confines the atoms in a limited region of space. Then the harmonic confinement is suddenly switched off and the atoms are let free to expand in the disordered potential. These two stages of the experimental procedure are schematically represented in Fig. 2.6 (a) for a bichromatic optical lattices and in Fig. 2.7 (a), (b) for a speckle potential. The expansion of the atomic cloud along a given direction can be monitored by in situ absorption imaging. In Fig. 2.6 (b)

we show a typical experimental measure of the width of the expanding condensate after a fixed expansion time as a function of the disorder strength. One can see that for large values of the disorder strength the expansion is completely frozen and the absence of diffusion predicted by Anderson is observed. Another key feature of Anderson localization is the exponential shape of single particle eigenstates. This reflects in an exponential shape of the atomic cloud that can also be observed with in situ absorption imaging. In the inset of Fig 2.6 (b) and in Fig. 2.7 (c) two examples of measured exponentially localized profiles are shown. Fitting the exponentially localized profiles one can also obtain a measure of the localization length as shown in Fig. 2.7 (d).

In chapters 3, 4 and 5 of this thesis we will extensively focus on the experimental setup realized in Ref. [25], namely a one dimensional bichromatic optical lattice. This choice is motivated by the fact that in this experiment, not only the disorder strength can be controlled at will, but also the interatomic interaction can be tuned, making this configuration particularly suitable for the study of the interplay between interaction and disorder induced localization [67, 68, 33, 69].

More recently Anderson localization of matter waves has been reported also in 3D with both fermions [70] and bosons [71] using a similar procedure with respect to the one that has been used in 1D.

Let us finally mention that using cold atoms it has been possible to realize the kicked rotor and observe dynamical localization, which can be considered as a mapping of Anderson localization in momentum space. In particular both the 1D [72, 73] and the 3D case [74, 75, 76] have been considered.

Noninteracting particles in quasiperiodic potentials

Quasiperiodic systems are a special class of non-periodic systems. They possess two or more periodicities whose periods are incommensurate with each other. Although these systems are not random in the usual sense, they lack of translational symmetry since there exist no translations which will leave the periods of all the periodic structures invariant. Nevertheless, there exist translations that leave the system "almost invariant". This leads to quite unusual behaviours in quasiperiodic systems.

It is well known that in a perfectly periodic system all the eigenfunctions are extended Bloch waves [40] while for a one dimensional random potential all the eigenfunctions are exponentially localized [53, 2]. These properties are strictly connected with the spreading behaviour of an initially localized wavepacket, in the former case it expands ballistically while in the latter it remains localized.

In between these two extreme cases we find quasiperiodic systems that show an intermediate behaviour between the two [77, 78]. In particular it is known that quasiperiodic systems can have both extended and localized states already in one dimension. Furthermore "critical" states which may be regarded as being intermediate between localized and extended can appear. As a consequence the dynamics of a wavepacket can range from localization to ballistic expansion and also anomalous diffusion can be observed [79, 80]. These quantum properties are often related to the quite anomalous transport properties of quasicrystals [81, 82, 83].

The localization properties in quasiperiodic systems are often studied considering tight binding Hamiltonians similar to (2.9), where the on site energies are chosen in order to introduce one or more additional periodicities to the system, which are incommensurate with respect to the underlying periodicity of the model, given by the discretization of the space [78]. In this context the most studied model is probably the Aubry-André or Harper model, [84, 85] where one can observe extended, critical or localized states, as the strength of the on-site quasiperiodic modulation is increased. Another well-studied example is the Fibonacci model [86, 87] where the states are always critical, leading to anomalous transport properties [80]. A specific feature of these two models is that they have a "pure" spectrum, namely all the states of the system are of the same nature: extended, localized and critical states do not coexist in the spectrum. Notably, there are also models where the spectrum is not pure and one can have one or more mobility edges separating states of different nature. An example is provided by the Generalized Harper model [88]. Other examples of quasiperiodic system with non-pure spectrum can be found also

considering models in continuous space [89].

Due to their peculiarity, the localization properties of quasiperiodic systems have always received a lot of attentions, especially after the discovery of quasicrystals [81, 82] and the observation of their anomalous transport properties [83]. However, few years ago, a new boost has been given to the study of this topic after that two experiments with ultracold atoms have reported the first observation of Anderson localization of matter waves. In fact one of the two experiment have been performed using a 1D quasiperiodic potential and realized an experimental implementation of the Aubry-André model [25]. One year later another experimental implementation of the Aubry-André model has been realized using photonic crystals [65]. For this reason in this chapter we will focus on the localization properties of the Aubry-André model and on its connection with atomic gases experiments.

This chapter is organized as follows. In section 3.1 we explain how the Aubry-André model can be realized experimentally using ultracold atoms in bichromatic optical lattices. In sections 3.2 and 3.3 we discuss the localization properties of the model, first considering the nature of the eigenstates, as originally done by Aubry and André, and then studying the dynamics of an initially localized wavepacket. This second method reproduces the typical expansion experiment that is performed with ultracold atoms. For this reason we focus on two questions which can be relevant from the experimental point of view, namely the role played by the initial shape of the wavepacket and the difference between the incommensurate and the commensurate case. Finally in section 3.4 we discuss the localization properties of the Aubry-André model in momentum space and we propose a possible way to detect the transition from extended to localized regime in a feasible experiment with ultracold atoms by measuring the momentum distribution of the atoms.

3.1   From bichromatic optical lattices to the Aubry-André model

One-dimensional bichromatic lattices are realized in experiments with Bose-Einstein condensates by superimposing two optical lattices of different wavelengths [89, 90, 49, 25], producing an external potential acting on the atoms in this form:

$$
\begin{aligned}
V_b(x) &= V_1(x) + V_2(x) \\
&= s_1 E_{R_1} \sin^2(k_1 x) + s_2 E_{R_2} \sin^2(k_2 x + \varphi) \,,
\end{aligned}
\tag{3.1}
$$

where $k_j = 2\pi/\lambda_j$ ($j = 1, 2$) is the wavenumber of the laser light that creates the optical lattice, $E_{R_j} = \hbar^2 k_j^2/(2m)$ is the recoil energy, s_j is the dimensionless lattice strength and φ is an arbitrary phase shift between the two lattices. One of the two lattices is typically used as the main periodic potential (primary lattice) and determines the main separation of the single-particle states in different Bloch bands. It is chosen to be strong enough ($s_1 \gg 1$) to apply the tight-binding approximation. This means that the primary lattice induces a discretization of the system with period $d = \lambda_1/2$, i.e., the atoms occupy only the wells of the primary lattice and
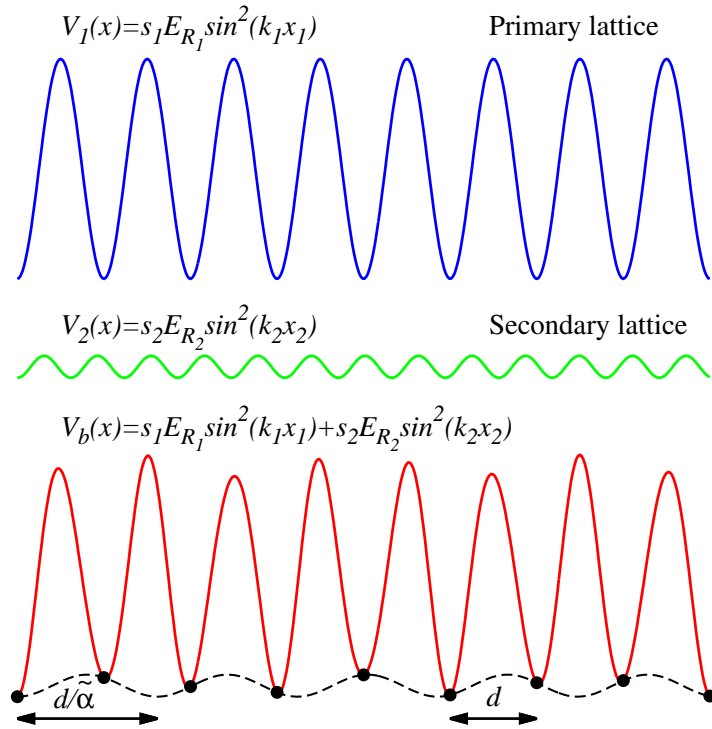
Figure 3.1: *Representation of a bichromatic optical lattice. The superposition of a deep primary lattice (blue line) and of a shallower secondary lattice (green line) produces the quasiperiodic potential represented by the red line. The black dots indicate the on-site energies within a discretized description of the system. The black line shows that the modulation introduced by the secondary lattice has a cosinusoidal form. The two black arrows represent the two key length scales of the system: the lattice spacing introduced by the primary lattice, d, and the periodicity of the modulation introduced by the secondary lattice, $d/\tilde{\alpha}$.*

can tunnel from one site to the other with a given tunneling rate J [91]. The second lattice is significantly shallower ($s_2 \ll s_1$) and perturbs weakly the structure formed by the primary lattice; in practise, the presence of the secondary lattice does not modify significantly the position of the minima of the potential but produces only a shift of the on site energies, introducing a "deterministic" disorder, or quasi-disorder [25, 90, 49].

Noninteracting atoms in the presence of a one-dimensional bichromatic optical lattice are described by the Hamiltonian

$$H = -\frac{\hbar^2}{2m}\frac{\partial^2}{\partial x^2} + V_b(x) \tag{3.2}$$

In first approximation, let us consider the situation in which $s_2 = 0$ and we are

left with a simple periodic system, where the spectrum is characterized by bands of allowed energies and energy gaps and the eigenstates are Bloch functions delocalized over the whole lattice [40]. In the tight binding regime the energy gap between the lowest band and the first exited band, E_G, is so large that the physics of the system can be well described by considering only the lowest energy band. This is a good approximation as long as all the energy scales involved in the problem under consideration are much smaller than E_G. Let us introduce a set of Wannier states $\mid w_j \rangle$ labelled by the site index j (see appendix A for an introduction on Wannier functions). Each of them, considered in real space, $\langle x \mid w_j \rangle = w_j(x) = w(x - x_j)$ represents a function centered around the lattice site j, at position $x_j = jd$. In particular, as previously mentioned one can consider as a basis of the system just the Wannier functions associated to the lowest energy band. One can therefore express wavefunctions and operators projecting on the basis of Wannier states

$$\mid \psi \rangle = \sum_j \psi_j \mid w_j \rangle,$$

$$H = \sum_{i,j} \mid w_i \rangle H_{i,j} \langle w_j \mid, \tag{3.3}$$

where $H_{i,j} = \langle w_i \mid H \mid w_j \rangle$, $\psi_j = \langle w_j \mid \psi \rangle$ and $n_j = |\psi_j|^2$ represents the probability of finding a particle in the lattice site j. Let us evaluate explicitly the matrix elements $H_{i,j}$:

$$\begin{aligned} H_{i,j} &= \int w_i^*(x) H w_j(x)\, dx \\ &= \int w_i^*(x) H^{(0)} w_j(x)\, dx + \int w_i^*(x) H^{(1)} w_j(x)\, dx, \end{aligned} \tag{3.4}$$

where $H^{(0)} = -\frac{\hbar^2}{2m}\frac{\partial^2}{\partial x^2} + s_1 E_{R_1} \sin^2(k_1 x)$ is the part of the Hamiltonian formed by the kinetic term and by the primary lattice, while $H^{(1)} = s_2 E_{R_2} \sin^2(k_2 x + \varphi)$ is just formed by the secondary lattice. Neglecting the overlap between Wannier functions beyond nearest neighbours for $H^{(0)}$ and retaining only the on-site contribution for $H^{(1)}$ one finds that the only non-zero matrix elements are

$$H_{i,j} = E_0 \delta_{i,j} - J \delta_{i,j\pm 1} + \delta_{i,j} \int |w_i(x)|^2 H^{(1)}\, dx \tag{3.5}$$

where

$$E_0 = \int w_i^*(x) H^{(0)} w_i(x)\, dx\,; \qquad J = -\int w_i^*(x) H^{(0)} w_{i+1}(x)\, dx. \tag{3.6}$$

The first term in equation (3.5) represents a constant on-site term that plays the only role of shifting the energies of the system by a constant value E_0, therefore in the following we will drop it. The second term is the one that connects neighbouring sites and its proportional to the tunneling energy J. Finally the last term describes the quasiperiodic shift of the on-site energies induced by the secondary lattice. This term

can be written in a much simpler form using the trigonometric relation $\sin^2(k_2 x + \varphi) = [1 - \cos(2k_2 x + 2\varphi)]/2$. Using the symmetry of the Wannier functions one can show that

$$\int \left[-\frac{s_2 E_{R_2}}{2} \cos(2k_2 x + 2\varphi) \right] |w_i(x)|^2 \, dx = \Delta \cos(2\pi\alpha i + \varphi') \qquad (3.7)$$

where we have used the fact that $x_i = id = i\pi/k_1$, we have redefined the phase φ and introduced $\alpha = k_2/k_1 = \lambda_1/\lambda_2$ and

$$\Delta = \frac{s_2 E_{R_2}}{2} \int \cos(2k_2 y)|w(y)|^2 \, dy. \qquad (3.8)$$

Finally neglecting all constant terms one ends up with the following simple expression for the matrix elements

$$H_{i,j} = -J\delta_{i,j\pm 1} + \delta_{i,j}\Delta \cos(2\pi\alpha i + \varphi). \qquad (3.9)$$

Substituting this expression in (3.3) and expressing all the energies in units of J one finds the Aubry-André Hamiltonian

$$H = -\sum_j \left(|\, w_j \rangle\langle w_{j+1} \,| + |\, w_{j+1} \rangle\langle w_j \,| \right) + \lambda \sum_j \cos(2\pi\alpha j + \varphi) \,|\, w_j \rangle\langle w_j \,| \quad (3.10)$$

where $\lambda = \Delta/J$. In this last expression we explicitly see that the modulation introduced by the secondary lattice has a cosinusoidal form and it can be seen as a potential in the discrete space:

$$V_j = \lambda \cos(2\pi\alpha j + \varphi). \qquad (3.11)$$

Let us notice that the discrete potential is quasiperiodic as long as the parameter α, which is the ratio between the wavelengths of the two lattices, is an irrational number. In fact, only when α is irrational the potential V_j adds a second periodicity which is incommensurate with respect to the underlying periodicity given by the discreteness of the system. Let us notice that V_j is invariant under a shift of α by an integer number and therefore, without any loss of generality, one can choose $\alpha < 1$.

In figure 3.1 we show an example of a bichromatic optical lattice and we schematically illustrate the discretization procedure. We considered $\alpha = (\sqrt{5} - 1)/2$ and a primary lattice much deeper than the secondary one. One can notice that the position of the wells of the bichromatic potential are determined by the primary lattice while the secondary lattice introduces just a modulation of the on-site energy. The black dots shows the value of the on-site energies within a discretized description of our system while the black line stresses the fact that this modulation has an oscillating form. The period of the modulation is given by $d/|\tilde{\alpha}|$ (or $1/\tilde{\alpha}$ in units of lattice sites) where $\tilde{\alpha}$ is obtained by shifting the value of α by an integer number so that it lies in the interval $[-0.5, 0.5]$. In the specific case shown in figure 3.1,

$\tilde{\alpha} = (\sqrt{5} - 3)/2$ and therefore we encounter a minimum in the lattice modulation approximately every 2.62 lattice sites.

Writing down the time independent Schrödinger $H \mid \psi \rangle = E \mid \psi \rangle$ equation for the tight binding Hamiltonian (3.10) one obtains

$$- \psi_{j+1} - \psi_{j-1} + \lambda \cos(2\pi\alpha j + \varphi)\psi_j = E\psi_j. \tag{3.12}$$

This equation is the one which is usually called Aubry-André or Harper model [85]. This model is of particular importance because, despite its simplicity, is very rich from the point of view of the localization properties and those are known exactly. The key parameter that determines the localization properties, when α is irrational, is λ which quantifies how strong is the quasi-disorder compared to the tunneling energy. In the following with a slight abuse of notation we will sometimes call λ the disorder strength.

3.2   Localization properties of the Aubry-André model

The localization properties of model (3.12) have been discussed for the first time by Aubry and André [85]. Later a number of numerical and analytical studies confirmed their results [77, 86, 92, 79, 88, 93]. Here, following the original calculation of Aubry-André, we show how one can derive the localization properties of the model using the self-duality of Eq. (3.12) and the Thouless formula for the Lyapunov exponent (2.15).

The self-duality property of equation (3.12) can be found by introducing the following transformations

$$\psi_j = e^{i\theta j} \sum_{l=-\infty}^{\infty} d_l e^{il(2\pi\alpha j + \varphi)}$$

$$d_l = e^{-i\varphi l} \sum_{j=-\infty}^{\infty} \psi_j e^{-ij(2\pi\alpha l + \theta)}. \tag{3.13}$$

Using these transformations in equation (3.12) one can show that the new variable d_l satisfies the dual equation

$$- d_{l+1} - d_{l-1} + \frac{4}{\lambda} \cos(2\pi\alpha l + \theta)d_l = \frac{2E}{\lambda}d_l \,, \tag{3.14}$$

which has exactly the same form as equation (3.12) if we set

$$\frac{4}{\lambda} \to \lambda \,, \qquad d_l \to \psi_j \,, \qquad \frac{2E}{\lambda} \to E \,, \qquad \theta \to \varphi \,. \tag{3.15}$$

The symmetry of Eqs (3.12) and (3.14) has an important consequence. One can note that, if ψ_n is a localized solution of (3.12), that is

$$\sum_{j=-\infty}^{\infty} |\psi_j|^2 < \infty,$$

then d_l will be an extended solution solution of (3.14), that is

$$\sum_{l=-\infty}^{\infty} |d_l|^2 = \infty,$$

and vice versa. This tell us that the dual transformations (3.13) exchanges the localization properties of the eigenfunctions. However, a priori we ignore which eigenfunctions are localized and which are extended. To go further we need to use the Thouless formula (2.15) which relates the Lyapunov exponent $\Lambda(E)$ to the density of states $\rho(E)$ [58]. This formula was originally introduced for random systems but it can be used without any change also for non-random models such as (3.12). Whenever α is an irrational number, making use of the dual property, one can relate the integrated density of states of the Aubry-André model $\mathcal{N}_{\lambda,\alpha}(E)$ to the one of its dual counterpart $\mathcal{N}_{\frac{4}{\lambda},\alpha}(E)$ [85]. The same can be done for the density of states $\rho(E) = \frac{\partial}{\partial E}\mathcal{N}(E)$ and one finds

$$N_{\lambda,\alpha}(E) = N_{\frac{4}{\lambda},\alpha}\left(\frac{2E}{\lambda}\right) ; \qquad \rho_{\lambda,\alpha}(E) = \rho_{\frac{4}{\lambda},\alpha}\left(\frac{2E}{\lambda}\right)\frac{2}{\lambda}. \tag{3.16}$$

Using these expressions and the Thouless formula one obtains the dual transform of the Lyapunov exponent

$$\Lambda_{\lambda,\alpha}(E) = \Lambda_{\frac{4}{\lambda},\alpha}\left(\frac{2E}{\lambda}\right) + \ln\left(\frac{\lambda}{2}\right). \tag{3.17}$$

Starting from this expression it is now possible to infer the localization properties of the Aubry-André model with few simple considerations. First of all, we note that the Lyapunov exponent $\Lambda(E)$ associated to a given eigenstate is necessarily a positive number and that $\Lambda(E)$ vanishes only whenever this state is extended. Let us also recall the result that we have derived earlier in this section that the dual transformation inverts the localization properties; therefore whenever $\Lambda_{\lambda,\alpha}(E)$ is non-zero it follows that $\Lambda_{\frac{4}{\lambda},\alpha}\left(\frac{2E}{\lambda}\right)$ is zero and vice-versa. Therefore assuming that $\Lambda_{\frac{4}{\lambda},\alpha}\left(\frac{2E}{\lambda}\right) = 0$ it follows that

$$\Lambda_{\lambda,\alpha}(E) = \ln\left(\frac{\lambda}{2}\right)$$

and the positivity of the Lyapunov exponent implies that $\lambda > 2$. Conversely, when $\Lambda_{\lambda,\alpha}(E) = 0$

$$\Lambda_{\frac{4}{\lambda},\alpha}\left(\frac{2E}{\lambda}\right) = \ln\left(\frac{2}{\lambda}\right)$$

and $\lambda < 2$.

We can therefore conclude that the Aubry-André model (3.12) undergoes a transition from extended to localized eigenstates at $\lambda = 2$. All eigenstates are extended for $\lambda < 2$ and exponentially localized for $\lambda > 2$. Moreover all the eigenstates have the same localization length

$$L_{loc} = 1/\Lambda = \frac{1}{\ln(\lambda/2)}. \tag{3.18}$$
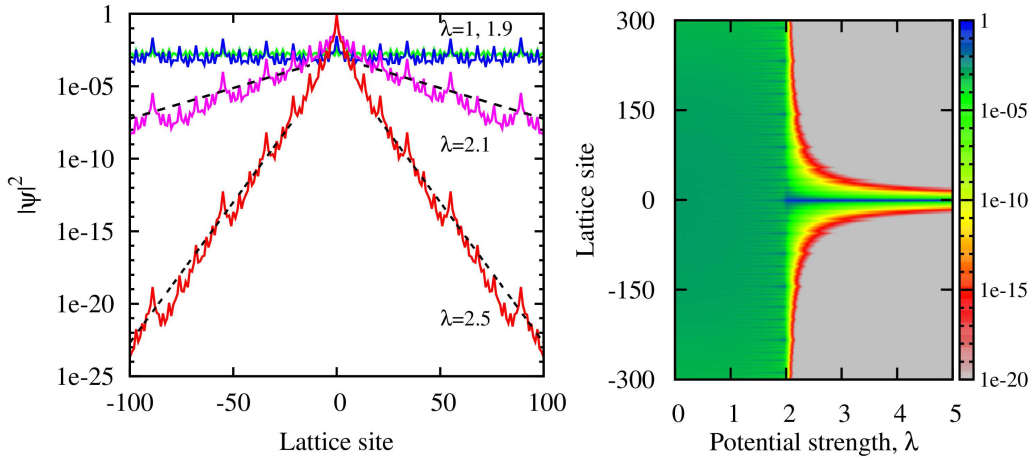
Figure 3.2: *Numerical study of of the localization properties of the Aubry-André model. In the left panel we show that the ground state of the system is extended for $\lambda = 1$ (green line) and $\lambda = 1.9$ (blue line) while it is exponentially localized for $\lambda = 2.1$ (magenta line) and $\lambda = 2.5$ (red line). In the localized regime we also show the localization length predicted by the analytical formula (3.18) (black dashed lines). In the right panel a color density plot shows the ground state as a function of the disorder strength. The transition from the extended to the localized regime at $\lambda = 2$ is clearly visible.*

The opposite properties holds for the dual model (3.14). The simple derivation that we presented here does not give any information about the nature of the eigenstates for $\lambda = 2$. It is known that they are neither plane waves nor exponentially localized. It is conjectured that they are decreasing functions with a power law [85].

The exponential localization that takes place for $\lambda > 2$ has been identified by Aubry and André [85] as Anderson localization in a quasiperiodic potential, analog to Anderson localization in a purely random potential. A different interpretation, based on a semiclassical analysis, has been recently proposed in Ref. [94].

In figure 3.2 we present a numerical calculation that confirms the results that we have already obtained on the localization properties of the Aubry-André model. We show the behaviour of the ground state of the system for different values of the potential strength, λ. In the right panel it is clearly observed that for $\lambda = 1$ and $\lambda = 1.9$ the ground state is an extended plane wave which follows the quasiperiodic modulations of the potential. Conversely for $\lambda = 2.1$ and $\lambda = 2.5$ the ground state is exponentially localized with a localization length which is in agreement with the theoretical expression (3.18), which in the figure is represented by the black dashed lines. In the left panel, a color density plot shows the ground state of the system across the transition point. The transition at $\lambda = 2$ is clearly visible. Here we showed our results for the ground state of the system but similar density profiles are obtained also for the exited states.
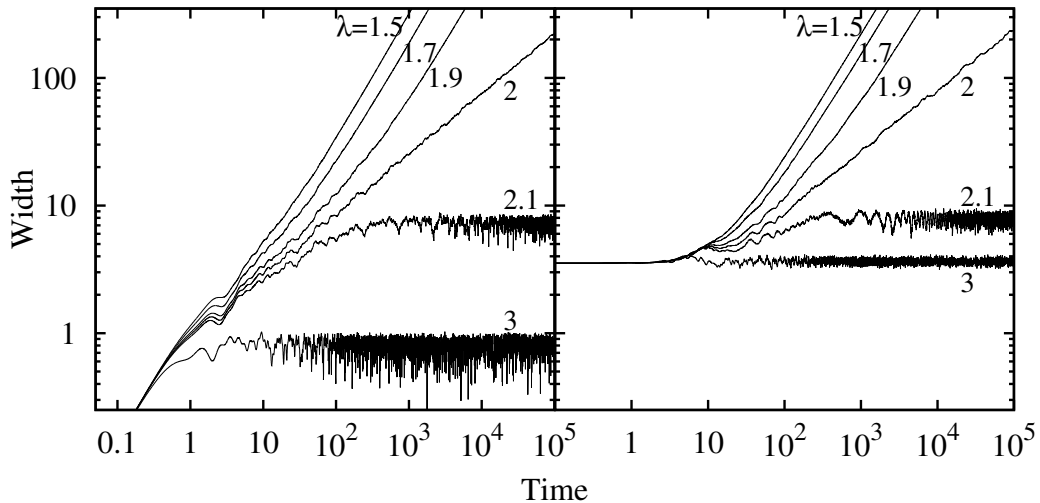
Figure 3.3: *Expansion of a noninteracting cloud of atoms in the Aubry-André model with $\alpha = (\sqrt{5} - 1)/2$. The time evolution of the width of the wavepacket $w(t)$ is shown for different values of the disorder strength, $\lambda = 1.5, 1.7, 1.9, 2, 2.1, 3$. In the left panel, the starting wavepacket is a δ-function localized in a single site. In the right panel we use an initial Gaussian wavepacket of width $\sigma = 5$. In both cases, one clearly observes the transition from extended to localized states that occurs at $\lambda = 2$.*

3.3 Spreading of wavepackets in the Aubry-André model

In this section we discuss the problem of quantum diffusion of an initially localized wavepacket in the Aubry-André model. This is of particular relevance for experiments with ultracold atoms where the expansion of an atomic cloud is the main tool used for the detection of Anderson localization [24, 25]. Both the width of the expanding cloud and its shape are of great interests.

The expansion of a noninteracting wavepacket is described by the time dependent Schrödinger equation $i\hbar\frac{\partial}{\partial t} \mid \psi \rangle = H \mid \psi \rangle$ that in the case of Hamiltonian (3.10) takes the following form

$$i\frac{\partial \psi_j}{\partial t} = -\psi_{j+1} - \psi_{j-1} + \lambda \cos(2\pi\alpha j + \varphi)\psi_j, \qquad (3.19)$$

where we have absorbed the Planck constant $\hbar$ in the time variable so that t becomes a dimensionless quantity. The actual time in seconds can be obtained by multiplying the dimensionless parameter t by $\hbar/J$.

We investigate the evolution starting from two different classes of initial conditions, namely a δ-function localized in a single lattice site,

$$\psi_j(0) = \delta_{j,0}, \qquad (3.20)$$

and a Gaussian wavepacket of width σ,

$$\psi_j(0) = Ce^{-\frac{j^2}{2\sigma^2}}\,, \tag{3.21}$$

where C is a normalization factor that has to be determined in order to have a norm of the wavepacket equal to one $\sum_j |\psi_j|^2 = 1$. The choice of Gaussian wavepackets is convenient if one wants to simulate realistic experimental configurations; it also allows one to explore the behavior of sharp to broad wavepackets in a continuous manner. Owing to arbitrariness of the phase φ, here we have chosen, without any loss of generality, to place the initial wavepacket around the lattice site $j = 0$.

As a measure of the localization we consider two quantities: the width of the wavepacket measured as the square root of the second moment of the spatial distribution $|\psi_j(t)|^2$,

$$w(t) = \sqrt{m_2(t)} = \sqrt{\sum_j (j - X)^2 |\psi_j(t)|^2}\,, \tag{3.22}$$

and the participation number

$$P(t) = \frac{1}{\sum_j |\psi_j(t)|^4}\,, \tag{3.23}$$

which measures the number of significantly occupied lattice sites [95]. The quantity X represents the average position of the wavepacket, defined as $X = \sum j|\psi_j|^2$.

The localization transition of the Aubry-André model at $\lambda = 2$, which has been introduced in the previous section, can be detected in the dynamics (quantum diffusion), by looking for example at the width of the wavepacket as a function of time [79]. In particular the asymptotic spreading of the wavepacket width $w(t)$ can be parametrized as $w(t) \sim t^\gamma$, and one finds three different regimes as the value of λ is varied:

(i) $\lambda < 2$: ballistic regime, $\gamma = 1$

(ii) $\lambda = 2$: subdiffusive regime, $\gamma \sim 0.5$

(iii) $\lambda > 2$: localized regime, $\gamma = 0$.

We solve Eq. (3.19) by using a standard fourth order Runge-Kutta (RK4) algorithm for the numerical integration. The accuracy of the integration is checked by monitoring the conservation of the norm of the wavepacket and of the energy of the system. A standard choice for the value of α consists of choosing the inverse golden mean $\alpha = (\sqrt{5} - 1)/2$ [95]. Our results for this value of α are shown in Fig. 3.3. In the case of an initial δ-function wavepacket (left panel), we find perfect agreement with previous calculations [79]. The right panel shows our results for the case of an initial Gaussian wavepacket. By comparing the two cases, one can see that the asymptotic behaviour is not affected by the choice of the initial shape of the wavepacket. Similar results are obtained for the participation number $P(t)$.
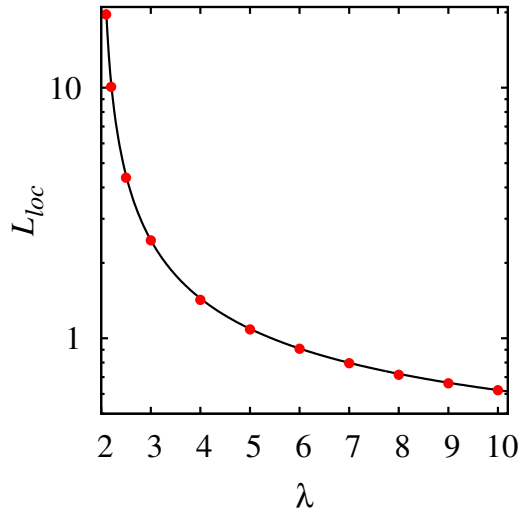
**Figure 3.4:** *Localization length of the wavepacket L_{loc} as a function of the disorder strength λ in the localized regime. We measure the localization length by fitting the tails of the localized wavepacket after the expansion. We compare the values of the localization length extracted from the fitting (red points) with the analytic prediction $L_{loc} = \frac{1}{\ln(\lambda/2)}$ (black line).*

As regards the shape of the wavepacket we focus on the localized regime $\lambda > 2$ where spreading stops after a transient time. Since, for a given disorder strength λ, all eigenstates are exponentially localized with the same localization length we expect that also the wavepacket, which is formed by a linear superposition of different eigenstates, has exponentially decaying tails with the same characteristic localization length. By fitting the density profiles of the wavepacket after the expansion we extract a value of the localization length. In Fig. 3.4 we show the result of our fits as a function of the disorder strength λ (red points) and we compare them with the theoretically expected value $L_{loc} = 1/\log(\lambda/2)$ (black line) showing a perfect agreement.

3.3.1 Incommensurate vs. commensurate case

It is worth stressing that a truly quasiperiodic potential can not be realized in any realistic experiment, since the wavelengths of the lasers are always known with a finite number of digits and therefore their ratio will always be a rational number. Moreover real experiments have always a finite size. It is thus important to clarify to which extent the predictions of the Aubry-André model are relevant for the description of experiments with ultracold atoms in bichromatic optical lattices.

To this purpose it is useful to compare the case of a quasiperiodic potential with an irrational value of α with the case of a periodic potential obtained by using a
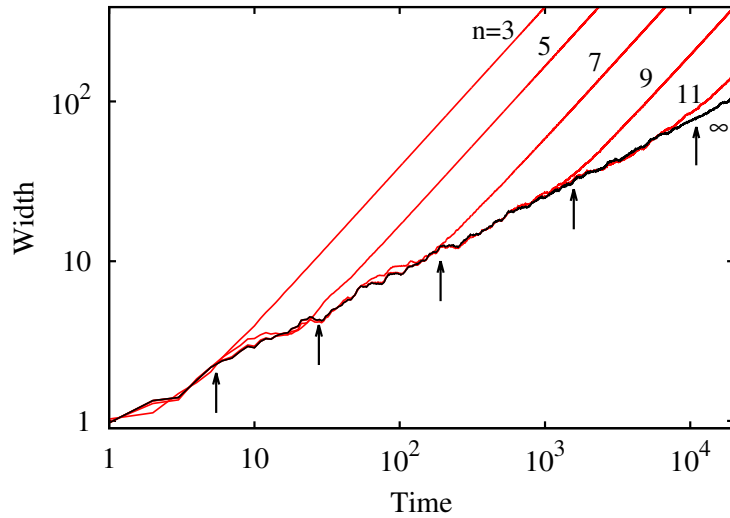
Figure 3.5: *Time evolution of the width of the wavepacket $w(t)$ of noninteracting particles, starting from a single-site δ-function, for $\lambda = 2$ and for different orders, n, of the approximants in the Fibonacci sequence. The black arrows represent the values of t at which we observe the transition from the behaviour predicted for a quasiperiodic potential (incommensurate lattice) to the diffusion expected in a periodic potential.*

rational approximation α_n of order n of the irrational number. In particular we consider a sequence of rational numbers α_n, that converges to the irrational value α as $n \to \infty$ [96, 78]. The sequence of approximants α_n can be found by successive truncations of the continued-fraction expansion of α. For the case of the golden mean $\alpha = (\sqrt{5} - 1)/2$ [95] the approximants are given by $\alpha_n = p_n/q_n$, where p_n and $q_n = p_{n+1}$ are two consecutive terms of the Fibonacci sequence ($p_1 = p_2 = 1$, $p_n = p_{n-1} + p_{n-2}$ for $n > 2$).

It turns out that the incommensurate case can thus be considered as the limit of a sequence of commensurate Hamiltonians, whose eigenvalues $E^{\xi,m}$ and eigenfunctions $\phi_j^{\xi,m}$ can be labelled by the quasi-momentum ξ and the band index m, since the spatial periodicity of the system, with period q_n, permits to use the Bloch wave decomposition. One finds that, for sufficiently large n and for $\lambda > 2$, the eigenfunctions are indeed characterized by periodic replica of exponentially localized functions within each period of the potential, that in the limit $n \to \infty$ tend to a single localized function [91].

Let us now consider the same problem from the point of view of the dynamical properties. The time evolution for $\alpha = (\sqrt{5} - 1)/2$ has to be compared to the one obtained using the approximant of order n in the Fibonacci sequence. For any finite value of n the system is periodic, with wavelength q_n, and the diffusion of an initially localized wavepacket is expected to be ballistic ($w(t) \sim t$). However, in the
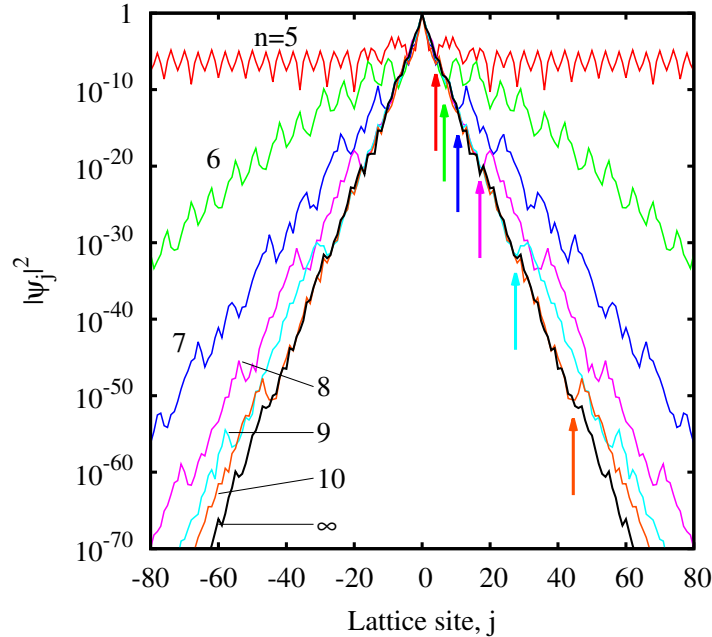
Figure 3.6: *Modulus square of the wavefunction $|\psi_j|^2$ for different values of n, plotted at a fixed evolution time $t = 1000$, for $\lambda = 7$ and $\beta = 0$. The initial wavepacket at $t = 0$ is a δ-function localized at $j = 0$. The vertical arrows are drawn at the positions $q_n/2$.*

limit $n \to \infty$ one must recover the results of the Aubry-André model, with a critical behaviour for $\lambda = 2$ and localized states for $\lambda > 2$. The approach to this limit in nontrivial and involves the characteristic time and length scales of the system.

In Fig. 3.5 we first show our results for the diffusion of a δ-like wavepacket in a lattice with the critical value $\lambda = 2$. For any finite n the wavepacket exhibits a subdiffusive spreading ($w(t) \sim t^\gamma$ with $\gamma \approx 0.5$), as in the incommensurate case, within an initial time interval. Then, at time τ, the width starts growing as in a ballistic expansion in a periodic lattice. The transition between the two regimes turns out to occur when the width of the wavepacket becomes of the same order of the spatial periodicity of the lattice. The transition time, τ, indicated by the arrows in Fig. 3.5, increases with the order n of the approximants and the corresponding width, $w(\tau)$ exhibits a linear dependence on the periodicity of the system, q_n[1]. The role of the spatial periodicity is even more evident if one plots the density distribution in the regime of localization, as shown in Fig. 3.6 for $\lambda = 7$ and $t = 1000$. In this figure the arrows are drawn at the positions $q_n/2$. As one can see, the

---

[1] A linear fit of the width $w(\tau)$ at the transition time τ, as a function of the spatial periodicity, gives $[w(\tau)](q_n) = aq_n + b$, with $a = 0.547(4)$ and $b = 0.8(2)$. The times τ's and the relative widths $w(\tau)$'s have been determined by fitting the subdiffusive behaviour of the incommensurate case and the linear behaviours of the commensurate cases and finding the intersection points between these two fits.
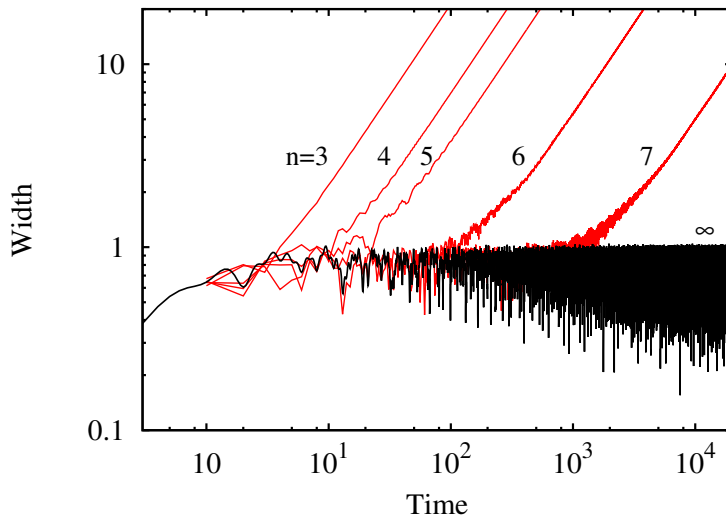
Figure 3.7: *Time evolution of the width of the wavepacket $w(t)$ of noninteracting particles, starting from a single-site δ-function, for $\lambda = 3$ and for different values of n.*

deviations from the density distribution of the incommensurate case ($n \to \infty$) are caused by the spreading of the lateral components of the distribution, i.e., those at a distance of the order of, or larger than $q_n/2$. The asymptotic behaviour ($t \to \infty$) is always ballistic. However, for a finite t and for $\lambda > 2$ the central part of the density distribution (within a width of order q_n) exhibits an exponential localization, independent of n, and is almost indistinguishable from the one predicted for the incommensurate lattice. The spreading of the low density tails affects the behaviour of the width defined in Eq. (3.22). An example is shown in Fig. 3.7. For short times the contribution of the expanding tails is negligible, while for later times the width increases as in a ballistic expansion. It is worth stressing, however, that these effects of the low density tails are expected to be hardly detectable in actual experiments, due to the finite resolution in the measurement of the density distribution.

Given the typical timescale and optical resolution of the experiments with ultra-cold gases in optical lattices, our analysis confirms that the transition from diffusion to localization observed in Ref. [25] can correctly be interpreted in terms of the predictions of the Aubry-André model.

3.4   Localization of ultracold atoms in momentum space

In the literature the evolution of wavepackets in the Aubry-André model has been investigated mainly in real space, looking for signatures of the transition from ballistic spreading to subdiffusion and localization, both in theory [79, 31] and experiments [25, 66]. Here we focus on the dynamics of the momentum distribution and iden-

tify measurable effects of the transition from diffusion to localization in momentum space. This is relevant for current experiments with ultracold atoms, where the momentum distribution is accessible *via* time of flight measurements and, typically, with an higher accuracy than in real space. In addition, our results provide complementary information for a better understanding of the key role played by duality of the Aubry-André model.

In the following we first introduce the Aubry-André model in momentum space, show its connection with the dual space and discuss its localization properties. We then discuss the presence of periodic oscillations in the dynamics of wavepackets in the Aubry-André model, both in momentum and in real space and we interpret these oscillations in terms of a simple theoretical model. Finally we identify an observable quantity that could be used in a feasible experiment for the observation of the Aubry-André transition in momentum space.

In this section we will focus on the case of a rational value of α which can be written as the ratio of two integer numbers $\alpha = p/q$. In this situation the solution of Eq. (3.19) can be restricted to a region of size $N = q$, which coincides with the spatial periodicity of the system. As we have described in Section 3.3.1 the case of irrational α can be obtained as a limit of a continued fraction approximation.

3.4.1   Aubry-André model in momentum space

Let us first explain how one can introduce the momentum distribution starting from a discrete description as the one given by Eq. (3.19). The continuous wavefunction associated to our discrete system is given by

$$\psi(x) = \sum_j \psi_j w_j(x) \tag{3.24}$$

where $w_j(x) = w(x - j)$ are the Wannier functions of the primary lattice and we have expressed the distances in units of lattice spacing. The momentum distribution $|\tilde{\psi}(k)|^2$ can be calculated by taking the Fourier Transform of wavefunction (3.24) and one finds

$$\tilde{\psi}(k) = \sqrt{N} f_k \tilde{w}(k) \tag{3.25}$$

where $\tilde{w}(k)$ is the Fourier transform of the Wannier function centered on the lattice site $j = 0$ and we have introduced f_ξ which is the discrete Fourier Transform (DFT) of ψ_j

$$f_\xi = \frac{1}{\sqrt{N}} \sum_j \psi_j e^{-i\xi j}. \tag{3.26}$$

Here we use ξ to indicate the quasi-momentum. From a physical point of view performing the DFT corresponds to a projection of the discrete wavefunction on the basis of quasi-momentum eigenstates. The allowed values of ξ in our system are given by $\xi = (2\pi/N)k$ and are restricted to the first Brillouin zone, $\xi \in [-\pi, \pi]$. In the following we will perform our analysis considering the quasi-momentum distribution $|f_\xi|^2$, then its easy to extend our results to the momentum space using this

simple relation that relates the momentum distribution with the quasi-momentum distribution

$$|\tilde{\psi}(k,t)|^2 = N|f_k(t)|^2|\tilde{w}(k)|^2. \tag{3.27}$$

By applying the transformation (3.26) to the Aubry-André model one finds [91]

$$i\frac{\partial}{\partial t}f_\xi = -2\cos(\xi)f_\xi + \frac{\lambda}{2}\left(e^{-i\varphi}f_{\xi+2\pi\alpha} + e^{i\varphi}f_{\xi-2\pi\alpha}\right) \tag{3.28}$$

which is the equation describing the evolution in quasi-momentum space. Let us note that the DFT exchanged the potential and the tunneling term with respect to Eq. (3.19) and that the tunneling no longer takes place between nearest neighbouring sites but between momentum components differing by $|\Delta\xi| = 2\pi\alpha$.

In order to have an insight on the localization properties in the quasi-momentum space let us recall that Aubry-André showed that the following transformation

$$d_l = \frac{1}{\sqrt{N}}\sum_j \psi_j e^{ij[2\pi\alpha l+\theta]}e^{-i\varphi l} \tag{3.29}$$

maps Eq. (3.19) into an equation for the new variable d_l exactly of the same form as Eq. (3.19) but with disorder strength $4/\lambda$. This is called the duality of the Aubry-André model (cfr. section 3.2). Let us note that transformation (3.29) corresponds to a projection on a basis of quasi-momentum eigenstates with eigenvalues $\xi = 2\pi\alpha l + \theta$. As a consequence one can see that there is a strict connection between the quasi-momentum space and the dual space introduced by (3.29). More precisely the quasi-momentum ξ can be calculated by multiplying the index l by $2\pi\alpha$ and introducing a phase shift θ. Therefore the amplitudes f_ξ in quasi-momentum space can be obtained from the amplitudes d_l in dual space simply with a re-labelling procedure. We can say that (3.26) is related to the dual transformation (3.29) by an arbitrary shift θ and a permutation [97]. This suggests that the localization properties in quasi-momentum space are the same of the localization properties of the dual Aubry-André model, except for the fact that disorder couples modes differing by $|\Delta\xi| = 2\pi\alpha$ instead of neighboring ones.

In order to verify our prediction on the localization properties in quasi-momentum space we will study numerically the evolution of the quasi-momentum distribution $|f_\xi|^2$ by first solving Eq. (3.19) in real space using a RK4 algorithm and then mapping the result in quasi-momentum space by performing the DFT. As initial condition we choose a Gaussian wavepacket, $\psi_j(0) = C\exp\{-j^2/2\sigma^2\}$. The limiting case of vanishing width $\sigma = 0$ will correspond to a δ-function initial condition.

According to the previous discussion, the localization properties in momentum space are opposite with respect to the one of the Aubry-André model in real space, namely localization occurs for $\lambda < 2$, where the wavepacket instead spreads in real space. In this regime one thus expects to see only one or few momentum components significantly populated. Conversely, for $\lambda > 2$ the regime is diffusive in momentum space and localized in real space, and one should see a momentum
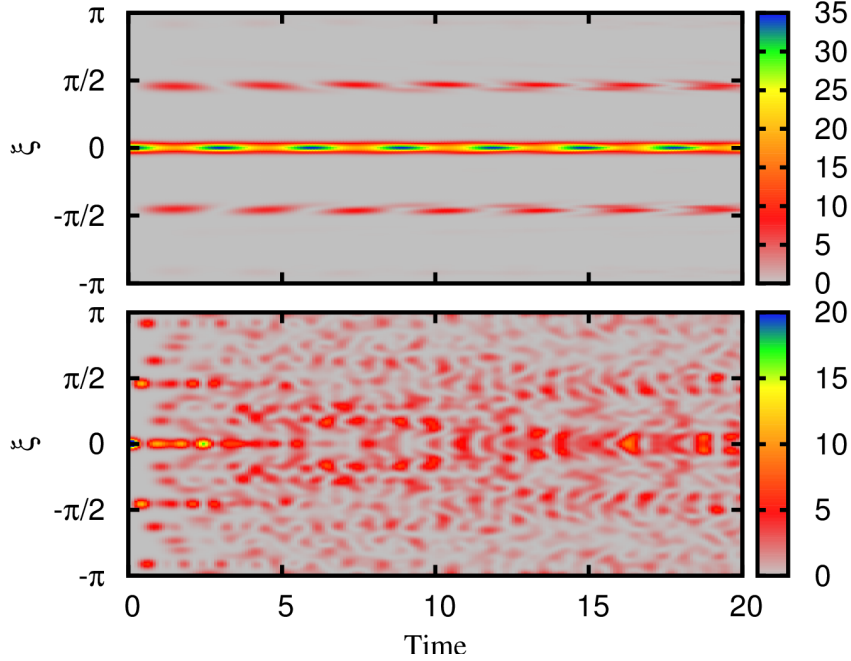
Figure 3.8: *Quasi-momentum distribution $|f_\xi(t)|^2$ obtained from the DFT of the solution of Eq (3.19). Here we use $\alpha = 0.2282...$ and $\varphi = 0$. The initial wavepacket in real space is a Gaussian of width $\sigma = 10$. Time is given in dimensionless units. Top panel: $\lambda = 1$, only few modes are involved and a periodic oscillation of the central and side peaks is observed. The side peaks are at a distance $\pm 2\pi\alpha$ from the central peak. Bottom panel: $\lambda = 5$, the evolution is affected by the coupling of many modes and the periodic oscillations are no more visible.*

distribution with many modes coupled together during the evolution of the system. This is indeed confirmed by our numerical simulations, as shown in Fig. 3.8 for $\alpha = 1064.4/866.6 - 1 = 0.2282...$. This value of the ratio between the wavelength of the two lattices α has been chosen in order to model the bichromatic lattice of the experiment of Ref. [67]. For $\lambda < 2$, as expected, we observe localization in the sense that just few momentum components are populated during the evolution. A striking feature is that the quasi-momentum components $|f_\xi|^2$ exhibit periodic oscillations, occurring among the central peak at $\xi = 0$ and two side peaks at $\xi = \pm 2\pi\alpha$. For $\lambda > 2$ instead many modes are populated and no periodic oscillations are observed.

3.4.2   Periodic oscillations in the Aubry-André model

Let us now characterize and interpret the periodic oscillations that we have observed in the time evolution of the quasi-momentum distribution.

We first perform a systematic study of these oscillations from a numerical point of view as the disorder strength λ is changed (always remaining in the regime $\lambda < 2$ where it is possible to observe the periodic behaviour). We extract the oscillation
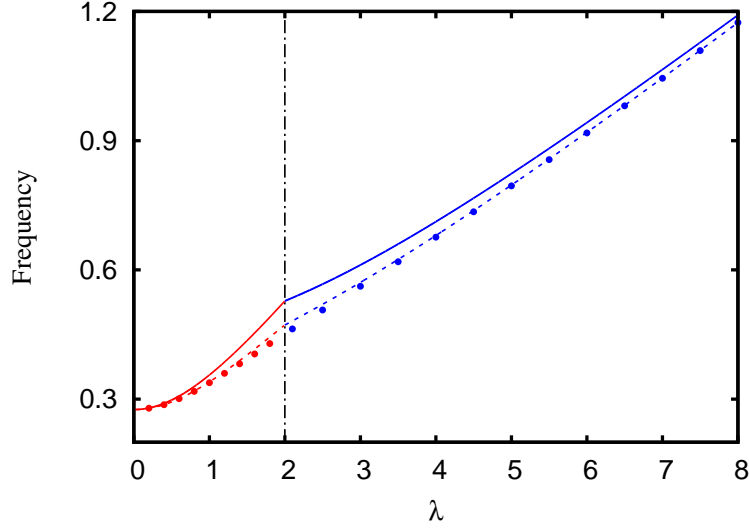
Figure 3.9: *Oscillation frequency of the central peak of quasi-momentum ($\lambda < 2$, red) and spatial ($\lambda > 2$, blue) distributions, for $\sigma = 10$, $\varphi = 0$. The full solution of the Aubry-André model (dots) is compared with the predictions of an analytic three-mode approximation (full lines) and a semi-analytic five-mode approximation (dashed line).*

frequency from the time evolution of the central peak of the quasi-momentum distribution. The signal is Fourier transformed, and the oscillation frequency is identified as the dominant component of the frequency spectrum. The obtained result is plotted in Fig. 3.9 as a function of λ (red points for $\lambda < 2$).

These oscillations can be interpreted by means of a simple analytical model that leads to an analytical expression for the oscillation frequency. Let us consider the time evolution in the quasi-momentum space as described by Eq. (3.28). We assume that the width $1/\sigma$ of the initial quasi-momentum distribution is small enough, so that only the $\xi = 0$ momentum component can be considered populated at $t = 0$ ($f_\xi(0) = \delta_{\xi,0}$). This assumption is valid when $1/\sigma \lesssim 2\pi\alpha$. We also assume that the time evolution couples the momentum component at $\xi = 0$ with only two other momentum components at $\xi = \pm 2\pi\alpha$. In this way, the Aubry-André equation in quasi-momentum space is mapped into an eigenvalue problem of a 3×3 matrix, whose eigenvectors and eigenvalues can be written as $g_{\xi,j}$ and E_j, respectively, with $j = 1, 2, 3$. The initial condition is $f_\xi(0) = \sum_{j=1}^{3} \gamma_j g_{\xi,j}$, where the coefficients γ_j are given by the standard rules of quantum mechanics. Under these assumptions one has $\gamma_{j=3} \equiv 0$, and the time evolution takes the form

$$|f_\xi(t)|^2 = (\gamma_1 g_{\xi,1})^2 + (\gamma_2 g_{\xi,2})^2 + \gamma_1 \gamma_2 g_{\xi,1} g_{\xi,2} \cos\left[(E_2 - E_1)t\right] . \qquad (3.30)$$

This expression describes a time-periodic oscillation of the relative intensity of the central and side peaks, with frequency $\nu(\lambda < 2) = |E_2 - E_1|/2\pi$, given by

$$\nu(\lambda < 2) = \pi^{-1}\sqrt{[1 - \cos(2\pi\alpha)]^2 + \lambda^2/2} . \qquad (3.31)$$
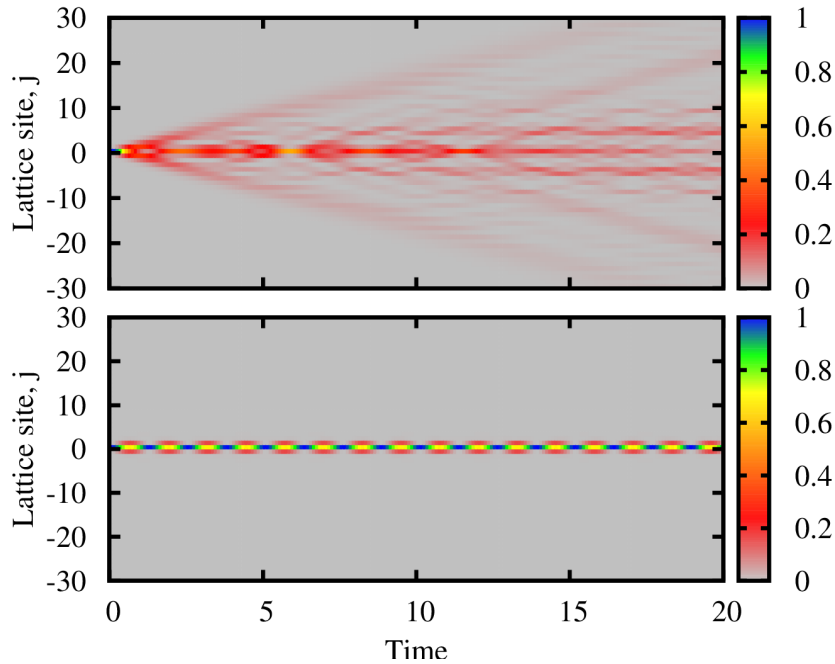
Figure 3.10: *Spatial distribution $|\psi_n|^2$ obtained from the solution of Eq (3.19) using a single site initial condition $\psi_j = \delta_{j,0}$. As in Fig. 3.8, we use $\alpha = 0.2282...$ and $\varphi = 0$. Time is given in dimensionless units. Top panel: $\lambda = 1$, the initially localized wavepacket spreads ballistically and there are no visible periodic oscillations. Bottom panel: $\lambda = 5$, the wavepacket is localized and a periodic oscillation of the central peak and its nearest neighbors is clearly visible.*

It is worth stressing that, once α is fixed, this frequency depends only on the disorder strength λ, but not on the phase φ or on the width of the initial wavepacket σ. This three-mode approximation provides a reasonable description of the numerical results, as shown by the solid line for $\lambda < 2$ in Fig. 3.9. The three-mode approximation becomes inaccurate when approaching $\lambda = 2$, where more modes are coupled during the evolutions. In order to check this effect, one can go one step further and consider a five-mode approximation in which the time evolution couples the quasi-momentum components at $\xi = 0$, $\xi = \pm 2\pi\alpha$, and $\xi = \pm 4\pi\alpha$. This is a straightforward generalization of the three-mode approximation, except for the fact that the differential equations for the coefficients $\gamma_j(t)$ do not yield simple analytical expressions and, moreover, the solutions contain several oscillation frequencies. The red dashed line in the $\lambda < 2$ part of Fig. 3.9 is our numerical result for the dominant component of the frequency spectrum, solution of the five-mode approximation, which mostly determines the time evolution of the central peak. As expected we get a better agreement with the full integration of Eq (3.19) compared to the three-mode approximation, especially in the region close to the transition point $\lambda = 2$.

In the region $\lambda > 2$ the few-mode approximation is expected to fail in the
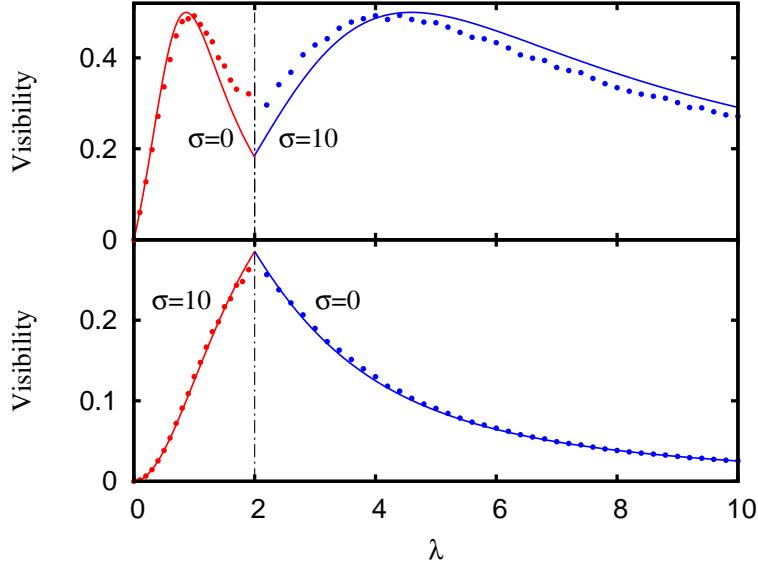
Figure 3.11: *Visibility of the oscillations in real and quasi-momentum space as a function λ, for $\varphi = 0$. The numerical points are compared with the three-mode approximation (full lines). Bottom panel: only few modes have been initially populated by using a δ-function initial wavepacket in real space and a Gaussian with $\sigma = 10$ in momentum space. Top panel: many modes have been initially populated by inverting the initial conditions with respect to the bottom panel.*

quasi-momentum space, where the wavepacket is no more localized. Indeed, in this regime, we do not see any significant evidence of periodic behaviors in the quasi-momentum distribution (see the bottom panel of Fig. 3.8). Conversely, owing to the duality of the Aubry-André model, one expects periodic oscillations to take place in real space, where the wavepacket is localized. This is confirmed by our numerical integration of Eq. (3.19), as shown in Fig. 3.10. In the top panel the wave packed spreads ballistically and one cannot detect any significant periodic behaviour; conversely in the bottom panel the wavepacket is localized, while the central peak and its nearest neighbours oscillate periodically. By assuming that the initial density distribution is localized in a single lattice site, $j = 0$, which is coupled with the nearest neighboring sites, $j = \pm 1$, we obtain a three-mode approximation analogous to the one used before in quasi-momentum space, but describing oscillations in the spatial distribution. The scenario in real space is more complicated because one generally observes oscillations with several frequency components, which also depend on the phase φ. However, in the special case $\varphi = 0$, one finds just a single frequency, given by

$$\nu(\lambda > 2) = (2\pi)^{-1}\sqrt{\lambda^2[1 - \cos(2\pi\alpha)]^2 + 8}\,, \qquad (3.32)$$

which is shown as the solid line for $\lambda > 2$ in Fig. 3.9. In the same figure we also plot the frequency obtained from the full numerical integration of Eq. (3.19) (blue dots

in the $\lambda > 2$ region); in this calculation we have used a Gaussian of width $\sigma = 10$ as initial shape of the wavepacket, but we have also checked that the frequency ν does not depend on σ, except close to $\lambda = 2$. The dashed line is the result of a straightforward semi-analytic extension to five modes, as in the $\lambda < 2$ region. It is worth stressing that the condition for the validity of the few-mode approximation for the oscillations in real space ($\psi_j = \delta_{j,0}$ or, equivalently, $\sigma \lesssim 1$) is much more constraining than the one in momentum space ($1/\sigma \lesssim 2\pi\alpha$) from the point of view of experimental realization.

   The amplitude of the oscillations in both real and momentum space also changes with λ, affecting its visibility. The latter can be calculated from the frequency spectrum of the numerical solution of Eq. (3.19), as the ratio between the modulus of the Fourier component of frequency $\nu(\lambda)$ and the modulus of the component at zero frequency. In a consistent way, one can define the visibility in the three-mode approximation; for the oscillations in momentum space for $\lambda < 2$, the visibility can be written as

$$\mathcal{V} = \frac{1}{2}\frac{\gamma_1\gamma_2 g_{0,1} g_{0,2}}{(\gamma_1 g_{0,1})^2 + (\gamma_2 g_{0,2})^2}. \tag{3.33}$$

A similar definition can be given in real space for $\lambda > 2$. In Fig. 3.11 we show the visibility of the oscillations as a function of λ. The points are the numerical results, while the lines represent the three-mode approximation. We have used two values for the width of the initial Gaussian wavepacket, namely $\sigma = 0$ (i.e., a δ-function) and $\sigma = 10$. In the upper panel, the two values of σ are used for $\lambda < 2$ and $\lambda > 2$, respectively. They correspond to a broad initial wavepacket both in momentum space for $\lambda < 2$ and real space for $\lambda > 2$. In the bottom panel we use again the same values of σ, but in the opposite regions, so to have a narrow initial wavepacket in both spaces [2]. One can see that the visibility depends significantly on both σ and λ. Again, the three-mode approximation is qualitatively correct, except near $\lambda = 2$. We observe that the three-mode approximation gives a better agreement for a narrow initial distribution (lower panel), as in the opposite case of a broad distribution many modes are initially excited and this approximation is not expected to be accurate. Another interesting feature is the effect of the duality of the Aubry-André model. Indeed, in both panels, the results in the region $\lambda < 2$ almost coincide with those in the region $\lambda > 2$ under the change of variable $\lambda \to 4/\lambda$, provided the initial distributions are broad (upper panel) or narrow (lower panel) in both momentum and real spaces; this duality also implies the continuity at $\lambda = 2$.

3.4.3   Detecting the Aubry-André transition in momentum space

So far we have seen that the time evolution of a wavepacket in the Aubry-André model exhibits interesting periodic behaviors both in momentum space, for $\lambda < 2$, and in real space, for $\lambda > 2$. Let us stress few differences between our analysis in momentum and real space. First, in momentum space the frequency of the

---

[2]For $\sigma = 10$, the momentum width $1/\sigma$ is much smaller than the distance between coupled modes, $\Delta\xi = 2\pi\alpha$.
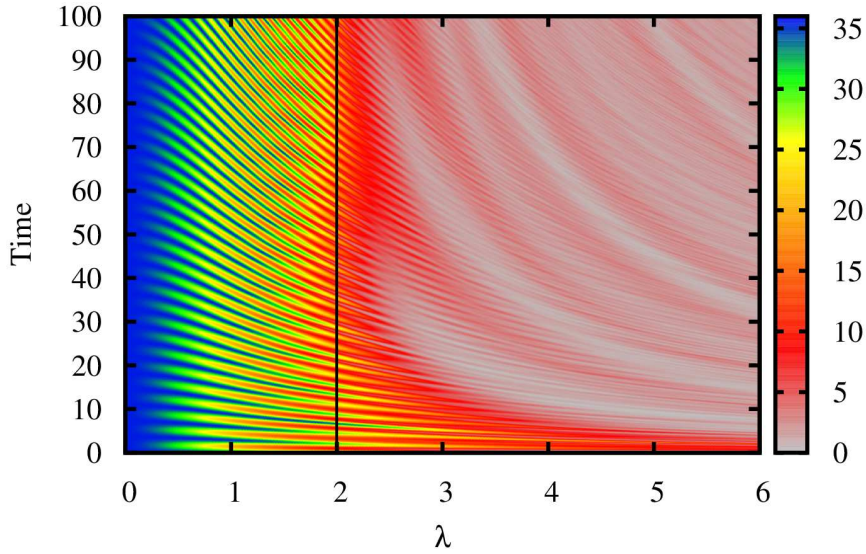
Figure 3.12: *Phase-averaged intensity of the central peak in momentum space,* $|f_0(t)|^2$, *as a function of time and disorder strength* λ *for a wavepacket with* $\sigma = 10$. *The intensity is given in arbitrary units.*

oscillations does not depend on the relative phase φ of the two lattices or, in other terms, on the initial position of the wavepacket, while this is not the case for real space. Getting rid of the phase dependence is positive since it is a parameter which would be hardly controllable in typical experiments. Second, the condition for the applicability of the few-mode approximation is less restrictive in momentum space, since the width of the initial wavepacket can be easily made smaller than the coupling distance between modes.

This observations suggest that the oscillations of the central and side peaks in the momentum distribution can be efficiently used to probe the transition from diffusion to localization in the Aubry-André model. A possible strategy consists of measuring the intensity of the central peak as a function of time for different values of λ, exploiting the fact that for $\lambda > 2$ the oscillations are phase dependent, while for $\lambda < 2$ they are not. Actually, in typical experiments with ultracold atoms, the phase φ varies at random at each realization, so that performing an average over many realizations at fixed λ is equivalent to an average over numerical simulations with different φ. Thus one expects that the oscillations vanish for $\lambda > 2$ (phase sensitive regime), but remain clearly visible for $\lambda < 2$ (phase independent regime). This is shown in Fig. 3.12, where the average has been done over 50 different values of the phase φ for each value of λ. Indeed the behavior of $|f_0(t)|^2$ exhibits a transition at $\lambda = 2$. From the same figure one can also extract the frequency $\nu(\lambda < 2)$. By using the experimental parameters of Ref. [67], with $\alpha = 1064.4/866.6$ and $\lambda = 1$, the oscillation period turns out to be of the order of 5 ms. This is a time of the order of the duration of typical experiments with ultracold atoms and that can therefore

be easily measured.

Weakly interacting bosons in quasiperiodic potentials

In the previous chapter we have discussed the diffusion and the localization properties of noninteracting particles in a 1D quasiperiodic potential. Now we want to proceed further by considering the more general case of interacting particles, having in mind the application to ultracold gases. Whether and in which way interaction between particles can affect the localization and diffusion properties of the system is a longstanding issue, which was raised at the very beginning of the story of Anderson localization [29]. This is, for instance, a natural question if one wants to study the conductance of electrons in a disorder material where interactions are intrinsically present and cannot be removed.

Ultracold gases represent a powerful tool for the study of this interplay. In fact both the strength of the interaction and of the disorder can be easily tuned in experiments. The former using Feshbach resonances, the latter acting on the intensity of the laser light that produces the optical disorder [27, 28, 98, 67, 68, 33].

From the theoretical point of view, various approaches can be used to study a weakly interacting Bose gas in a 1D disordered system. For instance, a possible method consists of considering the transmission of a Bose-Einstein condensate in a disorder region of finite extent [99, 100, 101]. Another possibility corresponds to consider the properties of a Bose gas at equilibrium which is confined in a box of finite size [102, 103, 104, 105, 106]. In this chapter, instead, we will study this interplay by considering the expansion of a Bose-Einstein condensate into a disordered potential. The experimental configuration that we have in mind is similar to the one that has been used for the observation of Anderson localization [24, 25] but this time controlling also the interaction between atoms. More precisely we treat the interaction within a mean field approach, which is known to be very effective for the description of weakly interacting Bose gases [107], and we consider a bichromatic optical lattice that introduces the exponential localization in absence of interaction among particles. This problem can be efficiently modelled using the discrete nonlinear Schrödinger equation as we will show in section 4.1. Our choice of this model of (quasi-)disorder is motivated by its close relation with the experimental setup used in Ref. [25] for the observation of Anderson localization, which is particularly suitable for the inclusion of interactions [67, 68, 33]. Notably, this approach is relevant also for experiments with light propagation in photonic lattices, where a nonlinear interaction term can be introduced using a Kerr media [65, 66].

The main result that we obtain is that the spreading behaviour is determined

by the competition between two different effects introduced by the interaction: on the one hand it favours localization through the self-trapping mechanism, on the other hand it destroys the localization induced by disorder leading to a subdiffusive expansion of wavepackets. These two effects will be discussed in sections 4.2.1 and 4.2.2 respectively. We also investigate the role played by the initial shape of the condensate in the dynamics of the system. Our calculations show that, if the condensate initially occupies a single lattice site, the dynamics of the gas in the lattice is dominated by self-trapping in a wide range of parameters, even for weak interaction. Conversely, if the diffusion starts from a condensate with Gaussian shape, extended over several lattice sites, self-trapping is significantly suppressed and the destruction of localization by interaction is more easily observable. Finally in section 4.3, we compare the results of our numerical simulations with an experimental study of the spreading of a weakly interacting Bose-Einstein condensate in a bichromatic optical lattice [33].

4.1   Discrete nonlinear Schrödinger equation

In this section we show that a gas of weakly interacting ultracold bosons, in the presence of a one dimensional bichromatic optical lattice and a tight harmonic confinement in the radial direction, can be described by means of a discrete nonlinear Schrödinger equation (DNLS).

It is known that a Bose-Einstein condensate of weakly interacting bosons at zero temperature can be conveniently described by the Gross-Pitaevskii (GP) equation [107, 108, 109, 110, 111]

$$i\hbar\frac{\partial\Psi(\vec{r},t)}{\partial t} = -\frac{\hbar^2}{2m}\nabla^2\Psi(\vec{r},t) + V(\vec{r})\Psi(\vec{r},t) + g|\Psi(\vec{r},t)|^2\Psi(\vec{r},t), \qquad (4.1)$$

where $\Psi(\vec{r},t)$ is a complex function that represents the condensate wavefunction. Its modulus square is the density of particles and the total number of particles is given by

$$\int|\Psi(\vec{r},t)|^2\,d\vec{r} = N. \qquad (4.2)$$

The quantity g is a coupling constant which accounts for the interaction between atoms and is determined by the s-wave scattering length a_s by

$$g = \frac{4\pi\hbar^2 a_s}{m}. \qquad (4.3)$$

For the external potential $V(\vec{r})$ let us consider a tight harmonic confinement in the transverse plane and a one dimensional bichromatic optical lattice in the axial direction. If the radial confinement is strong enough one can assume that the radial motion is completely frozen and that all the dynamics takes place in the axial direction. In this case the condensate wavefunction can be written as $\Psi(\vec{r},t) = \sqrt{N}\psi(x,t)\Phi_\perp(\vec{r}_\perp)$ where the wavefunctions $\psi(x,t)$ and $\Phi_\perp(\vec{r}_\perp)$ are normalized to unity. This factorization is a good approximation as long as the separation between

the ground state and the first exited state of the radial harmonic confinement $\hbar\omega_\perp$ is large compared to the other energy scales of the system such as the thermal energy or the mean field interaction energy.

Integrating out the radial direction and dropping some constant terms Eq. (4.1) can be reduced to a one dimensional Gross-Pitaevskii equation with a renormalized coupling constant [112, 113]

$$i\hbar\frac{\partial\psi(x,t)}{\partial t} = -\frac{\hbar^2}{2m}\frac{\partial^2}{\partial x^2}\psi(x,t) + V_b(x)\psi(x,t) + Ng_{1D}|\psi(x,t)|^2\psi(x,t), \qquad (4.4)$$

where $V_b(x)$ is the one-dimensional bichromatic optical lattice defined by Eq (3.1) and g_{1D} is an effective one-dimensional coupling constant given by

$$g_{1D} = g\int|\Phi(\vec{r}_\perp)|^4\,d\vec{r}_\perp. \qquad (4.5)$$

At this point one can follow a discretization procedure similar to the one that we have described in section 3.1. By decomposing the wavefunction on the basis of Wannier states of the primary lattice, $\psi(x) = \sum_j \psi_j w_j(x)$, one finds that Eq. (4.4) transforms into an equation for the evolution of the coefficients ψ_j, that is

$$i\hbar\frac{\partial\psi_j}{\partial t} = -J(\psi_{j+1} + \psi_{j-1}) + \Delta\cos(2\pi\alpha j + \varphi)\psi_j + NG|\psi_j|^2\psi_j \qquad (4.6)$$

where the tunneling energy J and the strength of the potential Δ are given by Eq. (3.6) and Eq. (3.8) respectively while G is related to g_{1D} through

$$G = g_{1D}\int|w_j(x)|^4\,dx. \qquad (4.7)$$

Finally, by expressing energy in units of J and time in units of $\hbar/(JE_{R_1})$, we obtain the discrete nonlinear Schrödinger equation

$$i\frac{\partial\psi_j}{\partial t} = -\psi_{j+1} - \psi_{j-1} + V_j\psi_j + \beta|\psi_j|^2\psi_j \qquad (4.8)$$

with $V_j = \lambda\cos(2\pi\alpha j + \varphi)$, $\lambda = \Delta/J$ and

$$\beta = NG/J. \qquad (4.9)$$

This equation is a discretized version of the usual GP equation and is of great importance for what follows since it will be studied in detail in this and in the next chapter of this thesis. Similar versions of a discretized Gross-Pitaevskii equation have been already used to investigate the dynamics of condensates in different situations (see for instance Ref. [114]). Within this mean-field description the interatomic interaction is included just by adding a nonlinear term in the equation of motion, therefore in the following we will use the terms interaction and nonlinearity interchangeably.

Let us stress that the dimensionless parameters λ and β which represent the strength of the quasi-disorder and of the mean-field interaction, respectively, are

the two key parameters that determine the properties of Eq. (4.8). We note that there are two conserved quantities associated to Eq. (4.8), the first is the norm $\mathcal{N}$ of the one dimensional condensate wavefunction ψ_j

$$\mathcal{N} = \sum_j |\psi_j|^2, \tag{4.10}$$

that in our case is always equal to 1, and the second is the energy of the system

$$H = \sum_j -(\psi_{j+1}\psi_j^* + \psi_{j+1}^*\psi_j) + V_j|\psi_j|^2 + \frac{1}{2}\beta|\psi_j|^4. \tag{4.11}$$

The first two terms in this expression represent the linear part of the energy, in particular the first is the kinetic energy while the second is the potential energy. The third term represents the nonlinear part and it is often called the mean-field interaction energy [107].

4.2   Effects of the interaction

We study the effects introduced by the interaction mainly by studying the time evolution of an initially localized wavepacket as done for the noninteracting case in section 3.3. We solve Eq. (4.8) using a RK4 algorithm and as initial condition we use both single site δ-function wavepackets and Gaussian wavepackets of initial width σ (cfr. section 3.3). Let us recall that in the case of noninteracting particles ($\beta = 0$) the evolution is governed by the Aubry-André Hamiltonian and a transition occurs at $\lambda = 2$ from an extended regime ($\lambda < 2$), where wavepackets expand ballistically, to a localized regime ($\lambda > 2$), where wavepackets remain localized after a transient initial expansion.

In the following we discuss two effects introduced by the interaction, namely self-trapping, which tends to locally trap part of the wavepacket, and the destruction of Anderson localization, which induces spreading. These two competing effects have to be carefully analysed in order to correctly interpret the expansion of a wavepacket.

4.2.1   Self-Trapping

Self-trapping is a localization phenomenon, different from Anderson localization, that occurs when the interaction is stronger than a critical value β_c. It is a quite general phenomenon that takes place also for a purely periodic system without disorder [114, 115, 116, 117] and double-well potentials [118, 119, 120, 121, 122]. An intuitive understanding of the origin of the self-trapping in a lattice is based on energy conservation arguments [123]. Let us consider separately the contribution to the energy that comes from the kinetic and potential terms together and the contribution that comes from the interacting term, $H = H_0(t) + H_{int}(t)$ where

$$H_0(t) = \sum_j -(\psi_{j+1}\psi_j^* + \psi_{j+1}^*\psi_j) + V_j|\psi_j|^2 \quad \text{and} \quad H_{int}(t) = \sum_j \frac{1}{2}\beta|\psi_j|^4. \tag{4.12}$$
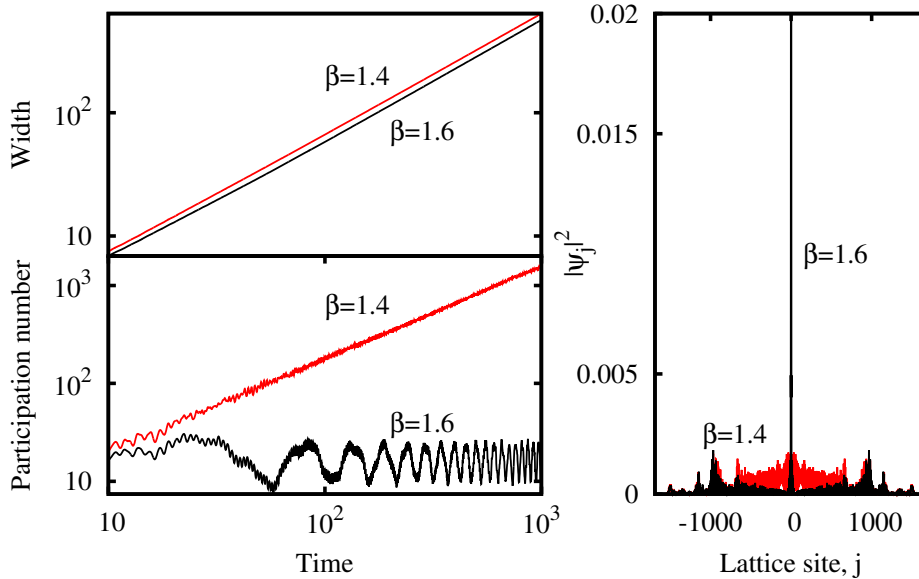
Figure 4.1: *Width $w(t)$, participation number $P(t)$, and density distribution $|\psi_j(t = 1000)|^2$ for two values of the interaction strength β, below ($\beta = 1.4$, red lines) and above ($\beta = 1.6$, black lines) the transition from diffusion to self-trapping. Here the initial state is a single-site δ-function with $\varphi = 0$ and $\lambda = 0.8$.*

If the gas is subject to a periodic potential in the tight-binding approximation and its dynamics is restricted to the lowest Bloch band, as supposed in deriving Eq. (4.11), the term H_0 in the Hamiltonian is upper bounded. Let us call this upper bound E_0^{max} [1]. Whenever the energy of the interacting system is larger than this upper bound, $H > E_0^{max}$, one can prove that the system cannot reach a situation where $H_{int}(t) = 0$, at any $t > 0$, without violating energy conservation. This means that, under these conditions, part of the interaction energy must be trapped in the system in the form of a localized peak that does not spread. In other words, whenever $H > E_0^{max}$ an initially localized wavepacket cannot spread to zero in the whole space. This argument, in general, does not provide a precise quantitative estimate of the critical value β_c, but it gives a reasonable upper bound.

Self-trapping of particles in the context of the discrete nonlinear Schrödinger equation has been studied for different types of external potentials such as periodic potentials [116], quasiperiodic [116, 124, 125] potentials and random potentials [123, 126]. In particular a 1D quasiperiodic potential of the same type as (3.11) for $\lambda \leq 2$ has been already discussed in Ref. [116, 124]. Here we provide a more systematic calculation of β_c and we compare the diffusion from a single-site to the one from a Gaussian wavepacket.

A signature of the presence of self-trapping is a saturation of the participation

---

[1] Due to the symmetry of the problem the upper bound of the spectrum is given by the width of the full spectrum, Δ, divided by two, $E_0^{max} = \Delta/2$,

number $P(t)$ that, for $\beta > \beta_c$, reaches an asymptotic finite value, due to the trapping mechanism occurring at the center of the wavepacket, while the width $w(t)$ keeps increasing owing to the expanding tails [116, 123]. An example of self-trapping transition is shown in Fig. 4.1, where we show the results obtained by solving Eq. (4.8) for diffusion from a single-site in a quasiperiodic potential with $\alpha = (\sqrt{5}-1)/2$ and $\lambda = 0.8$. In the figure one can see the typical change of behaviour that occurs when β crosses the critical value β_c that for the example shown in figure is approximately equal to 1.5. The same figure shows also the difference in the density distributions at $t = 1000$. For $\beta = 1.4$ (red lines), below the critical value β_c both the width and the participation number grows ballistically and no signatures of self-trapping can be detected in the shape of the packet. Instead for $\beta = 1.6$ (black lines), above the critical value β_c, the presence of a strongly localized self-trapped peak is clearly observable in the central part of the wavepacket. This leads to a strong difference in the behaviour of the participation number that saturates to a constant value after a transient time. The lateral, low density tails of the wavepacket are instead similar in the two cases resulting in a similar behaviour of the width.

Let us stress here that self-trapping, even if it is a phenomenon that leads to localization, is completely different from Anderson localization. First of all the crucial point for the occurrence of self-trapping is the presence of interactions and of an upper bounded spectrum. Therefore, it can be observed in a variety of different systems, regardless of the presence of disorder. Conversely, Anderson localization takes place in presence of disorder and for noninteracting particles. Secondly self-trapping leads only to a partial localization since the central part of the wavepacket remains localized while its tails keep expanding. Again this is completely different from Anderson localization where a complete stop of the expansion takes place and the tails decrease exponentially to zero.

We now study in detail the self-trapping transition within the quasiperiodic model defined by Eq. (4.8) when the disorder strength is varied across the transition point at $\lambda = 2$ considering a single site-initial condition and different values of the phase of the potential φ. By systematically looking at the numerical results for $w(t)$, $P(t)$, $|\psi_j(t)|^2$ in the β vs. λ plane, we can identify the set of parameters for which self-trapping takes place and obtain the diagram shown in Fig. 4.2. The values of β_c are represented by red circles and blue squares for $\varphi = \pi$ and 0, respectively.

We have identified three different regions corresponding to three different behaviours in the diagram. In region I, above the red circles, all points correspond to self-trapped states. For $\lambda < 2$ we find that the value of β_c is practically independent of the phase φ and decreases as λ is increased. In region II, we observe diffusion, often accompanied by solitonic structures and discrete breathers eventually spreading. Similar structures in the numerical solutions of Eq. (4.8), for diffusion from a single-site and for $\lambda = 0$, have been already found in Ref. [116]. For $\lambda > 2$ we find that β_c is strongly φ-dependent. In the figure we show the results for the two limiting values $\varphi = 0$ and $\varphi = \pi$; in particular, in region III, we find that all states are self-trapped for $\varphi = 0$ while they are diffusive for $\varphi = \pi$. The semi-axis $\lambda > 2$ and $\beta = 0$ corresponds to the regime of disorder induced localization for noninteracting
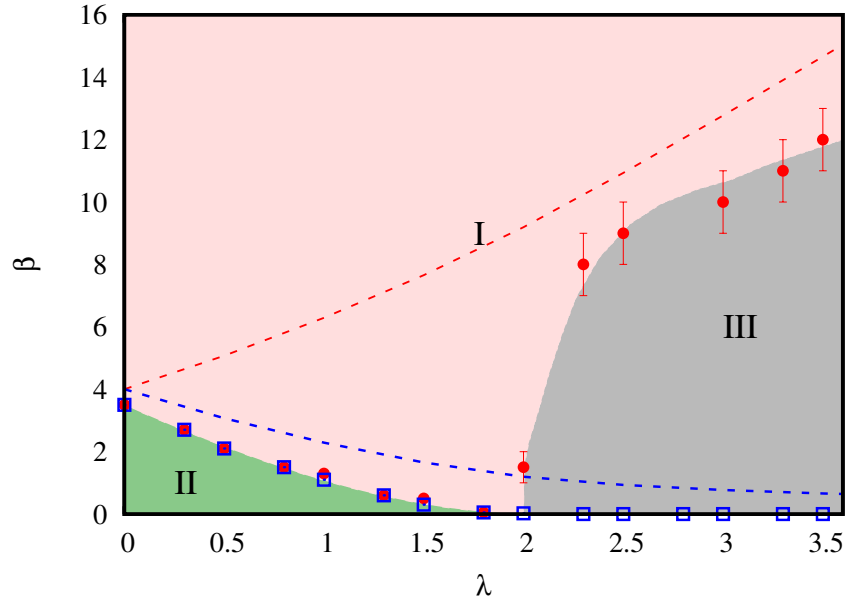
Figure 4.2: *Critical value of the interaction strength for the transition to self-trapping, β_c, as a function of the disorder strength, λ, for diffusion from a single lattice site and for $\varphi = \pi$ (red circles) and $\varphi = 0$ (blue squares). The red and blue dashed lines are the corresponding upper bounds for β_c obtained by calculating the bandwidth of the single-particle spectrum and using energy conservation arguments. The diagram is schematically divided in three regions I, II and III. All states in I are self-trapped; in II, one finds diffusion, with soliton-like structures and discrete breathers; in III, the transition from diffusive states to self-trapping strongly depends on the value of the phase φ (i.e., the position of the initial wavepacket). The semi-axis $\lambda > 2$ and $\beta = 0$ corresponds to the regime of disorder induced localization for noninteracting particles.*

particles.

The phase dependence of β_c for $\lambda > 2$ can be qualitatively explained by the energy conservation arguments already mentioned above. In particular, we numerically calculate the maximum energy, E_0^{max}, in the lowest Bloch band of the noninteracting single-particle spectrum and we compare this value to the initial energy of the interacting system, which is given by $H = \lambda \cos(\varphi) + \beta/2$. The upper bound for the transition to self-trapping is then given by the condition $H = E_0^{max}$, which implies

$$\beta = 2(E_0^{max} \pm \lambda)$$

where the plus and the minus signs holds for $\varphi = \pi$ and $\varphi = 0$, respectively. These two upper bounds are represented by the blue and red dashed lines in Fig. 4.2.

Fig. 4.2 shows that, in the case of diffusion from a single-site, the self-trapping mechanism plays a rather important and nontrivial role, leaving almost no space
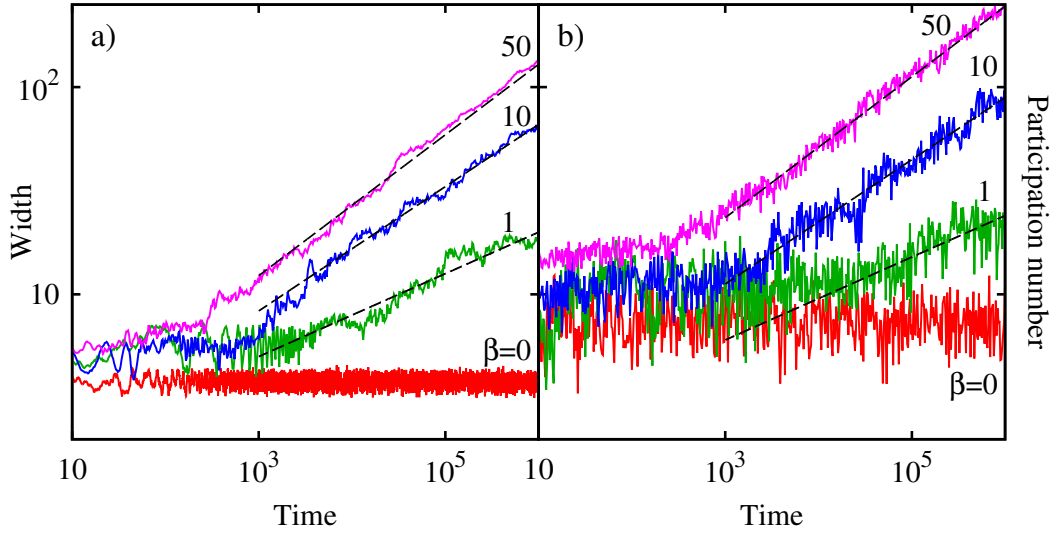
Figure 4.3: *Time evolution of the width of the wavepacket $w(t)$ (a) and of the participation number (b) for $\lambda = 2.5$ and for an initial Gaussian wavepacket with $\sigma = 5$. We compare the noninteracting case, $\beta = 0$, with three interacting cases: $\beta = 1, 10, 50$. The black dashed lines represent a guide to the eye. Their slope is 0.2, 0.3 and 0.34 and is the same in (a) and (b).*

to the observability of the interplay between disorder and interaction. The region were this interplay might be observed, namely for $\lambda > 2$ and small β, where one expects to see the destruction of localization due to interaction, it is also the region where the dependence on the phase φ is the largest. Unfortunately, in typical experimental situations with Bose-Einstein condensates, the phase φ is not controllable. Moreover, in the experiments the initial distribution of atoms in the lattice sites is more similar to a Gaussian than a δ-function. This suggests that, while the single-site diffusion is conceptually important and widely investigated from the theoretical viewpoint, the diffusion from a Gaussian is also interesting and worth exploring.

4.2.2   Destruction of Anderson localization

Let us now consider the effects of the interaction on the expansion of a wavepacket, in a regime where all the single particle eigenstates are localized ($\lambda > 2$). We choose the system parameters in order to rule out self-trapping so that the interplay between interaction and disorder induced localization can be investigated. As initial wavepacket we use a Gaussian distribution with a size that is larger than the typical size of the eigenstates of the linear system. This choice is convenient since it strongly suppresses the dependence of the dynamics of the system on the lattice phase φ. This leads to a simpler analysis of the interplay between the two key parameters λ and β.

The main result of our observations is that, as the interaction is turned on, a wavepacket that was localized for $\beta = 0$ starts to expand subdiffusively. We observe an asymptotic growth of both the width $w(t)$ and the participation number $P(t)$, according to the following laws:

$$w(t) \sim t^{\gamma_1} \qquad\qquad P(t) \sim t^{\gamma_2} \qquad\qquad (4.13)$$

with γ_1 and γ_2 in the range $0 - 0.5$. Let us recall that ballistic expansion would correspond to $\gamma = 1$ and normal diffusion to $\gamma = 0.5$. In the absence of self-trapping we find that the coefficients γ_1 and γ_2 are nearly equal, therefore in the following we will use $\gamma \approx \gamma_1 \approx \gamma_2$. A typical example of the observed delocalization process is shown in Fig. 4.3. The effect of the interaction is studied considering the diffusion of an initial Gaussian wavepacket with $\sigma = 5$ and a disorder strength just above the localization transition $\lambda = 2.5$. The noninteracting case, which remains localized, is compared with three different values of the interaction parameter, $\beta = 1$, $\beta = 10$ and $\beta = 50$. Already for $\beta = 1$ there is an evident delocalization and this effect increases as β is increased in the sense that γ becomes larger and the delocalization takes place earlier. The three black dashed lines represent a guide for the eyes. They represent an asymptotic spreading law of the type described by (4.13) with spreading exponents γ equal to 0.2 ($\beta = 1$), 0.3 ($\beta = 10$) and 0.34 ($\beta = 50$) and they are the same in panel (a) and in panel (b). The presence of these lines stresses the fact that the exponent changes as the value of the interaction strength is increased and suggests the equality between the spreading exponents for $w(t)$ and $P(t)$. A very similar behaviour is obtained also for the diffusion from a single-site, provided the phase φ and the interaction β are chosen in such a way to avoid self trapping (e.g., in region III of Fig. 4.2 with $\varphi = \pi$). When the disorder strength λ is increased the localization gets more robust, in the sense that the onset of subdiffusive spreading takes place for later times and γ becomes smaller. For large λ we reach a situation where the delocalization process is no longer observable within our simulation time. This is shown in Fig. 4.4, where we compare the time evolution of a Gaussian wavepacket for fixed β and for increasing values of the disorder strength λ.

Similar results on the dynamics of wavepackets in presence of Anderson localization have been recently reported for purely random systems [127, 128, 126, 129]. In these studies they considered the discrete nonlinear Schrödinger equation with on site energies that are given by an uncorrelated random sequence distributed according to a square distribution $V_j \in [-W/2, W/2]$. They numerically observed a subdiffusive expansion similar to the one that we have described in this section and suggested that the asymptotic value of the spreading exponent, in the case of a random potential, is universal and approximately equal to 1/6. A theoretical model that interpret the origin of the subdiffusive spreading as due to the presence of resonant modes inside the packet has been developed in [126, 129] and provides a value of the spreading exponent that agrees very well with the numerical one. More recently it has been shown that for large values of the nonlinear parameter a faster transient expansion can be observed where $\gamma = 1/4$ [130, 131, 132].
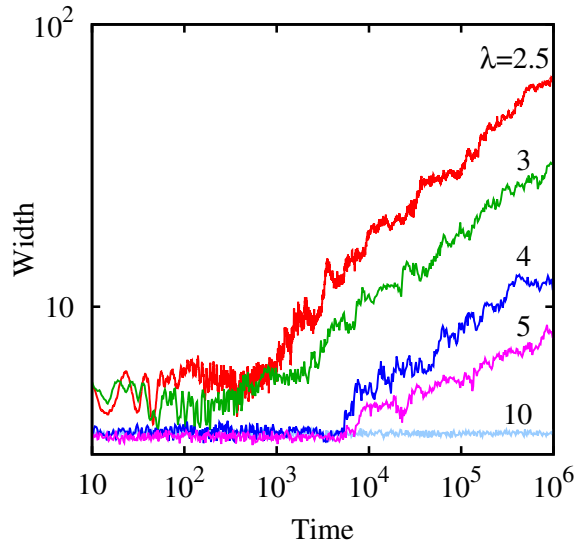
Figure 4.4: *Time evolution of the width of a Gaussian wavepacket with $\sigma = 5$, for $\beta = 10$ and different values of the disorder strength λ.*

As we have seen in this section, the results that we extract from Fig. 4.3 for the spreading exponents γ in a quasiperiodic potential are significantly larger than those found for purely random systems. In particular for the highest values of β here considered, the values of γ are larger than both $1/6$ and $1/4$. This suggests that the comparison of our results with those obtained for random systems is not so trivial and deserves a more detailed study. This issue will be addressed in the next section, as well as in the next chapter. In particular, in the next section we discuss the comparison between our theoretical predictions for the spreading exponent and the experimental results, while in the next chapter we will focus on the long-time asymptotic behaviour, making a bridge between the numerical results and the models of Refs. [126, 129, 130] applied to quasiperiodic systems.

4.3   Experimental observation of subdiffusion

In this section we introduce the experiment realized in Florence on the expansion of a cloud of interacting ultracold atoms in a bichromatic optical lattice [33] and compare the experimental results with the numerical ones obtained with the one-dimensional discrete nonlinear Schrödinger equation.

4.3.1   Experimental setup

Thanks to the great controllability of the relevant parameters in experiments with ultracold atomic systems, it has been possible to observe the expansion of a cloud of atoms in a controlled disorder and with a tunable interatomic interaction. The setup

is the same of previous experiments [24, 25]: the condensate is first produced and kept confined within a three dimensional harmonic trap; it is then loaded into an additional one-dimensional disordered potential; finally, by switching off the harmonic confinement along the axial direction, it is let free to expand into the disordered potential. The strength of the disorder can be controlled by acting on the intensity of the lasers that produce the potential, while the strength of the interatomic interaction is controlled by means of an external magnetic field, thanks to a Feshbach resonance. Using these two experimental "knobs", it is possible to change the two key parameters of the problem, thus allowing a detailed investigation of the interplay between interaction and disorder induced localization.

Let us now discuss more in detail the experimental procedure. A Bose-Einstein condensate of ^{39}K atoms is produced in an optical trap which gives a radial confinement of $2\pi \times 50$ Hz and an axial confinement of $2\pi \times 70$ Hz and contains about $N = 5 \times 10^4$ atoms. The disordered potential is experimentally realized using a one dimensional bichromatic optical lattice that can be described by Eq. (3.1)

$$V(x) = s_1 E_{R_1} \sin^2(k_1 x) + s_2 E_{R_2} \sin^2(k_2 x + \varphi). \qquad (4.14)$$

It is formed by superimposing two simple optical lattices of different wavelengths ($\lambda_1 = 1064.4$ and $\lambda_2 = 859.6$), each of them created by a laser field in the standing wave configuration. This potential is characterized by a lattice spacing $d = \lambda_1/2$, a tunneling energy J and a disorder strength Δ. The lattice beams provide an additional radial confinement of $\omega_\perp = 2\pi \times 50$ Hz.

The condensate is first loaded into a quasiperiodic lattice with a constant $\Delta = 3J$ and the scattering length is fixed at $a_s = 280a_0$. At a given time $t = 0$ the optical trap is suddenly switched off letting the interacting atomic cloud free to expand along the bichromatic optical lattice. At the same time, the disorder strength, Δ and the scattering length a_s are suddenly changed and tuned to their final values that will stay fixed for the rest of the expansion. The time evolution of the radially-integrated spatial distribution $n(x)$ of the atomic cloud is then monitored by in situ absorption imaging up to $t = 10$ s. The spreading is quantified by measuring the width of the atomic cloud which is calculated as the square root of the second moment of the spatial distribution

$$\sigma(t) = \sqrt{\int x^2 n(x)\, dx}, \qquad (4.15)$$

where the spatial distribution $n(x)$ has been normalized to one. The strength of the interaction is experimentally quantified by an estimation of the interaction energy per particle E_{int} of the cloud at $t = 0$, which is given by

$$E_{int} = g \frac{N_s}{2} \int |\phi(\vec{r})|^4\, d\vec{r} \qquad (4.16)$$

where $g = 4\pi\hbar^2 a_s/m$ is the coupling constant, N_s is the mean atom number per site and $\phi(\vec{r})$ is a Gaussian approximation of the single site wavefunction.
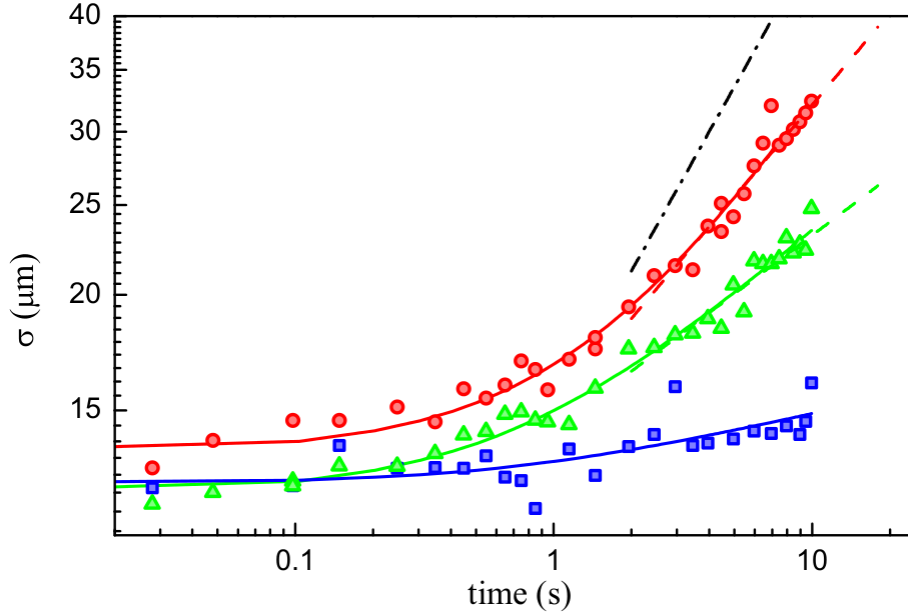
Figure 4.5: *Time evolution of the width σ of the expanding cloud for different initial interaction energies: $E_{int} = 0$ (squares), $E_{int} = 1.8J$ (triangles), and $E_{int} = 2.3J$ (circles). The continuous lines are the fit with Eq.(1). The dashed lines show the fitted asymptotic behavior, while the dash-dotted line shows the expected behavior for normal diffusion. The lattice parameters are $s_1 = 5$, $\Delta/J = 5$.*

The initial wavepacket is always created in the same experimental conditions, since it is independent from the final parameters of the expansion and it has been estimated to occupy on average $N_s = 20 \pm 7$ lattice sites. The typical disorder strength that is used in the experiment is $\lambda = \Delta/J \approx 5$. Let us note that we are in a regime where the size of the initial wavepacket is much larger than the localization length of the single-particle eigenstates L_{loc}. As a consequence we know that the behaviour of the wavepacket will be determined just by the disorder and the interaction strength and we can forget about the value of the phase φ between the two lattices.

In Fig. 4.5 we show a typical example of a set of experimental runs that measure the time evolution of the width of the expanding atomic cloud for $\lambda = 5$. We compare the noninteracting case $E_{int} = 0$ (blue squares) with two cases where the interaction is different from zero, $E_{int} = 1.8$ (green triangles) and $E_{int} = 2.3J$ (red circles). In absence of interaction the system is localized and the width essentially does not change in time. Only an extremely slow expansion can be detected, presumably due to technical noise. The noise is mostly provided by the vibrations of the retroreflecting mirrors used to create the two lattices that reflects in a disorder potential that changes with time. The introduction of a repulsive interaction allows the wavepacket to expand significantly: the expansion is however not ballistic since
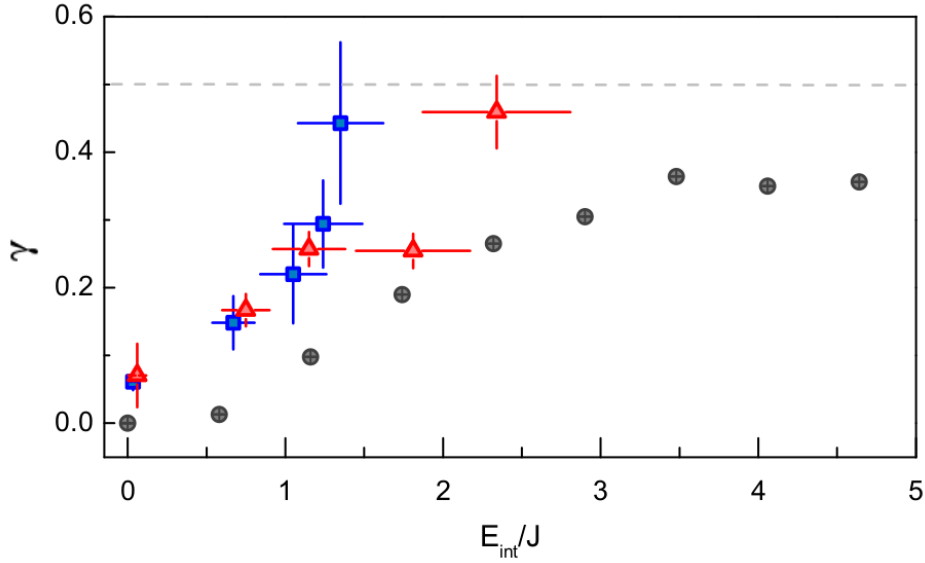
Figure 4.6: *Spreading exponent γ vs the initial interaction energy E_{int} in the experiment (triangles and squares) and simulations (grey circles). The experimental data are for $\Delta/J \approx 5$ and two different values of the depth of the main lattice: $s_1 = 7$ (red triangles) and $s_1 = 5$ (blue squares). The vertical bars are the fitting error of Eq.(1) to the data, while the horizontal bars indicate the statistical error.*

its velocity decreases during the time evolution, as the width of the cloud increases.

In order to characterize the spreading more in detail and classify the type of spreading behaviour, the experimental curves for the width σ are fitted with the following function

$$\sigma(t) = \sigma_0 \left(1 + \frac{t}{t_0} \right)^{\gamma} \tag{4.17}$$

with three fitting parameters σ_0, t_o and γ. Here σ_0 represents the initial width of the atomic cloud, t_0 is an "activation time" and γ is the exponent that characterize the type of spreading behaviour. We note that Eq. (4.17) reproduces the asymptotic behaviour $\sigma \sim t^{\gamma}$ that we have introduced with Eq. (4.13) and it has the additional advantage to extract information also from the measurements at short times. This allows to decrease the uncertainty on the parameters extracted from the fitting procedure. Notably Eq. (4.17) gives a good description of the behaviour of the atomic cloud also for short times.

The values of γ extracted from the fitting procedure are always smaller than 0.5 and are larger for increasing interaction strength. This indicates a subdiffusive expansion and confirms qualitatively the results presented in section 4.2.2. More precisely the values of the spreading exponent for $E_{int} \neq 0$ are in the range $\gamma \approx 0.2 - 0.4$. The results of a systematic investigation of the value of the spreading exponent are shown in Fig. 4.6 as a function of the interaction energy E_{int} and for

a fixed value of the disorder strength $\lambda = 5$. One can see a clear increase of γ with E_{int} up to $\gamma \approx 0.4$. The two set of points correspond to different values of the depth of the primary lattice $s_1 = 5$ (blue squares) and $s_1 = 7$ (red triangles). The fact that the two datasets lie approximately on the same curve indicates that the behavior of the system does not depend on the specific value of s_1 but just on the ratio between the two tight binding parameters Δ and J. This confirms that a tight binding formalism provides a good description of the experiment.

4.3.2   Comparison with the discrete nonlinear Schrödinger equation

Let us now compare the values of γ extracted from the experiment and those that can be obtained from the discrete nonlinear Schrödinger equation. In sections 3.1 and 4.1 we discussed how it is possible to connect a cloud of expanding atoms in a one dimensional bichromatic optical lattice to the discrete nonlinear Schrödinger equation and we gave a set of expressions (3.6), (3.8), (4.9) that allows to connect the experimental parameters to the one of the theoretical model.

We now write down the explicit expressions that we have used to connect the theoretical parameters with those of the experiment. Let us start considering the tunneling energy J. At present we know that J can be calculated using expression (3.6) and an estimation of the Wannier function $w(x)$. Anyway there is also another way to obtain the value of the tunneling energy using the fact that, in absence of an external potential, J is proportional to the bandwidth of the lowest band of the system. In particular an exact formula for the bandwidth, which is valid when $s_1 \gg 1$, yields $J = (4/\sqrt{\pi})E_{R_1}s_1^{3/4}\exp(-2\sqrt{s_1})$ [133]. An even more precise formula can be obtained by numerically solving the band structure and performing a fit to the calculated curves [134]

$$J = 1.43 E_{R_1} s_1^{0.98} e^{-2.07\sqrt{s_1}} \tag{4.18}$$

An estimation of the intensity of the quasiperiodic modulation Δ can be calculated by solving the integral in Eq. (3.8) using a Gaussian approximation for the Wannier functions, $|w(x)|^2 = (k_1/\sqrt{\pi})s_1^{1/4}\exp(-\sqrt{s_1}k_1^2 x^2)$ (see appendix A for more details); following this procedure one obtains $\Delta = (s_2 E_{R_2}/2)e^{-\alpha^2/\sqrt{s_1}}$. Also in this case a more accurate result can be obtained from a numerical calculation. More precisely, by replacing the Gaussian approximation of $w(x)$ with the numerically calculated Wannier functions one finds [91]

$$\Delta = \frac{s_2 E_{R_2}}{2} e^{-2.18/s_1^{0.6}}. \tag{4.19}$$

Finally the interaction parameter β is calculated starting from the experimental estimation of E_{int}. Within the discrete nonlinear Schrödinger equation, the interaction energy per particle in units of J is given by $E_{int}/J = (\beta/2)\sum_j |\psi_j|^4$. Recalling that the participation number gives an estimation of the lattice sites which are significantly occupied, $n_{site} \approx P = 1/\sum_j |\psi_j|^4$ we obtain an expression of β as a function
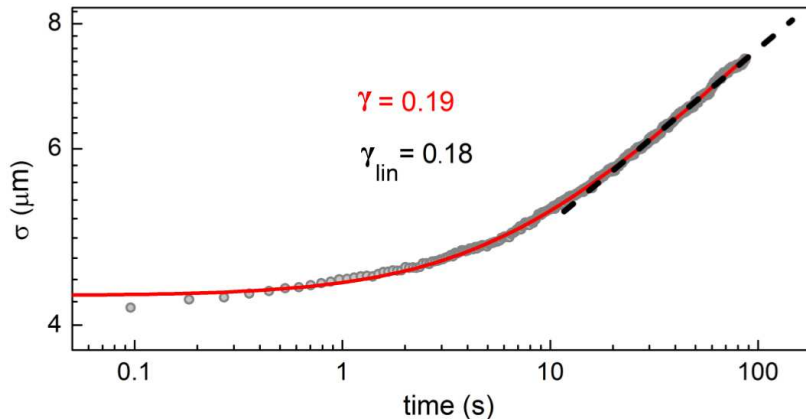
Figure 4.7: *Time evolution of the width of the expanding atomic cloud obtained solving the discrete nonlinear Schrödinger equation for $\lambda = 5$ and $E_{int} \approx 1.8$ (grey points). We also show the result of two different fitting procedures. The first is performed using Eq. (4.17) as a fitting function (red solid line). The second is the result of a linear fit in log-log scale done considering only the last part of the simulation.*

of E_{int}

$$\beta = 2n_{site}\frac{E_{int}}{J} \,. \tag{4.20}$$

Expressions (4.18), (4.19) and (4.20) create a direct and explicit connection between the experimental parameters and the theoretical ones and represent the equations that we use for the mapping from theory to experiment.

The initial wavefunction for the expansion is calculated solving a stationary version of the DNLS equation

$$-\psi_{j+1} - \psi_{j-1} + V_j\psi_j + \beta|\psi_j|^2\psi_j = \mu\psi_j \tag{4.21}$$

where V_j contains a contribution from the one dimensional bichromatic optical lattice and a contribution from the harmonic confinement along the axial direction.

In Fig. 4.6 we show the values of γ extracted from the numerical simulations (grey circles). The spreading exponent increases for increasing value of the interaction energy E_{int} and approaches a saturation value around 0.35. The calculation of γ has been done following the same procedure that has been used for the experimental data. First we compute the width of the wavepacket using Eq. (3.22) and then we fit the curve of the width as a function of time using Eq. (4.17) as a fitting function. A typical example of a numerical simulation for the width of the expanding wavepacket expressed in μm is shown in Fig. 4.7. The result of the fit is also shown (red solid line) in the figure. Typically the numerical simulations for $w(t)$ have been averaged over 40 different realizations (corresponding to different values of the phase shift φ)

before performing the fit. We also extracted the spreading exponents γ_{lin} by fitting the data points only for large times with the asymptotic expression (4.13) and we verified that the two fitting procedures give a good agreement. In Fig. 4.7 the black dashed line shows the result of the fitting with the asymptotic expression and the values of the two exponents are reported.

The numerical exponents shown in Fig. 4.6 are in qualitative agreement with the experimental ones. Note that the experimental measurements give a nonzero value of the spreading exponent $\gamma \approx 0.06$ even for $E_{int} \approx 0$. This is probably the result of a weak technical noise on the quasiperiodic potential, due to variations in the laser wavelengths and to vibrations of the retroreflecting mirror that creates the standing waves. If we would assume that this value represents a constant bias for all measurements with interaction then we would find an improved quantitative agreement between theory and experiment. A detailed analysis of quantum diffusion in presence of disorder, noise and interaction has been recently performed in [69] and seems to support the assumptions of an increase of γ due to the presence of the experimental noise.

There is however a disagreement on the typical interaction energy at which the saturation regime for the exponents γ is reached in the experiment and in the theory. Furthermore we observe that the activation time is much longer in the numerical simulations than in the experiment and this implies the need of a longer simulated expansions in order to get a numerical spreading comparable with the experimental one. These differences are mainly due to finite temperature effects and to a feature of the experimental setup which is not included in the discrete nonlinear Schrödinger equation that is the radial degrees of freedom. The use of the DNLS model implies that the radial degrees of freedom has to be completely frozen during the dynamics of the system. This is not the case for the experiment where many radial states are populated and play a role during the expansion. The situation is different for noninteracting samples where the different degrees of freedom can be completely decoupled and the radial dynamics does not influence the axial one. In presence of interaction the finite temperature and the presence of the radial degrees of freedom influences the dynamics and in particular leads to a faster expansion and to a smaller activation time [33].

Finally as regards a comparison of the spreading exponents obtained for the quasiperiodic case with those obtained for uncorrelated random potentials we confirm the observation of section 4.2.2. The exponents γ for the quasiperiodic case, extracted both from the simulations and from the experiment, are larger than the maximum value of the exponent that have been observed and theoretically predicted for random systems, that is 1/4. In the next chapter we will continue and conclude this discussion on the comparison with the random case and we will study the spreading exponent γ for asymptotic times, orders of magnitudes larger than the times that can be reached in present experiments with ultracold atoms.

Subdiffusion of nonlinear waves in quasiperiodic potentials

The topic of this chapter is again the interplay between interaction and Anderson localization in quasiperiodic systems. We still consider the dynamics of a wavepacket, but now our focus will be on the characterization of the subdiffusive spreading introduced by the interaction.

We have already seen in the previous chapters that exponential localization of noninteracting quantum particles (or linear waves) can occur in quasiperiodic systems and that the inclusion of interaction between particles changes localization into subdiffusive spreading. Theoretically, the interplay between interaction and Anderson localization, has been more often studied by considering wavepackets propagating in purely random potentials [123, 127, 128, 126, 129, 135, 130, 136, 137, 131, 132]. Also in this case, numerical simulations showed that the presence of nonlinearity indeed destroys localization and leads to a subdiffusive growth of the width of the wavepacket in time as $w(t) \sim t^{\gamma}$ [127, 128, 126, 129, 135, 136, 131, 132]. In particular it was predicted that at large t, the coefficient γ should converge to $1/6$ in a regime of so-called "weak chaos", as opposed to normal diffusion where $\gamma = 0.5$. A transient regime of "strong chaos" was also identified, where $\gamma = 1/4$ [130, 131, 132]. A comparison between the values of γ for the random case with those discussed in sections 4.2.2 and 4.3.2 for the quasiperiodic case clearly indicates that in the quasiperiodic case the typical spreading exponents are significantly larger, at least at finite spreading times.

The purpose of this chapter is to clarify the details of the spreading mechanism and address the differences and similarities between quasiperiodic and purely random potentials. We extend and refine our previous numerical investigations by pushing the simulations to much longer times, thus allowing for the identification of the strong and weak chaos regimes in quasiperiodic systems and compare the situation with known properties of purely random systems. For this purpose, we use two different models, namely the discrete nonlinear Schrödinger equation, that we have already introduced in section 4.1, and a quasiperiodic version of the quartic Klein-Gordon lattice model.

We anticipate here that a regime of weak chaos is indeed observed in the long time spreading of nonlinear wavepackets propagating in quasiperiodic systems; in particular we find that the asymptotic value of the spreading coefficient γ is $1/6$ as in purely random systems, thus showing that this behaviour is rather general and model independent. Another similarity with purely random systems is the

occurrence of self-trapping (cfr. section 4.2.1): when the nonlinear interaction is large enough to shift the mode frequencies so strongly that they are tuned out of resonance with all non-excited neighbouring modes, a part of the wavepacket remains spatially localized [123, 126, 31]. However as opposed to the random system, in the quasiperiodic case partial self-trapping is also possible for weaker nonlinearities. This is due to the complexity of the linear wave spectrum which exhibits a fractal gap structure of sub-bands. Self-trapping gives rise to transient spreading regimes characterized by an intermediate large exponent γ; we call this effect "overshooting". Finally, we have also observed signatures of strong chaos, but detection of this regime is difficult in quasiperiodic systems, since it is often masked by overshooting and partial self-trapping, which occur on the same temporal scales.

In section 5.1 we formulate the DNLS model in normal mode space. In section 5.2 we discuss the relevant energy scales for the prediction of the spreading behaviour of a wavepacket. In section 5.3 we summarize the different spreading regimes and discuss the spreading laws associated to each regime. In sections 5.4 and 5.5 we present and discuss the results of long time numerical simulations within the DNLS model. Finally in 5.6 we introduce the Klein-Gordon model and we show that the observed numerical results can be interpreted on the basis of the same theoretical model that it has been developed for the DNLS model.

5.1 DNLS in normal mode space

Let us start from the DNLS model with a quasiperiodic potential. The key equation, already introduced in section 4.1, is

$$i\frac{\partial \psi_j}{\partial t} = -(\psi_{j+1} + \psi_{j-1}) + V_l\psi_j + \beta|\psi_j|^2\psi_j\,, \tag{5.1}$$

where $V_j = \lambda \cos(2\pi\alpha j + \varphi)$. From now on we choose $\alpha = (\sqrt{5} - 1)/2$ and $\lambda > 2$, since we focus on the interplay between localization and nonlinearity.

The normal modes associated to Eq. (5.1) are defined by neglecting the nonlinear term and solving the following eigenvalue problem

$$- A_{\nu,j+1} - A_{\nu,j-1} + \lambda\cos(2\pi\alpha j + \varphi)A_{\nu,j} = E_\nu A_{\nu,j}\,. \tag{5.2}$$

where the index ν labels the different normal modes $A_{\nu,j}$ and the corresponding eigenvalues E_ν. Equation (5.2) is the Aubry-André model [85] that we introduced in sections 3.1 and 3.2. We have already discussed extensively the localization properties of this model. Here we just remind that in the localized regime ($\lambda > 2$) all the eigenstates are exponentially localized in the form $A_{\nu,j} \sim e^{-|j-j_\nu|/L_{loc}}$, where j_ν is the localization center and $L_{loc} = 1/\ln(\lambda/2)$ is the localization length.

In order to quantify the spatial extent of a given eigenstate, we can conveniently define a localization volume $V_\nu = 1 + \sqrt{12m_2^{(\nu)}}$, where $m_2^{(\nu)} = \sum_j (X_\nu - j)^2|A_{\nu,j}|^2$ is the second moment of $|A_{\nu,j}|^2$ and $X_\nu = \sum_j j|A_{\nu,j}|^2$ is its center of norm [138]. The localization volume V_ν is an important quantity since we will use it as an estimate of
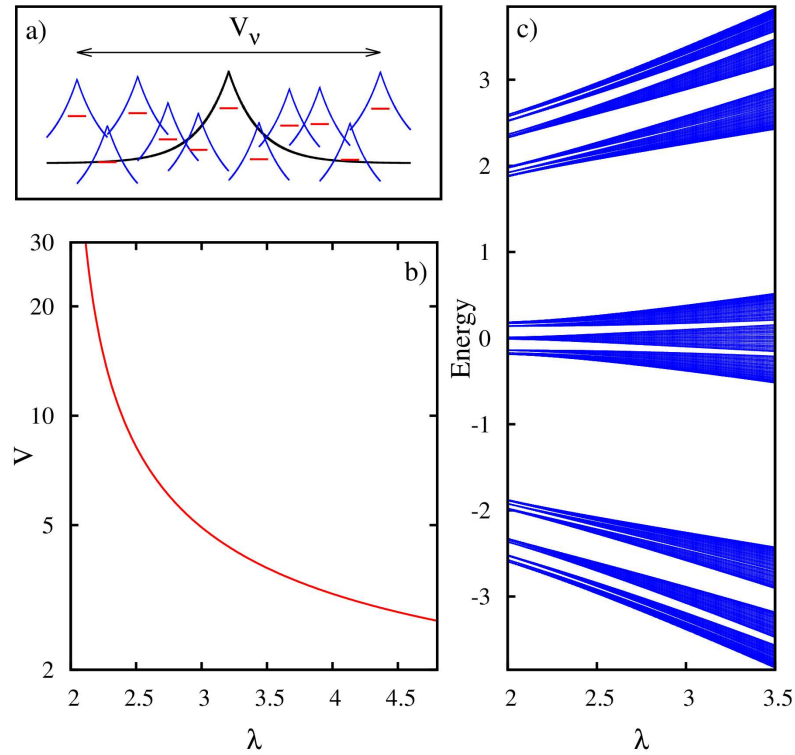
Figure 5.1: *a) Pictorial interpretation of localization volume. A given eigenstate ν (black line in the center of the box) is assumed to interact only with those eigenstates (blue lines) that lie in a region of size V_ν around his mean position. The red lines represent the corresponding on-site energies. b) Average localization volume of eigenstates V as a function of the potential strength λ. c) Eigenenergies E_ν of the linear system obtained from numerical diagonalization of Eq. (5.2), as a function of λ.*

the number of modes which interact with a given mode ν. Its meaning is schematically shown in Fig. 5.1a. The modes that interact with a given reference mode ν are those whose center of norm lies in an area V_ν around it. The quantity that will be relevant for our analysis is an average value of the localization volume at a given value of the disorder strength λ that we indicate with V. The average is performed over the different eigenstates of the spectrum and over different realizations of the quasiperiodic potential. Different realizations of the potential correspond in our case to different values of the phase shift φ. The average localization volume V can be found numerically by direct diagonalizing of the linear system. A plot of this quantity as a function of the potential strength λ is shown in Fig. 5.1b.

We can conveniently use the normal modes of the linear Aubry-André model as a decomposition basis of the wave function ψ_j, $\psi_j = \sum_\nu \phi_\nu A_{\nu,j}$. In this way,

Eq. (4.8) can be rewritten for the evolution of the normal mode amplitudes ϕ_ν:

$$i\frac{\partial \phi_\nu}{\partial t} = E_\nu \phi_\nu + \beta \sum_{\nu_1,\nu_2,\nu_3} I_{\nu,\nu_1,\nu_2,\nu_3} \phi_{\nu_1}^* \phi_{\nu_2} \phi_{\nu_3} \tag{5.3}$$

where $I_{\nu,\nu_1,\nu_2,\nu_3}$ is an overlap integral involving four normal modes:

$$I_{\nu,\nu_1,\nu_2,\nu_3} = \sum_j A_{\nu,j} A_{\nu_1,j} A_{\nu_2,j} A_{\nu_3,j}. \tag{5.4}$$

In the previous chapter we characterized the spreading of wavepackets mainly by considering the time evolution of the particle density $n_j = |\psi_j|^2$, which is described by Eq. (5.1). We basically follow the same approach also in this chapter. However, it is worth stressing that the evolution of wavepackets can be equivalently described in the space of normal modes. This can be done by assigning a position to each normal mode through its center of norm X_ν, and following the evolution of the normal modes amplitudes ϕ_ν given by Eq. (5.3); we can therefore introduce a density also in normal mode space $n_\nu = |\phi_\nu|^2$.

By performing a numerical study of the time evolution of n_ν and n_j, one can show that, after a short transient time and after averaging over many realizations, the two densities are very similar, leading to a time evolution in the two spaces that is almost identical. In the rest of our analysis, we will mainly consider the evolution of the density of particles n_j, but we will also use the normal mode space for some theoretical considerations.

5.2 Relevant energy scales

Interesting information on the spreading of initially localized wavepackets can be obtained from a comparison of two energy scales of the noninteracting spectrum associated to Eq. (5.1) and of an energy scale associated to the nonlinear term. In this section we will introduce these three energy scales (d, Δ, δ) and explain their meanings.

The spectrum for $\lambda > 2$ is purely dense-point, characterized by the presence of an infinite number of gaps and bands. A plot of the Aubry-André model's spectrum as a function of λ is shown in Fig. 5.1c. In this figure, one clearly sees the presence of two major gaps dividing the spectrum in three parts, each of them divided in turn in three smaller parts, and so on. An intuitive understanding of this band structure can be given, following an heuristic argument. The wavelength associated to the potential V_j is $1/|\tilde{\alpha}| = (\sqrt{5} + 3)/2 \approx 2.62$ (see section 3.1 for more details). An effective wavelength equal to an integer number q would correspond to a separation in exactly q bands. Our value of $1/|\tilde{\alpha}|$ lies between two and three, so that the band structure has neither two nor three bands, but three main bands with an internal structure of sub-bands. In the following we will call these portions of spectrum separated by the largest gaps "mini-bands". For our purposes, it is enough to consider

a division of the spectrum in $M = 3$ or at most in $M = 9$ mini-bands. Smaller mini-bands have vanishingly small effects on the time evolution of wavepackets.

Let us introduce two energy scales associated with the linear system [126, 138]. The first one, Δ, is the full width of the spectrum, defined as the difference between the largest and the smallest eigenvalues: $\Delta = \max\{E_\nu\} - \min\{E_\nu\}$. The second one, d, is the mean spacing of eigenvalues within a single mini-band and within the range of a localization volume. Let us explain how we calculate this quantity. We consider a given mini-band and all the eigenstates that lie in it. For each eigenstate ν, we calculate its localization volume V_ν and then we form the subset of the other eigenstates, $\{\mu\}$, belonging to the same mini-band and interacting with it, namely, those fulfilling the condition $|X_\nu - X_\mu| < V_\nu/2$. The average number of states in the subset can be estimated as V/M. Then we calculate the energy spacings within this subset. This procedure is repeated for each eigenstate in the band and then averaging over all the eigenstates and different disorder realizations gives the mean spacing d.

The number of mini-bands M to be used in the calculations of d depends on λ. For a given λ we choose M in such a way that the localization volume V satisfies the condition $V/M > 2$. This implies that, on average, there are at least two eigenstates within the subset $\{\mu\}$ that we can use to calculate the average energy spacings. We always consider $\lambda > 2.1$; therefore it is enough to divide the spectrum at most in nine mini-bands. As λ is increased the average localization volume of the eigenstates V decreases – therefore at some point we have to consider the spectral separation into smaller mini-bands. In practice we consider $M = 9$ mini-bands for $2.1 \lesssim \lambda \lesssim 2.2$, $M = 3$ mini-bands for $2.2 \lesssim \lambda \lesssim 2.75$ and just one band (i.e., the full spectrum) for $\lambda \gtrsim 2.75$. A plot of the energy scales Δ and d as a function of λ is shown in Fig. 5.2. These two quantities have been calculated numerically diagonalizing Eq. (5.2). The dashed vertical lines represent the values of λ where the number of mini-bands changes in the calculation of d.

We note that in the present setting, where we have set $\hbar = 1$ and we are dealing with spreading of nonlinear wavepackets, all the energies can also be interpreted as frequencies. For instance the eigenenergies of the system E_ν can also be interpreted as the oscillation frequencies of the normal modes. In the following we will therefore use the terms energy and frequency interchangeably.

Let us now introduce the energy scale associated to the nonlinearity, δ, we will call it nonlinear frequency shift following the notation introduced in [126]. In order to explain the concept of nonlinear frequency shift let us first consider a single site problem with an on-site potential V. The time evolution of this system is described by the following equation of motion $i\dot\psi = V\psi + \beta|\psi|^2\psi$ and can be viewed as the evolution of an oscillator that experiences a nonlinear frequency shift $\delta = \beta|\psi|^2$ away from its linear frequency V. The evolution described by Eq. (5.1), which involves many lattice sites, can be viewed as a set of coupled oscillators and it is more convenient to approach the problem in normal mode space. From Eq. (5.3) one can see that the frequency shift can be estimated as $\delta \sim \beta n$, where n is a characteristic average density $n = \bar n_\nu \approx \bar n_j$ which is approximately equal in real and

mode space, as we have discussed in the previous section.

5.3   Expected spreading regimes

Equation (5.3) indicates that the presence of nonlinearity in the DNLS model introduces a coupling between eigenstates of the underlying linear spectrum. We already discussed in the previous chapter that this leads to a subdiffusive spreading of wavepackets, i.e. its width grows asymptotically as $w \sim t^\gamma$ with $\gamma < 0.5$. This behaviour has been observed both numerically and experimentally. However, a systematic investigation of the behaviour of the exponent γ in different regimes of strong and weak chaos, and self-trapping, have not been done so far. In this section, we approach this issue by first comparing the nonlinear frequency shift $\delta = \beta n$ with the energy scales Δ and d, in such a way as to introduce the different spreading regimes expected to be observed in the subsequent numerical simulations.

Let us consider an initial wavepacket with density n and localization volume L larger than the average localization volume of the eigenstates of the linear spectrum, $L \geq V$. If $\delta > \Delta$, nonlinearity is so strong that all the participating normal modes within the wavepacket are shifted out of resonance with respect to the non-excited neighbourhood; therefore spreading is largely suppressed and a significant part of the wavepacket remains self-trapped. In section 4.2.1 we introduced this phenomenon following an energy conservation argument while here we presented it from a different perspective, as an exited mode which is off-resonant with the other neighbouring modes. We note that both analysis lead to the same conclusion that the relevant energy scale for the determination of the self-trapping transition is the width of the linear spectrum Δ.

If instead $\delta < \Delta$, we are no longer in the self-trapping regime and two sub-cases can be distinguished: on one hand, when $\delta > d$, strong chaos is realized, the mode frequencies are strongly shifted and all the modes in the packet are resonantly interacting with each other, thus producing an efficient spreading. On the other hand, when $\delta < d$, the mode frequencies in the wavepacket are only weakly shifted and weak chaos is obtained: only a fraction of modes interact resonantly, the localization is still destroyed, but spreading is slower.

If $L < V$ the estimate of the self-trapping transition is done as before, that is by comparing $\delta = \beta n$ with the spectrum width Δ. If self-trapping is avoided, however, the wavepacket initially spreads also in absence of nonlinearity, eventually filling the localization volume V. Consequently the initial density n is reduced to $\tilde{n} \approx nL/V$, due to linear time evolution, the relevant nonlinear frequency shift must now be calculated by using this reduced density $\tilde{n}$. Apart from this detail, which originates from the initial dynamics at short times, the asymptotic spreading regimes are the same as before. Note that the strong chaos regime can only exist as a transient regime: as the wavepacket spreads, its norm density $n(t)$ decreases, and eventually will reach a situation where $\beta n(t) < d$. At this point, a crossover from strong to
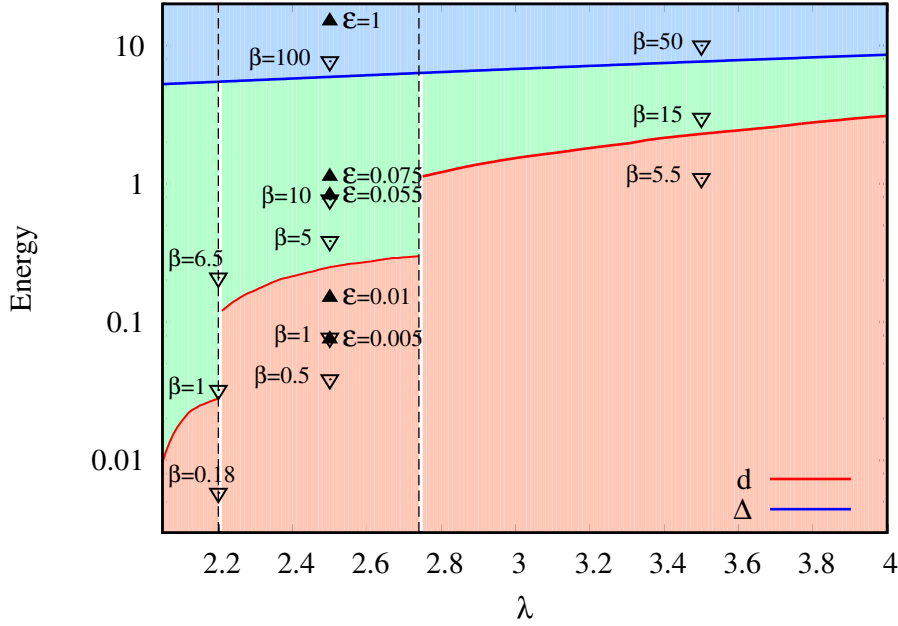
Figure 5.2: *Energy scales Δ (top blue line) and d (bottom red line) plotted as a function of the potential strength λ. The empty (downward) and full (upward) triangles correspond to the values of δ that we have used for the simulations with the DNLS model and with the KG model respectively. Comparing the nonlinear frequency shift δ with the energy scales Δ and d one can predict the different spreading regimes of weak chaos (δ < d), strong chaos (d < δ < Δ) and self-trapping (δ > Δ). The separation between the three regimes should not be interpreted as a sharp boundary, but as a smooth crossover.*

weak chaos is expected to occur during the time evolution [131]. To summarize

$$\beta n > \Delta \quad \text{self-trapping} \tag{5.5}$$

$$d < \beta\tilde{n} < \Delta \quad \text{strong chaos} \tag{5.6}$$

$$\beta\tilde{n} < d \quad \text{weak chaos} \tag{5.7}$$

where $\tilde{n} = n$ if $L \geq V$ and $\tilde{n} = nL/V$ if $L < V$.

Let us finally stress that the "transition lines" that we have introduced by comparing the nonlinear frequency shift with the typical energy scales of the linear spectrum do not define sharp phase transitions between different spreading regimes. Instead, we may expect to see a relatively smooth crossover, such that the regimes of self-trapping, strong chaos and weak chaos should be clearly identified only far from the transition lines.

5.3.1   Spreading laws

In the previous section we discussed how to predict the different spreading regimes starting from energy scale arguments, but this method does not provide information on the spreading laws associated to the different regimes. Here we discuss this issue by making a link with the concepts of strong and weak chaos.

We follow the theory which has been first introduced by Flach, Skokos, Krimer and Komineas in Refs. [126, 129] and then developed further in Ref. [130]. More recently Michaely and Fishman [139] discussed more in detail some assumptions on which the theory is based. So far, the theory has been applied to a purely disordered system where the potential V_j is a random variable uniformly distributed in the interval $[-W/2, W/2]$. However, it can be applied also to the quasiperiodic case described by Eq. (5.1). In fact the theory can be used when (i) the equation associated to the linear system yields Anderson localization, (ii) the localization length L_{loc} is upper bounded, (iii) the nonlinearity is compact in real space and does not induce long range interactions between normal modes of the linear system.

The starting point is the equation of motion in normal mode space (5.3). Let us rewrite this equation by removing the trivial time evolution which is given by the linear term. This can be done by substituting

$$\phi_\nu(t) = \chi_\nu(t)e^{-iE_\nu t} \tag{5.8}$$

into Eq. (5.3). One obtains

$$i\frac{\partial \chi_\nu}{\partial t} = \beta \sum_{\nu_1,\nu_2,\nu_3} I_{\nu,\nu_1,\nu_2,\nu_3}\, \chi_{\nu_1}^* \chi_{\nu_2}\chi_{\nu_3}\, e^{i(E_\nu+E_{\nu_1}-E_{\nu_2}-E_{\nu_3})}. \tag{5.9}$$

Let us define the right hand side of this equation as a generic function $F(t)$. The theory now considers the spreading from the region occupied by the wavepacket, where the modes ν_1, ν_2, ν_3 lie, to the exterior non-exited region, where the mode ν is localized. Moreover it is assumed that all the modes inside the packet are exited to the same density n [126, 129], in particular

$$|\chi_{\nu_1}|^2 \approx |\chi_{\nu_2}|^2 \approx |\chi_{\nu_3}|^2 \approx n \qquad\qquad |\chi_\nu|^2 \ll n. \tag{5.10}$$

The key assumption of the theory, which is sometimes referred to as the "random phase ansatz" [140], is that $F(t)$ behaves as a random noise. This ansatz combined with (5.10) suggests that the right hand side of Eq. (5.9) can be written in the following form [130, 139]

$$F(t) \approx C\beta n^{3/2}\mathcal{P}(\beta n)f(t) \tag{5.11}$$

where $\mathcal{P}(\beta n)$ is the number of resonant modes in the packet, i.e. those who strongly affects the dynamics of ν, $f(t)$ is a random noise such that $\langle f(t)f(t')\rangle = \delta(t-t')$[1] and C is a constant that does not depend on β and n. For purely random systems the

---

[1]here $\langle\dots\rangle$ indicates an average over the disordered potential.

resonance probability has been estimated to be $\mathcal{P}(\beta n) = (1 - e^{-C_0\beta n})$ [126, 129, 138] while for the quasiperiodic model under considerations we will present a calculation of this quantity in the next section. The validity of the random phase ansatz and of the relation $\langle f(t)f(t')\rangle = \delta(t - t')$ has been recently verified numerically in [139]. Combining Eqs. (5.9) and (5.11) one finds

$$i\frac{\partial}{\partial t}\chi_\nu \approx C\beta n^{3/2}\mathcal{P}(\beta n)f(t), \qquad (5.12)$$

and therefore

$$\chi_\nu \approx -iC\beta n^{3/2}\mathcal{P}(\beta n)\int_0^t f(t')\,dt'. \qquad (5.13)$$

Taking the modulus square and averaging over the disorder yields

$$\langle|\chi_\nu|^2\rangle \approx C\beta^2 n^3[\mathcal{P}(\beta n)]^2 t. \qquad (5.14)$$

From this equation it is possible to estimate a momentary diffusion rate, D, which is proportional to the inverse of the equilibration time T, i.e. the time needed to excite the exterior mode ν to the packet level n

$$T = \frac{1}{C\beta^2 n^2[\mathcal{P}(\beta n)]^2} \quad \text{and} \quad D \sim \frac{1}{T} \qquad (5.15)$$

The equilibrium time T varies slowly with t, this can be verified by checking that $\frac{\partial T}{\partial t} \to 0$ for $t \to \infty$. In other words, there is a separation of timescales: on the scale given by T the system seems to equilibrate by a diffusion process and the packet populates the region occupied by ν; on a longer timescale there is an even longer equilibration process associated to a slower diffusion. We will comment more on this point at the end of the section. Thus, for times much larger than T the spreading is governed by a diffusion equation and in particular

$$w(t) \sim \sqrt{D}t^{1/2}. \qquad (5.16)$$

Since the width of the wavepacket is of the order of the inverse of the density $w \sim 1/n$ we can rewrite Eq. (5.16) as follows

$$\frac{1}{n} \sim \beta^{1/2}[\mathcal{P}(\beta n)]^{1/2}t^{1/4}. \qquad (5.17)$$

What we have discussed so far is general and applies both to the random and the quasiperiodic case. For the remaining part of this section we continue the discussion focusing on random systems and we will use $\mathcal{P}(\beta n) = (1 - e^{-C_0\beta n})$. In the next section we will calculate $\mathcal{P}(\beta n)$ and discuss the spreading laws for the quasiperiodic case.

For large values of the nonlinear frequency shift, $\delta = \beta n$, it is easy to verify that $\mathcal{P}(\beta n) = (1 - e^{-C_0\beta n}) \to 1$. In this situation strong chaos is realized and all the modes are resonantly interacting. From Eq. (5.17) one obtains that the corresponding spreading law is

$$w(t) \sim t^{1/4}. \qquad (5.18)$$
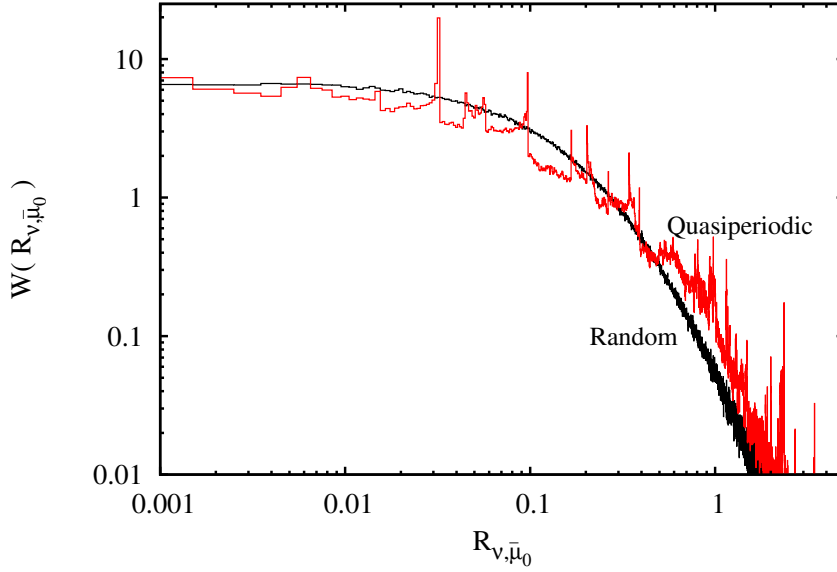
Figure 5.3: *Comparison between the probability density function $\mathcal{W}(R_{\nu,\vec{\nu_0}})$ of the quasiperiodic DNLS model and of the random DNLS model. For the quasiperiodic case, $\lambda = 2.5$, while for the random case, we choose a disorder strength that gives a similar localization length.*

Conversely, for small values of the nonlinear frequency shift $\mathcal{P}(\beta n) \to \beta n$, the packet is in the weak chaos regime and only a fraction of the modes is resonant. As a consequence a slower spreading is obtained

$$w(t) \sim t^{1/6}. \tag{5.19}$$

Eqs. (5.18) and (5.19) defines the expected spreading laws for the weak chaos and strong chaos regimes for the random case. Numerical simulations are in very good agreement with these theoretical expectations [126, 129, 131, 132].

Starting from the spreading laws (5.18) and (5.19) one can derive the asymptotic time evolution also for $n(t)$ and $T(t)$ [139]. One can therefore observe that $\frac{\partial T}{\partial t}$ and $\frac{\partial n}{\partial t}$ tends both to zero for large times. This justifies the separation of timescales that we mentioned previously. Moreover $\frac{\partial n}{\partial t} \ll \frac{\partial T}{\partial t}$ for $t \to \infty$, therefore the fact that we considered a constant density n in the derivation of the equilibration time T and of the diffusion rate D is justified in the long time limit [139].

5.3.2   Resonance probability

Let us estimate the number of resonant modes in the packet $\mathcal{P}(\beta n)$ for the quasiperiodic model under consideration (5.1). As we have seen in the previous section this is a key quantity for the determination of the spreading behaviour. According to

Eq. (5.9), due to nonlinearity, the evolution of a given normal mode is affected by any three (triplet) modes. The coupling is the largest if the triplet modes have large amplitudes and if the overlap integrals are large, i.e., if the triplet modes are close enough in space to the given normal mode. Some of these triplet modes may affect the dynamics of the chosen mode ν strongly, some weakly. To distinguish these triplet groups, we apply perturbation theory to Eq. (5.9) [126, 141]. We use a perturbation expansion of the coefficients χ_ν in powers of β

$$\chi_\nu = \chi_\nu^{(0)} + \chi_\nu^{(1)} + \chi_\nu^{(2)} + ... = c_\nu^{(0)} + \beta c_\nu^{(1)} + \beta^2 c_\nu^{(2)} + ... \qquad (5.20)$$

At first order and assuming (5.10) one finds

$$\chi_\nu^{(1)} = -\beta n^{3/2} \sum_{\nu_1,\nu_2,\nu_3} \frac{I_{\nu,\nu_1,\nu_2,\nu_3}}{E_\nu + E_{\nu_1} - E_{\nu_2} - E_{\nu_3}} e^{i(E_\nu + E_{\nu_1} - E_{\nu_2} - E_{\nu_3})t} \qquad (5.21)$$

It follows that the amplitude of a normal mode ν is changed by a given triplet of other wavepacket modes $\vec{\nu} = \{\nu_1, \nu_2, \nu_3\}$ (we consider just the contribution of a single triplet to the sum of Eq. (5.21)) as

$$|\chi_\nu^{(1)}| = \beta \frac{n^{3/2}}{R_{\nu,\vec{\nu}}} \qquad (5.22)$$

where

$$R_{\nu,\vec{\nu}} = \left| \frac{E_\nu + E_{\nu_1} - E_{\nu_2} - E_{\nu_3}}{I_{\nu,\nu_1,\nu_2,\nu_3}} \right|. \qquad (5.23)$$

The perturbation approach breaks down and resonances set in when $\sqrt{n} < |\chi_\nu^{(1)}|$ [126, 138]. Substituting

$$R_{\nu,\vec{\nu}} < \beta n. \qquad (5.24)$$

This expression tells us that the resonance condition, for a given normal mode ν, is fulfilled if there is at least one triplet of modes $\vec{\nu}$ that satisfies inequality (5.24).

The probability for the onset of a resonance can therefore be calculated with the following statistical numerical analysis [126, 138]. For a given normal mode ν, we define $R_{\nu,\vec{\nu}_0} = \min_{\vec{\nu}} \{R_{\nu,\vec{\nu}}\}$. Collecting $R_{\nu,\vec{\nu}_0}$ for many modes and many values of the phase φ, we find the probability density distribution $\mathcal{W}(R_{\nu,\vec{\nu}_0})$. From this quantity we can calculate the probability $\mathcal{P}$ for a mode, which is exited to a norm density n, to be resonant with at least one triplet of other modes at a given value of the interaction parameter β. This is obtained by integrating $\mathcal{W}(R_{\nu,\vec{\nu}_0})$ from zero to βn

$$\mathcal{P} = \int_0^{\beta n} \mathcal{W}(R) \, dR. \qquad (5.25)$$

An example of probability density $\mathcal{W}(R_{\nu,\vec{\nu}_0})$ for $\lambda = 2.5$ is shown in Fig. 5.3 (red line). For comparison we also show the same quantity for the random DNLS model (black line), as discussed in [126, 138], which is approximately given by $\mathcal{W}(R) \approx C_0 e^{-C_0 R}$. Except for fine structures, like small sharp peaks appearing

in the quasiperiodic case, the overall behaviour is qualitatively very similar in the two cases. In particular, in both cases, the probability density $\mathcal{W}(R)$ tends to a finite constant value C_0 when $R \to 0$ and then tends rapidly to zero for large values of R.

As a consequence we expect the same spreading behaviour in the quasiperiodic and in the random case. More precisely, for small values of the nonlinear frequency shift $\delta = \beta n$, a non-zero fraction of modes in the packet is resonant. The probability to be resonant is given by $\mathcal{P}(\beta n) \sim \beta n$, thus we are in the weak chaos regime. For large values of βn, instead all the modes interact resonantly and $\mathcal{P} = 1$; we are then in the strong chaos regime. Following the reasoning presented in the previous section, this implies that also in the quasiperiodic case, as in disordered systems, we may expect to find $w(t) \sim t^{1/6}$ in the weak chaos regime and $w(t) \sim t^{1/4}$ in the strong chaos regime.

5.4 Numerical observations

We perform extensive numerical simulations solving Eq. (4.8) for different sets of parameters $\{\lambda, \beta\}$. For each choice of parameters we average over N different realizations of the quasiperiodic potential obtained by randomly changing the phase shift φ. As initial conditions, we use compact wavepackets that lie in the center of our computational box, taking care that during the time evolution the wavepacket never reaches the box boundaries. The number of realizations considered varies between 100 and 500 and the number of lattice sites between 200 and 2000. To solve the equations of motion, we use symplectic integration schemes of the SABA family [142, 129] that allow us to reach large integration times with good accuracy[2].

In order to quantify the type of subdiffusive behaviour, we calculate the exponent γ by considering the logarithm of the width $\log_{10} w$ for different realizations of the potential. We compute the average value $\langle \log_{10} w \rangle$ and its statistical error, given by the standard deviation divided by the square root of the number of realizations N. Then the value of γ at a given time t is calculated by applying a linear fitting procedure to the curve $\langle \log_{10} w \rangle$ within a fixed time interval around $\log_{10} t$. By repeating this procedure at different t, we extract the behaviour of γ as a function of time and its relative statistical error. In order to detect the self-trapping transition (as we have done in section 4.2.1) we also calculate the average participation number, $\langle \log_{10} P \rangle$. Finally we also quantify the sparsity of the wavepacket by calculating the compactness index [129]

$$\xi = \frac{P^2}{w^2} = \frac{P^2}{m_2}. \tag{5.26}$$

This definition follows from the fact that the width w (and also the second moment m_2) is sensitive to the spreading of the tails of the distribution while the participation

---

[2]The numerical accuracy of our calculation is controlled by checking the conservation of the energy $\mathcal{H}$ and the norm $\mathcal{N}$ of the expanding wavepacket (check Eqs. (4.11) and (4.10)). The error is always kept smaller than $10^{-2.5}$. For the integration we used time steps between 0.1 and 0.05.

number P is a measure of the inhomogeneity of the distribution, being insensitive to any spatial correlation. For this reason a combination of these two quantities gives a measure of the sparsity of a distribution. In particular smaller values of ξ correspond to more sparse wavepackets.

5.4.1 Results for square wavepackets

Let us first show our results for initial wavepackets that has a square shaped distribution which populates L lattice sites with equal density $n_j = |\psi_j|^2 = 1/L$. In this particular case the calculation of the nonlinear frequency shift is straightforward since the average density is simply given by $n = 1/L$ and $\delta = \beta/L$. In Fig. 5.4 we present a representative set of simulations for $\lambda = 2.5$. We choose $L = 13$, which gives an initial localization volume larger than V. The different panels show the time evolution of the width $\langle \log_{10} w \rangle$, the spreading exponent γ, the participation ratio $\langle \log_{10} P \rangle$, and the compactness index $\langle \xi \rangle$. The width of the curves for $\langle \log_{10} w \rangle$, $\langle \log_{10} P \rangle$ and γ corresponds to the statistical error. The values of the nonlinear frequency shift δ induced by the initial wavepackets used in these simulations are shown in Fig. 5.2 (empty downward triangles) in order to compare them to the relevant energy scales Δ and d.

In all simulations we observe that nonlinearity causes the wavepacket to spread. The spreading starts earlier when β is larger. We find that the spreading is always subdiffusive ($\gamma < 0.5$), confirming the result of previous sections 4.2.2 and 4.3.2. Subdiffusion is seen both in the width w and in the participation number P, except for the largest value of β (yellow curves in Fig. 5.4). In the latter case, P saturates to a constant value after a transient time, a clear signature of self-trapping. This observation of self-trapping only for $\beta = 100$ is consistent with the energy scale arguments schematically represented in Fig. 5.2. In the absence of self-trapping, the compactness index ξ saturates to a constant value, indicating that the wavepacket spreads but does not become more sparse. Conversely, in the presence of self-trapping the central part of the wavepacket remains spatially trapped while its tails keep expanding, thus resulting in a wavepacket that becomes more sparse during the evolution, nicely quantified by the compactness index which decreases to zero. We notice that the portion of packet that is expanding is characterized by a value of γ larger than $1/4$. After an initial increase, γ reaches a maximum and then decreases to smaller values. In this regime, the evolution is rather complex and the theory presented in section 5.3.1 does not apply since condition (5.10) is not satisfied. A similar behaviour was previously obtained also in random systems [131, 132]. The transient large values of γ may be due to a nontrivial interacting mechanism that takes place between the expanding part and the self-trapped portion, resulting in faster spreading, an effect that we call "overshooting".

For the lowest values of β the energy scale arguments suggest the occurrence of weak chaos. Indeed for $\beta = 0.5$ and 1 the exponent saturates asymptotically around the theoretical value $\gamma = 1/6$ (red and green curves in Fig. 5.4), as expected. It is worth mentioning that this asymptotic exponent is the same as in random sys-
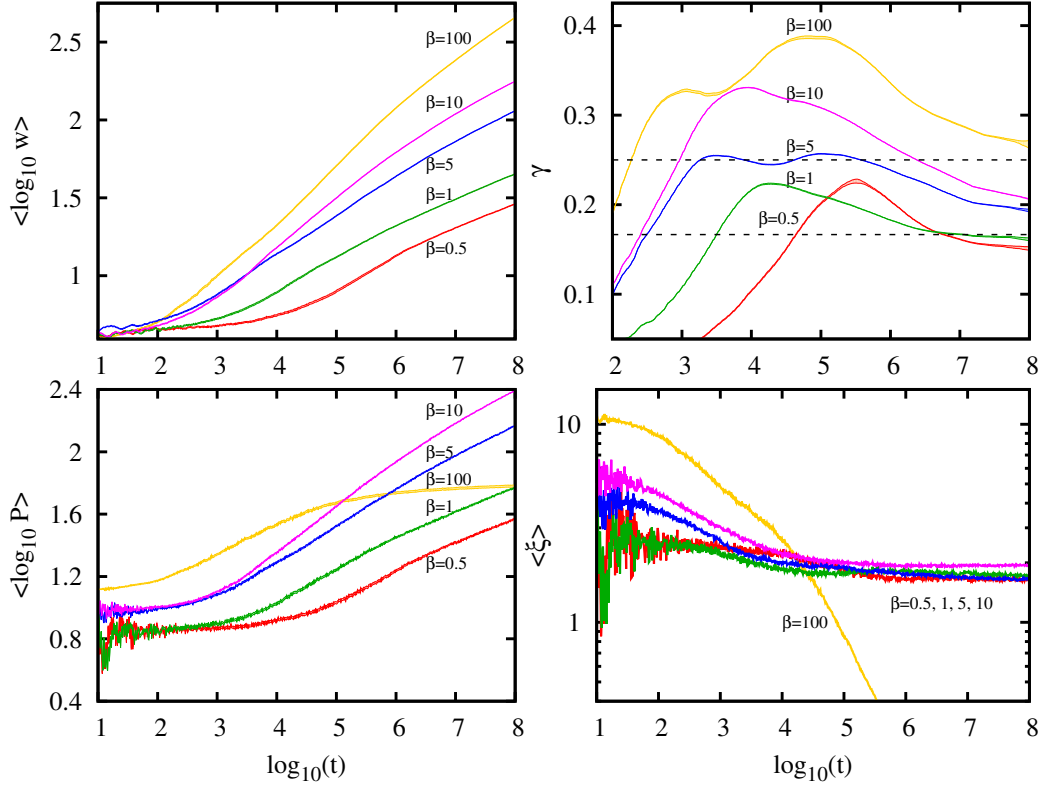
Figure 5.4: *Numerical results obtained by integrating the DNLS equations of motion
(4.8). The time evolution of $\langle \log_{10} w \rangle$ (left panel, top), γ (right panel, top), $\langle \log_{10} P \rangle$
(left panel, bottom), and $\langle \xi \rangle$ (right panel, bottom) is shown versus $\log_{10} t$ for different
values of the nonlinear parameter $\beta = 0.5, 1, 5, 10, 100$. The initial wavepacket in
all simulations is a square distribution with $L = 13$ and the potential strength is
$\lambda = 2.5$. In the top right panel the two dashed lines correspond to theoretically
predicted power laws $\gamma = 1/6$ and $\gamma = 1/4$. The width of the lines for the quantities
$\langle \log_{10} w \rangle$, $\langle \log_{10} P \rangle$ and γ represents the statistical error, which depends on time and
on the number of realizations. In most cases the statistical error is smaller than the
resolution of the figure.*

tems [130, 131]; meaning that the mechanism leading to destruction of exponential
localization is rather universal.

In difference to the random case, here during the time evolution, the value of γ
temporarily increases above $1/6$, eventually reaching its asymptote only at longer
times. This is an overshooting similar to the one that we have discussed above for
the self-trapping regime, but occurring also for weaker nonlinearities. This effect is
unique to the quasiperiodic system and is likely due to the presence of an infinite
number of mini-bands and gaps in the linear spectrum of the Hamiltonian, which
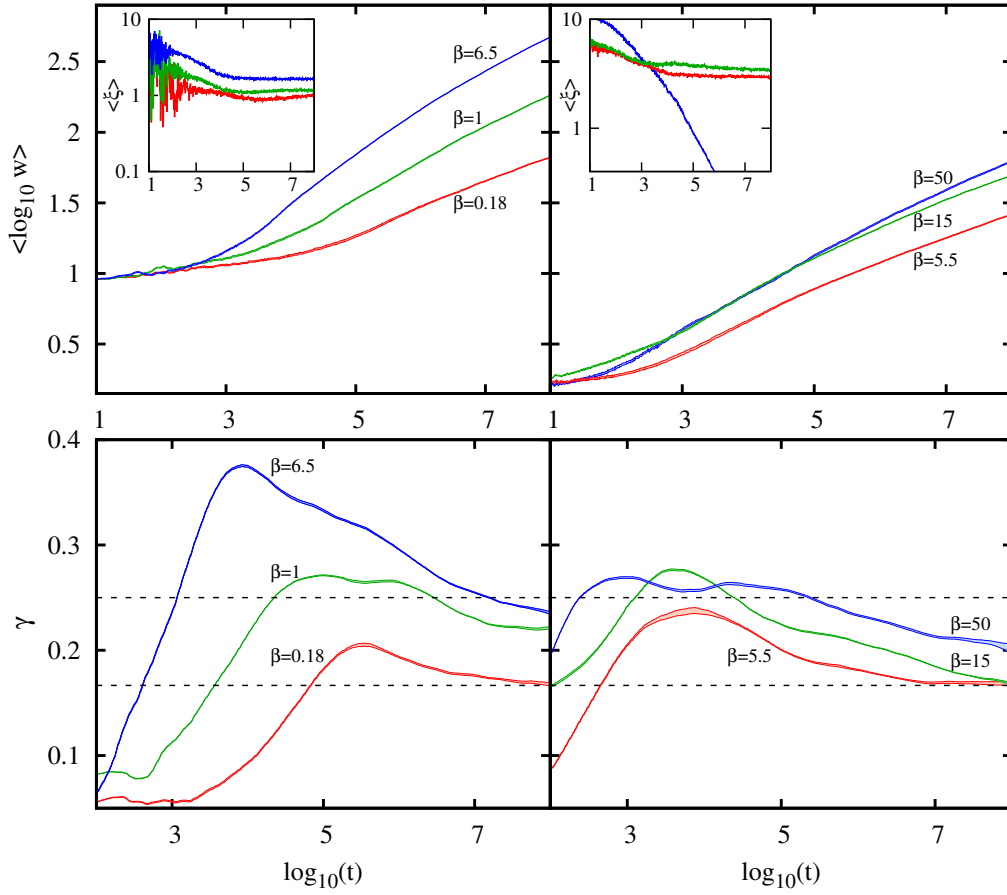
Figure 5.5: *Average logarithm of the width of the expanding wavepacket, $\langle \log_{10} w \rangle$ and spreading exponent, γ for $\lambda = 2.2$ (left plots) and $\lambda = 3.5$ (right plots). For $\lambda = 2.2$, the initial wavepacket has width $L = 31$ and we consider $\beta = 0.18$ (lower red curves), 1 (mid green curves) and 6.5 (upper blue curves). For $\lambda = 3.5$, the initial wavepacket has width $L = 5$ and we consider $\beta = 5.5$ (lower red curves), 15 (mid green curves), and 50 (upper blue curves). The width of the lines represents the statistical error as in Fig. 5.4. Insets: average compactness index of the expanding wavepacket $\langle \xi \rangle$ for the same sets of simulations.*

causes a temporary self-trapping of portions of the expanding wavepacket in one or more energy gaps between mini-bands. This partial self-trapping is different from the self-trapping that occurs when $\delta > \Delta$, where all the packet modes are simultaneously shifted out of resonance. For this reason partial self-trapping is not detectable as a saturation of the participation number P and can only be seen indirectly as an overshooting in the exponent γ.

The two simulations for $\beta = 5$ and 10 lie in a range of energy were we expect to see strong chaos (blue and magenta curves in Fig. 5.4). As already said in the

previous section, the strong chaos regime is transient: one should find a value of γ around $1/4$ for a few decades of time, eventually decreasing towards the asymptotic value $1/6$. The two corresponding curves in Fig. 5.4 indeed exhibit a behaviour which qualitatively agrees with this expectation. The value of γ first rises up to $1/4$, oscillates around this value and then starts to decrease as predicted. However, especially for large β, we also observe values of γ larger than $1/4$. As in the weak chaos regime, this overshooting again is evidence of partial self-trapping. Its mechanism is also transient and occurs in the same time intervals where strong chaos is expected. For this reason, while weak chaos is clearly observed in our simulations, strong chaos and partial self-trapping tend to overlap, thus producing a more complex evolution of the wavepacket in quasiperiodic systems than in random systems.

In Fig. 5.5 we show the results of simulations for $\lambda = 2.2$ and $\lambda = 3.5$; the corresponding values of nonlinear frequency shift are reported as triangles in Fig. 5.2. The values of L are $L = 31$ for $\lambda = 2.2$ and $L = 5$ for $\lambda = 3.5$, both larger than V. For $\{\lambda, \beta\} = \{2.2, 0.18\}$ and $\{\lambda, \beta\} = \{3.5, 5.5\}$ energy scale arguments predict weak chaos. We indeed find a spreading exponent which approaches asymptotically the value $1/6$. For $\{\lambda, \beta\} = \{2.2, 1\}$, $\{\lambda, \beta\} = \{2.2, 6.5\}$ and $\{\lambda, \beta\} = \{3.5, 15\}$ the predicted behaviour is either strong chaos or a regime in between strong and weak chaos. What we observe numerically is a growth of the spreading exponent γ up to $1/4$ and even to larger values, followed by a decrease towards $1/6$. In most cases, our simulations show a significant overshooting due to partial self-trapping. It is worth mentioning that this effect is larger for weaker disorder strength λ, consistent with the fact the linear spectrum exhibits larger mini-gaps in this regime (see Fig. 5.1). Finally for $\{\lambda, \beta\} = \{3.5, 50\}$, we observe self-trapping, as expected.

In conclusion, from the analysis of the results of the DNLS model for different values of λ we find that the energy scale arguments and the model discussed in section 5.2 correctly explain the overall trend of the numerical simulations and the separation between different spreading regimes in the parameter space.

5.4.2 Role of the shape of the initial wavepacket

In this section we show that the results discussed so far do not depend on the shape of the initial wavepacket. Besides its theoretical interest, this issue is also relevant from the point of view of experiments, where it is not always possible to design the wavepackets at will.

In the previous section, we have used a square distribution as initial wavepacket. Now, inspired by the experiments with ultracold atoms, we consider initial wavepackets with the shape of a Gaussian distribution (as we have done in section 4.2.2) or a Thomas-Fermi (TF) distribution. In this case of inhomogeneous initial wavepackets the average value of the density is estimated as the inverse participation number at $t = 0$, $n = \sum_j |\psi_j|^4$. Therefore the nonlinear frequency shift is given by $\beta \sum_j |\psi_j|^4$, which is also identical (up to a prefactor) with the mean-field interaction energy.

Let us recall the definition of Gaussian wavepacket (cfr. section 3.3) which is
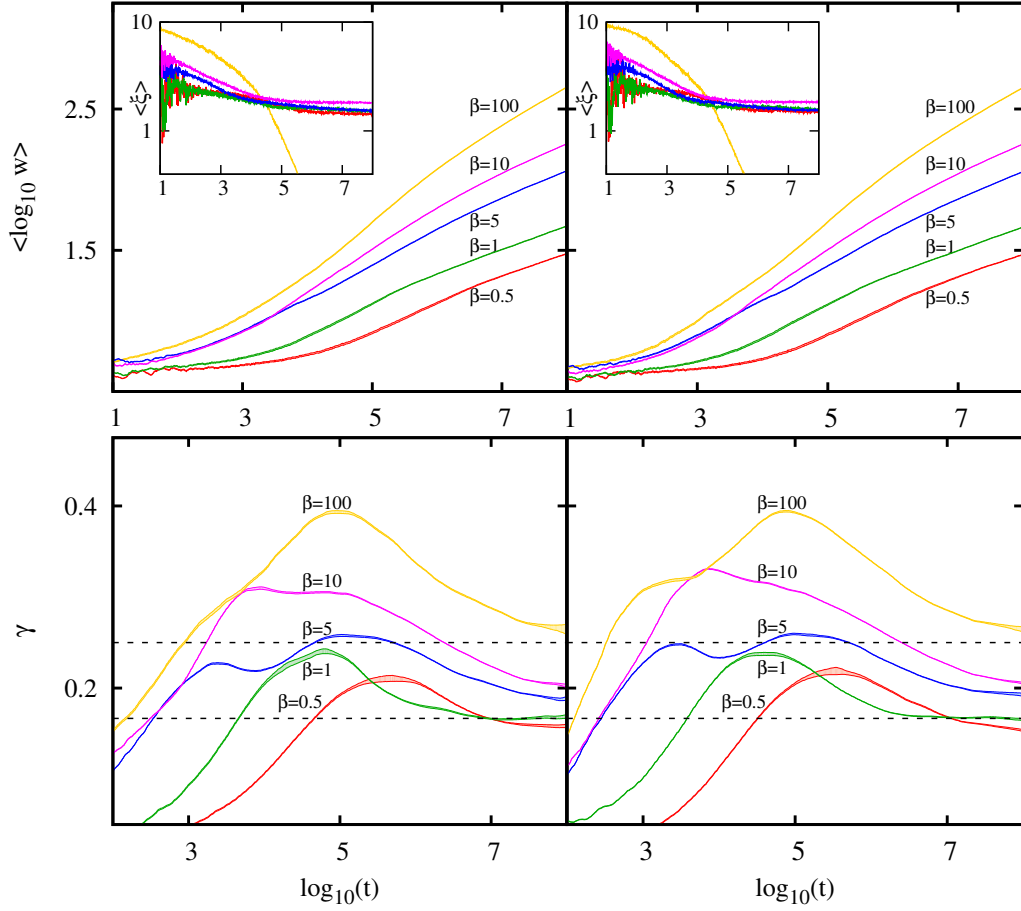
Figure 5.6: *Average logarithm of the width of the expanding wavepacket, $\langle \log_{10} w \rangle$ and spreading exponent, γ as a function of time for different nonlinearities $\beta = 0.5, 1, 5, 10, 100$. The disorder strength is $\lambda = 2.5$ in all simulations. As an initial condition, we have used a Gaussian wavepacket with $\sigma = 5$ (left plots) and a TF distribution with $R = 7.50$ (right plots). The width of the lines represents the statistical error as in Fig. 5.4. Insets: average compactness index of the expanding wavepacket $\langle \xi \rangle$ for the same sets of simulations.*

given by

$$\psi_j(0) = C_1 e^{-\frac{j^2}{2\sigma^2}}, \tag{5.27}$$

where σ is a parameter controlling the width of the packet while C_1 is a constant factor that can be determined by using the normalization condition $\sum_j |\psi_j|^2 = 1$. A Thomas-Fermi wavepacket is instead defined by

$$\psi_j(0) = C_2 \sqrt{1 - \frac{j^2}{R^2}} \tag{5.28}$$

in the region where $|j| < R$ and $\psi_j = 0$ otherwise. The parameter R is the Thomas-Fermi radius characterizing the width of the distribution, while the constant C_2 is a normalization factor. These two distributions are of interest when considering ultracold bosons initially released from an harmonic trap in the Gross-Pitaevskii regime [107].

In Fig. 5.6 we show the time evolution of the width of the expanding wavepacket, $\langle \log_{10} w \rangle$ (top row) and of the spreading exponent, γ (bottom row), using initially a Gaussian (left column) and a TF (right column) wavepacket distribution. In the insets we also show the compactness index $\langle \xi \rangle$, in order to identify the self-trapping regime. We choose the width of the initial distributions (σ and R) so that the nonlinear frequency shift is similar to the one already used for the simulations in Fig. 5.4. In particular we use $\sigma = 5$ and $R = 7.5$, yielding a nonlinear frequency shift $\delta \approx \beta/13$. The values of β used in Fig. 5.6 are the same as those previously considered.

From the comparison between the results of Fig. 5.6 and Fig. 5.4, we can conclude that the shape of the initial wavepacket does not affect the overall behaviour of the time evolution, nor its interpretation in terms of regimes of weak and strong chaos, self-trapping, and overshooting. This suggests the results that we have obtained are rather general and that the nonlinear frequency shift δ is the only key parameter controlling the dynamics of the wavepacket.

5.5   Application to cold atoms

Let us now discuss the relation of the analysis performed in this chapter with the results presented in section 4.3.2 where we measured the spreading exponent γ for times of the order of the duration of typical experiments with ultracold atoms. We can say that the results presented here are consistent with the observations of 4.3.2 where we observed spreading exponents larger than $1/6$ already for weak nonlinearities and even larger than $1/4$ for larger nonlinearities. In fact in our dimensionless units, the experimental expansion is of the order of 10^4 and the width of the atomic cloud increases up to $50 - 100$ lattice sites. Considering Figs. 5.4 and 5.5 we can see that the typical experimental timescale is of the same order of magnitude of the timescale for occurrence of partial self-trapping. In conclusion our work suggests that such large values of γ can be explained in terms of a transient overshooting caused by partial self-trapping in mini-bands.

We would like also to comment on the validity of the DNLS equation for the description of experiments with ultracold atomic gases. Let us recall that the DNLS equation corresponds to a discretized version of the Gross-Pitaevskii equation for the dynamics of a Bose-Einstein condensate in the single-band approximation. The validity of this mean-field theory is not ensured for those dynamical regimes where Gross-Pitaevskii equation predicts chaos, which can be viewed as a signature of a large depletion of the condensate [143, 144, 145, 146, 147, 148, 149]. For this reason, in the presence of disorder the theory fails to predict the long time evolution

of observables directly related to small scale fluctuations and long-range coherence. However, for coarse-grained observables, like the width of the wavepacket in real and momentum space, or the participation number, the predictions of the theory remain very good even in regimes where the depletion is expected to be large, long after the random fluctuations prevent the prediction of fine scale structures. This has been recently shown in Ref. [149] by comparing the predictions of the Gross-Pitaevskii equation with one beyond mean-field theory in numerical simulations within timescales of the order of typical experiments with cold atoms and long enough to observe the effects of depletion and chaotic dynamics. Indeed our analysis is essentially based on coarse-grained observables. In addition, for each set of parameters we also average over many realizations and this extends the validity of the present approach even for longer times, as any residual dependence on small scale fluctuations is further suppressed by the averaging procedure.

5.6 Klein-Gordon model

In order to show the generality of our results we consider a different quasiperiodic model where one can observe the interplay between Anderson localization and nonlinearity; this model is a quasiperiodic version of the quartic Klein-Gordon (KG) lattice.

The Hamiltonian of this model is given by

$$H_{\mathrm{KG}} = \frac{1}{2} \sum_j \left[p_j^2 + \tilde{V}_j u_j^2 + \frac{1}{2} u_j^4 + \frac{1}{2\lambda} (u_{j+1} - u_j)^2 \right], \qquad (5.29)$$

where u_j and p_j are the generalized coordinates and momenta on the site j and $\tilde{V}_j = 1 + (1/2) \cos(2\pi\alpha j + \varphi)$. This Hamiltonian describes a set of classical coupled oscillators. Each oscillator has a linear part with a frequency that changes quasiperiodically along the lattice and a nonlinear part. The coupling between the different oscillators is restricted to neighbouring sites. The energy associated with lattice site j is

$$\mathcal{E}_j = \frac{p_j^2}{2} + \frac{\tilde{V}_j u_j^2}{2} + \frac{u_j^4}{4} + \frac{(u_{j+1} - u_j)^2}{8\lambda} + \frac{(u_{j-1} - u_j)^2}{8\lambda}. \qquad (5.30)$$

The equations of motion are generated by $\partial^2 u_j / \partial t^2 = -\partial H / \partial u_j$, yielding

$$\frac{\partial^2 u_j}{\partial t^2} = -\tilde{V}_j u_j - u_j^3 + \frac{1}{2\lambda} (u_{j+1} + u_{j-1} - 2u_j). \qquad (5.31)$$

This set of equations conserve the total energy of the system $\mathcal{H} = \sum_j \mathcal{E}_j$ which is a quantity that is strictly positive $\mathcal{H} > 0$. Note that in the DNLS model the conserved quantities are two, the norm of the wavepacket and the energy of the system; this represents a significant difference between the two models. The Klein-Gordon model has been extensively studied, since it can give a simple description of the non-dissipative dynamics of anharmonic optical lattice vibrations in molecular

crystals [150]. The total energy of the system $\mathcal{H}$ serves as a control parameter of nonlinearity, analogous to β for the DNLS model.

The coefficient $1/(2\lambda)$ in Eq. (5.29) is chosen so that the linear parts of the Hamiltonians of the KG and of the DNLS model correspond to the same eigenvalue problem. In fact, neglecting the nonlinear term and using $u_j = A_{j,\nu}e^{i\omega_\nu t}$ reduces Eq. (5.31) to the Aubry-André model (5.2) with $E_\nu = 2\lambda(\omega_\nu^2 - 1/\lambda - 1)$. As a consequence the localization properties associated to the linear part of the KG model are again those of the Aubry-André model, the parameter λ represents the disorder strength also in this case and the two energy scales associated to the linear spectrum d and Δ are calculated in the same way.

For the Klein-Gordon model we measure the spreading of wavepackets by tracking the normalized energy density $\varepsilon_j = \mathcal{E}_j/\mathcal{H}$ which plays the same role of n_j in the DNLS case. All the quantities that we have used for the study of the spreading of wavepackets within the DNLS model (w, γ, P, x) can be defined also for the KG model simply by replacing n_j with ε_J.

For small amplitudes the equation of the KG chain can be approximately mapped onto a DNLS model [151, 152, 153] using $\beta\mathcal{N} \approx 6\lambda\mathcal{H}$ where $\mathcal{N}$ is the norm of the wavepacket within the DNLS model and in our case is set equal to one. Therefore the nonlinear frequency shift within the KG model can be calculated from the small amplitude mapping and is given by $\delta \sim 6\lambda\mathcal{E}$ where $\mathcal{E}$ is an average characteristic energy associated to the initial wavepacket. Moreover, following this small amplitude mapping, all the analytics that we have discussed in the previous sections can be applied applied also to the KG model.

5.6.1   Numerical observations for the Klein Gordon model

Due to the existence of a mapping between KG and DNLS, we expect to observe the same spreading regimes in the two models. This has been already proven in purely random systems where the two models reveal similar qualitative results in a wide range of parameters [126, 129, 130, 131, 132]. Despite this similarity, the study of the KG model remains interesting for at least two reasons. On one hand, it allows for testing the generality of the results in a case where there is just one conserved quantity. This is highly nontrivial, especially for self-trapping, for which the argument based on norm and energy conservation cannot be applied in the KG model [123]. On the other hand, the KG model is advantageous from a numerical point of view. The fact that there is just one conserved quantity results in two orders of magnitude faster integration speed within the same integration error. For the numerical integration we use again a symplectic integration scheme of the SABA family [142, 129].

Similarly to what was done for the DNLS model, we initially set the compact wavepackets to span a width $L = 13$ (unless otherwise stated) centered in the lattice, such that each site has equal energy $\mathcal{E}_j = \mathcal{E} = \mathcal{H}/L$. This is implemented by setting initial momenta of $p = \pm\sqrt{2\mathcal{E}}$ with randomly assigned signs and zero coordinates. The values of initial energy densities $\mathcal{E}$ are chosen to give expected spreading regimes
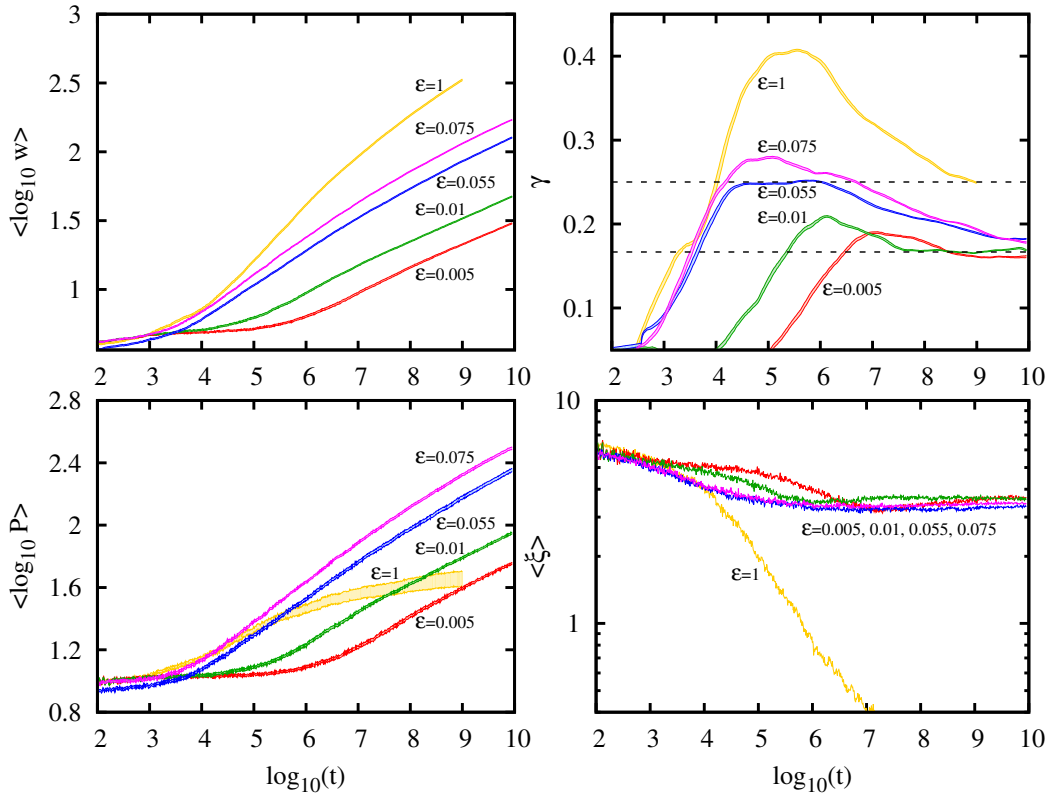
Figure 5.7: *Numerical results obtained by integrating the KG equations of motion (5.31). The time evolution of $\langle \log_{10} w \rangle$ (left panel, top), γ (right panel, top), $\langle \log_{10} P \rangle$ (left panel, bottom), and $\langle \xi \rangle$ (right panel, bottom) is shown versus $\log_{10} t$. The parameters are $\{\lambda, \mathcal{E}\} = \{2.5, 0.005\}, \{2.5, 0.01\}, \{2.5, 0.055\}, \{2.5, 0.075\}, \{2.5, 1.0\}$. We used an initial wavepacket with width $L = 13$ for $\mathcal{E} = 0.005, 0.01, 0.075, 1$ and $L = 11$ for $\mathcal{E} = 0.075$. The width of the lines for the quantities $\langle \log_{10} w \rangle$, $\langle \log_{10} P \rangle$ and γ represents the statistical error as in Fig. 5.4. In the top right panel the two dashed lines correspond to theoretically predicted power laws $\gamma = 1/6$ and $\gamma = 1/4$.*

of asymptotic weak chaos, intermediate strong chaos, and dynamical crossover from strong chaos to the slower weak chaos subdiffusive spreading [130].

The results of the time simulations are shown in Fig. 5.7, while the expected spreading regimes are given in Fig. 5.2 (full upward triangles). As one can see by comparing Fig. 5.7 with Fig. 5.4, the qualitative behaviour of the two models is rather similar. After initial transients, which increase with decreasing nonlinearity, all KG simulations reveal subdiffusive growth of the width w according to power law $w \sim t^{\gamma}$ with $\gamma < 0.5$. If self-trapping is avoided, all simulations show a similar subdiffusive behaviour for the participation number; moreover, the wavepackets remain

compact as they spread, since the compactness index at the largest computational times saturates around a constant value. For the two smallest values of initial energy density $\mathcal{E} = 0.05$ and $\mathcal{E} = 0.01$, the characteristics of the weak chaos regime are observed, namely, the exponent γ saturates around 1/6 (red and green curves in Fig. 5.7) after a transient time. We stress that the only difference from the purely random systems is the overshooting phenomenon at transient times. This effect is an inherent property of quasiperiodic systems which inevitably manifests itself in all spreading regimes, while in the disordered case it was shown to occur only in the regime of self-trapping [131, 132].

For the two energy densities $\mathcal{E} = 0.055$ and 0.075 we suggest strong chaos, with characteristics similar to the DNLS case. The simulation with $\mathcal{E} = 0.055$ (blue curves in Fig. 5.7) indeed exhibits the typical behaviour of the strong chaos scenario: the characteristic exponent γ increases up to predicted value 1/4 and remains so for about two time decades, followed by a crossover with γ decreasing to the weak chaos dynamics. There is also another possibility for larger $\mathcal{E} = 0.075$, when intermediate strong chaos is masked due to partial self-trapping (magenta curves in Fig. 5.7). Thus, γ shows values larger then 1/4 but still with subsequent decay to slower subdiffusion. Here, we would like to strongly emphasize that none of the simulations exhibit pronounced deviations from strong or weak chaos regimes of spreading, i.e. long-lasting overshooting with $\gamma > 1/4$, or significant slowing down to values $\gamma < 1/6$.

Finally, for $\mathcal{E} = 1.0$ the dynamics enters the self-trapping regime, as our theory predicts. There, a major part of the initial wavepacket stays localized, while the remainder spreads (yellow curves in Fig. 5.7). The participation number, therefore, does not grow significantly and $\langle \log_{10} P \rangle$ starts to level off at large times (Fig. 5.7, left panel, bottom, yellow curve). In contrast, the small spreading portion yields a continuous increase of the width w (Fig. 5.7, left panel, top, yellow curve), which initially is characterized by large values of $\gamma > 1/4$ (howbeit, for larger time γ decreases). Consequently, the compactness index $\langle \xi \rangle$ (Fig. 5.7, right panel, bottom, yellow curve) drops down to small values indicating deep self-trapping regime. Note that a similar behaviour has been observed before in purely random systems [131, 132]. Unusually large values of γ can be explained by local trapping-detrapping processes in the evolving wavepacket. The corresponding dynamics is in strong non-equilibrium and its theoretical description has yet to be developed.

The results discussed in this section reveal that the evolution of wavepackets in the KG model can be interpreted in terms of the spreading regimes discussed in section 5.3 and show the generality of our theoretical interpretation.

Delocalization phenomena in 1D models with correlated disorder

Interference effects induced by random potentials deeply modify the transport properties of quantum particles and can lead to a very surprising effect: a complete absence of diffusion [1]. As we have seen in chapter 2, the onset of localization crucially depends on the dimensionality of the system [7]. In particular it is known that Anderson localization always occurs in one and two dimensions, no matter how weak is the disorder, while in three dimensions localization takes place depending on the disorder strength and on the energy of the particle. In particular in 1D the effect of disorder is known to be the strongest and several proofs of localization have been given [4, 5, 53].

These statements are true as long as the disordered is uncorrelated. A natural question is to what extent these results still holds if the uncorrelation condition is relaxed. This is the main topic of this chapter.

In nature, strictly speaking, uncorrelated disorder does not exist, and this is why this topic attracted a lot of attention in the last decades [30]. Very often the potential is assumed to be uncorrelated because mathematical proofs are much easier in this case. In some contexts, like condensed matter physics, the replacement of the real potential with an uncorrelated one is not the strongest approximation and therefore is somehow justified. In some other cases this replacement represents a good approximation since one is interested only in waves with a typical wavelength larger than the correlation length of the potential [39]. However there are also situations where the role of correlations can be relevant. For instance experimental evidences of delocalization effects produced by correlations have been detected in semiconductor superlattices [154] or using microwaves propagating in disordered waveguides [155].

Effects of correlations are also observable with ultracold atoms. On the one hand bichromatic optical lattices provide a realization of a quasiperiodic system which exhibits a transition from extended to localized states already in 1D; this systems represent a limiting case where the potential is not random and correlations do not decay in space [25]. On the other hand, remaining in the context of non-deterministic random systems, experiments in speckle potentials show the existence of states whose localization length is significantly enhanced by correlations [156, 24].

From the theoretical side great attention has been given to the role played by correlations in the determination of the localization properties of 1D systems. It is well established that quasiperiodic systems can exhibit localized or extended states

depending on the parameters of the potential (cfr. chapter 3). As regards truly random one dimensional systems, instead, the fact that correlations have a delocalization effect is widely accepted, though the presence of a band of metallic states and of a mobility edge introduced by correlations is still an open problem.

The first evidences of extended states in 1D systems were found in modified versions of the Anderson model [157, 158]. These papers considered on-site energies such to form dimeric structures which present no backscattering for certain resonant modes. This leads to a discrete set of extended/metallic states but not to a true mobility edge, since an entire band of extended states is missing. Nevertheless correlations have a strong effect on the transport properties of the system and induce a superdiffusive spreading of initially confined wavepackets. Among these models the most well known examples are the random dimer model and its dual counterpart [158, 159]. They are characterized by random potentials with *short-range* spatial correlations: the two point correlation function, $C(\ell)$, decays exponentially on a typical length $\bar{\ell}$ with $\pi/k_{max} < \bar{\ell} \ll L$, L being the system size and k_{max} the largest wavevector allowed by the system.

The role played by correlations has been extensively studied also for disordered potentials that present a spectral function $S(k)$, which is the Fourier transform of $C(\ell)$, that vanishes in a finite k-region. It was initially claimed that these kind of potentials might give rise to bands of extended states in 1D [160], but later it has been recognized that those states are not really extended; they exhibit an abrupt increase of the localization length mimicking the presence of a mobility edge in finite-size systems [161]. This is, for instance, the case of speckle potentials [162, 47] that we mentioned before.

Another interesting class of disordered potentials are those which exhibit *long range* correlations. In this case both $C(\ell)$ and $S(k)$ are nonzero over the whole real and k space. There are no length scales characterizing the disorder and typically the correlation function is assumed to decay as a power law $C(\ell) \propto \ell^{-\beta}$. In this case, it has been observed that correlations can have different effects depending on the region of the spectrum under consideration. In particular, for discrete models, a reduction of the localization length has been observed at the band edges while an enhancement has been reported at the band center [163]. In this context also the presence of mobility edges has been claimed [164], although these results stirred some controversy [165, 166].

Finally, let us mention that the presence of a mobility edge in 1D has been recently reported for deterministic non-quasiperiodic potentials [167].

Very often, especially in the case of long range correlations, these studies relies on toy models characterized by ad-hoc correlation functions, creating almost no connection with possible experimental implementations. In this chapter we propose a physical model for a random potential where long-range and short-range correlations arise naturally from the system itself and which is also realizable using dipolar ultracold gases.

The model considers a series of dipoles pinned at random positions in the minima of a deep optical lattice. Due to the repulsive interactions among these dipoles
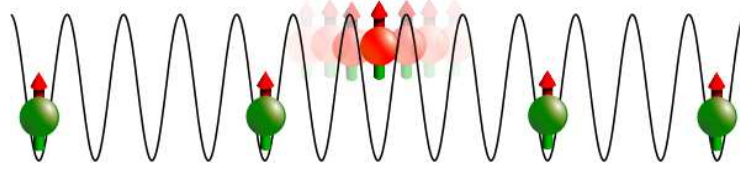
Figure 6.1: *Schematic representation of the physical model. A set of dipoles (green spheres) are trapped at random positions in the minima of a deep optical lattice and play the role of impurities. One test dipole (red sphere) is excited to another internal level and feels a shallower external potential. The test dipole can tunnel through the lattice subject to the random potential originating from the dipolar interaction with the impurities.*

there will be a correlation in the way in which they are positioned in the lattice and in particular they will have the tendency to sit far away from each other. This set of trapped dipoles, referred as *impurities*, is assumed to create a disordered potential for another dipole, the *test dipole*, which is excited to another internal level and is assumed to be free to move through the lattice (see Fig. 6.1). Short range correlations arises from the distribution of the impurities, while long range correlations are due to the dipolar interaction between the test dipole and the impurities.

In the following we study the localization properties of the test dipole in the correlated potential realized by the impurities, highlighting the role played by short and range correlations. In particular, as the parameters of the model are changed, we observe that short range correlations can introduce a discrete set of extended states in the system, while long range correlations tend to restore localization and lead to counterintuitive effects on the localization length of the system.

The chapter is organized as follows. First of all in section 6.1 we give a brief introduction on the dipole-dipole interaction. The model is presented in detail in section 6.2 and the Hamiltonian describing the properties of the test dipole is derived. In section 6.3 we characterize the statistical properties of the random potential formed by the impurities. Then, in section 6.4 we study the localization properties of the model by using a renormalization-decimation scheme for the calculation of the localization length. Finally a detailed discussion of the role played by short and long correlations is presented in section 6.5.

6.1 Dipolar interaction

Let us consider two particles with dipole moments pointing in the directions identified by the two unit vectors $\vec{e}_1$ and $\vec{e}_2$ and whose relative position is $\vec{r}$. The potential energy associated to the dipole-dipole interaction between the two particles is given by

$$U_{dd}(\vec{r}) = \frac{\mathcal{A}_{dd}}{4\pi} \frac{(\vec{e}_1 \cdot \vec{e}_2)|\vec{r}|^2 - 3(\vec{e}_1 \cdot \vec{r})(\vec{e}_2 \cdot \vec{r})}{|\vec{r}|^5},$$

(6.1)
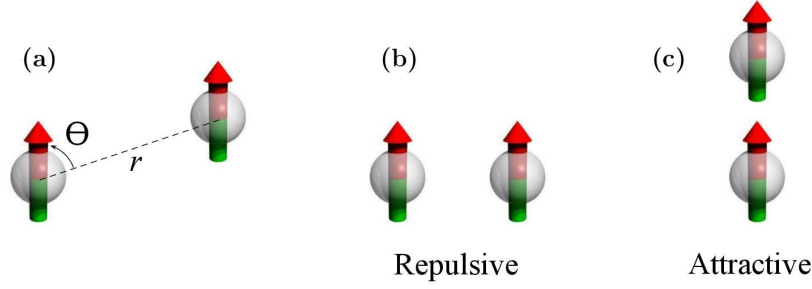
Figure 6.2: *Interaction between polarized dipoles (a). Two polarized dipoles placed side by side repel each other (b) while dipoles in a "head to tail" configuration attract each other (c). Figure taken from ref. [168].*

where the coupling constant $\mathcal{A}_{dd}$ quantifies the strength of the dipolar interaction and is given by different expressions depending on the physical origin of the dipole force. For particles having a permanent magnetic moment, μ, the coupling constant $\mathcal{A}_{dd}$ is $\mu_0\mu^2$, where μ_0 is the permeability of vacuum; for particles having a permanent electric dipole moment, p, $\mathcal{A}_{dd}$ is given by p^2/ε_0, where ε_0 is the permittivity of vacuum. For a polarized sample, where all dipoles point in the same direction, the dipolar interaction takes a simpler form [168]:

$$U_{dd}(\vec{r}) = \frac{\mathcal{A}_{dd}}{4\pi}\frac{1-3\cos^2(\Theta)}{|\vec{r}|^3}. \tag{6.2}$$

where Θ is the angle between the relative position $\vec{r}$ and the dipole orientation (Fig. 6.2). The main property of the dipole-dipole interaction is yo be *long range* and *anisotropic*. The long range character of the interaction is due to the fact that it decreases with the cube of the distance $U_{dd} \sim 1/|\vec{r}|^3$. The anisotropy is instead given by its angular dependence. As Θ is varied from 0 to $\pi/2$ the function $\left(1-3\cos^2(\Theta)\right)$ changes sign and the dipole-dipole interaction changes from positive to repulsive. In Fig. 6.2 we show the two limiting situations of particles sitting side by side where the interaction is maximally repulsive (b) and of dipoles in a "head-to-tail" configuration where the interaction is maximally attractive (c). For the special value $\Theta_M = \arccos(1/\sqrt{3}) \approx 54.7°$, the so-called "magic-angle", the dipole-dipole interaction vanishes.

There are several candidates to experimentally realize a dipolar quantum gas: molecules having a permanent electric dipole moment p, Rydberg atoms, which can have very large induced electric dipole moments, or ground state atoms having a large magnetic moment μ [169]. So far quantum degeneracy has been reached only in the last case with three different atomic species: Chromium ($\mu = 6\mu_B$, where μ_B is the Bohr magneton), Dysprosium ($\mu = 10\mu_B$) and Erbium ($\mu = 7\mu_B$). Chromium was condensed in 2005 [170] and, since then, it allowed for the first experimental investigations of the unique properties of dipolar quantum gases [171, 169]. More recently a Bose-Einstein condensate [172] and a degenerate Fermi gas

[173] of Dysprosium have been produced. The last species that has been condensed is Erbium [174].

6.2   The physical model

Let us consider a very dilute ultracold dipolar gas in a deep one dimensional optical lattice, which forbids tunneling between sites. The gas feels also the presence of a strong harmonic confinement placed in the directions perpendicular to the lattice that reduces the effective dimensionality of the system to 1D.

We assume that the dipoles are trapped at random positions at the minima of the lattice and that they are polarized perpendicularly with respect to the lattice axis, so that dipole-dipole interaction is repulsive. In this way, for small densities and large dipole-dipole interaction, there are no double occupancies, and moreover we can assume that the dipoles will occupy sites far away from each other. In particular the interaction is taken to be strong enough so that each dipole has to be preceded and followed by at least two empty sites. In the following we refer to this set of trapped dipoles as *impurities*.

One dipole, that we refer to as the *test dipole*, is excited to another internal state, so that, unlike the impurities [50, 51], it feels a shallower optical lattice and it is free to hop between different sites. In this situation we can describe the test dipole as a single particle that feels the presence of a random potential that originates from the dipolar interaction with the impurities pinned in the lattice. This random potential is characterized by the presence of both short range and long range correlations and its statistical properties will be characterized in detail in section 6.3. The physical model that we have just described is schematically represented in Fig. 6.1.

Assuming that the motion of the dipolar impurities is frozen and that the radial confinement is so strong that all the atoms lie in the lowest level of the radial harmonic trap, the motion of the test particle of mass m along the lattice axis z can be described using the following Hamiltonian

$$H = -\frac{\hbar^2}{2m}\frac{\partial^2}{\partial z^2} + s_{(T)}E_R\sin^2(kz) + V_d(z),\qquad(6.3)$$

where $k = 2\pi/\lambda$ is the wavenumber of the laser generating the optical lattice of spacing $d = \lambda/2$, $E_R = \hbar^2 k^2/2m$ is the recoil energy and $s_{(T)}$ is the dimensionless lattice strength felt by the test particle. The potential $V_d(z)$ represents the random potential resulting from the dipolar interaction of the test particle with the impurities trapped in the lattice and it can be written as follows

$$V_d(z) = \int dz' \rho(z')U_{dd}^{1D}(z - z').\qquad(6.4)$$

Here we have introduced the function $\rho(z)$ which describes the density distribution of the impurities along the z direction. The potential $U_{dd}^{1D}(z)$ is the effective one dimensional dipolar interaction obtained after integration of the dipolar interaction in the radial direction. In our model we do not include contact interactions, with

the underlying idea that they can be switched off by exploiting Feshbach resonances [168, 175, 169]. The density function $\rho(z)$ can be calculated assuming that in the z direction each impurity occupies a Wannier state $w^{(I)}(z)$ and therefore the full density is given by a sum of Wannier functions localized around the sites occupied by the impurities, that we label with $\bar{l}$:

$$\rho(z) = \sum_{\bar{l}} |w^{(I)}(z - \bar{l}d)|^2. \tag{6.5}$$

The Wannier states of the impurities are calculated imposing that they feel an optical lattice which is much deeper than the one felt by the test particle $s_{(I)} >> s_{(T)}$. The effective one dimensional potential $U_{dd}^{1D}(z)$ is obtained assuming that both the test particle and the impurities occupy the lowest radial state of the harmonic confinement

$$\phi_\omega(\vec{r}_\perp) = \frac{1}{\sqrt{\pi}\sigma_\omega} e^{-r_\perp^2/2\sigma_\omega^2} \qquad \text{with} \qquad \sigma_\omega = \sqrt{\frac{\hbar}{m\omega}} \tag{6.6}$$

and is given by the following expression

$$U_{dd}^{1D}(z) = \int d\vec{r'}_\perp d\vec{r}_\perp |\phi_{\omega^{(I)}}(\vec{r'}_\perp)|^2 |\phi_{\omega^{(T)}}(\vec{r}_\perp)|^2 U_{dd}(\vec{r} - \vec{r'}). \tag{6.7}$$

where $\omega^{(I)}$ and $\omega^{(T)}$ are the frequencies of the radial harmonic trapping felt by the impurities and by the test dipole respectively. Solving the integral in Eq. (6.7) one obtains [176]

$$U_{dd}^{1D}(z) = \frac{\mathcal{A}_{dd}}{4\pi\sigma_\perp^3}(1 - 3\cos^2\alpha)\times$$
$$\times \left\{ -\frac{2}{3}\delta\left(\frac{z}{\sigma_\perp}\right) + \frac{1}{2}\sqrt{\frac{\pi}{2}} e^{\frac{1}{2}\frac{z^2}{\sigma_\perp^2}} \left[\left(\frac{z^2}{\sigma_\perp^2}\right) + 1 \right] \text{Erfc}\left(\frac{|z|}{\sqrt{2}\sigma_\perp}\right) - \frac{|z|}{2\sigma_\perp} \right\}. \tag{6.8}$$

where $\sigma_\perp = \sqrt{(\sigma_{\omega^{(I)}}^2 + \sigma_{\omega^{(T)}}^2)/2}$, α is the angle between the direction of the dipole and the z axis, that in our case is equal to $\pi/2$, and $\text{Erfc}(z)$ is the complementary error function

$$\text{Erfc}(z) = \frac{2}{\sqrt{\pi}} \int_z^\infty e^{-t^2} dt. \tag{6.9}$$

Note that $U_{dd}^{1D}(z)$ is composed by two parts: a Dirac delta term that is strongly peaked around $z = 0$ and a slowly decaying part formed by the second and the third term. One can show that at large distances $|z| \gg \sigma_\perp$ the slowly decaying part reproduces the typical behaviour of a dipolar interaction, namely it decreases with the cube of distance $U_{dd}^{1D}(z) \sim \mathcal{A}_{dd}(1 - 3\cos^2\alpha)/|z|^3$.

A tight binding form of Hamiltonian (6.3) is obtained by using a set of Wannier states $w_n(z)$ as a basis for the states of the test particle (see appendix A for an introduction on Wannier functions) and by following a discretization procedure

similar to the one illustrated in section 3.1. For the case of a single dipolar impurity pinned at site l the Hamiltonian of the test particle is

$$
\begin{aligned}
H_{(1)} = & - J \sum_n \left(\mid w_n \rangle \langle w_{n+1} \mid + \mid w_{n+1} \rangle \langle w_n \mid \right) \\
& - J^d \left(\mid w_l \rangle \langle w_{l \pm 1} \mid + \mid w_{l \pm 1} \rangle \langle w_l \mid \right) + \sum_n u_{n-l}^{dd} \mid w_n \rangle \langle w_n \mid .
\end{aligned} \tag{6.10}
$$

In Eq. (6.10) we have included the standard nearest neighbour tunneling term J (cfr. Eq (3.6) of section 3.1) and two contributions due to the dipolar interaction; the first represents a nearest neighbour dipolar assisted hopping J^d, the second is the on-site energy u_{n-l}^{dd} at site n. They can be calculated as follows

$$
\begin{aligned}
J &= - \int w_n^*(z) \left[-\frac{\hbar^2}{2m} \frac{d^2}{dz^2} + s E_R \sin^2(kz) \right] w_{n+1}(z) \, dz, \\
J^d &= - \int w_l(z) w_{l+1}(z) |w_l^{(I)}(z')|^2 U_{dd}^{1D}(z - z') \, dz \, dz', \\
u_{n-l}^{dd} &= \int |w_n(z)|^2 |w_l^{(I)}(z')|^2 U_{dd}^{1D}(z - z') \, dz \, dz'.
\end{aligned} \tag{6.11}
$$

Note that the function u_n^{dd} can be interpreted as the dipolar interaction between a single impurity and the test particle in the discretized formalism. In fact the on-site energy simply depends on the distance $|n - l|$ between the test particle and the impurity.

In Fig. 6.3 we show the behaviour of the quantities $\theta = (J + J^d)/J$ and $\lambda_{n-l} = u_{n-l}^{dd}/J$ for $|n - l| = 0, 1, 2$ as a function of $\sigma_\perp$ for the case of $\mathcal{A}_{dd} = 0.49 \hbar^2 \lambda/m$, $s_{(T)} = 6$ and $s_{(I)} = 30$. This value of $\mathcal{A}_{dd}$ corresponds to the dipolar moment of Dysprosium atoms trapped in an optical lattice generated by a laser of wavelength $\lambda = 570$ nm.

We note that, for this choice of parameters, we can reasonably set $\theta = 1$ ($J^d = 0$) and the on site energies for $|n - l| \geq 2$ can be approximated with the asymptotic expression $\lambda_{n-l} = \lambda/|n - l|^3$ with $\lambda = (\mathcal{A}_{dd}/Jd^3)$. They are therefore independent on the value of $\sigma_\perp$. Also λ_1 does not depend significantly on the radial confinement. Conversely the value of λ_0 strongly depends on $\sigma_\perp$ and it can even vanish and become negative. This is due to the fact that the dipolar interaction changes sign depending on the relative position of the two dipoles and therefore the integral for the calculation of u_0^{dd} has both positive and negative contributions.

In presence of several, randomly placed impurities the on-site energies have to be calculated summing over all the different contributions. The on-site energies are therefore given by

$$
\varepsilon_n = \sum_{\bar{l}} u_{n-\bar{l}}^{dd} = \sum_l \rho_l u_{n-l}^{dd} \tag{6.12}
$$

where the index in the first summation, $\bar{l}$, runs only over the sites occupied by an impurity. This summation can be conveniently rewritten by summing over all sites
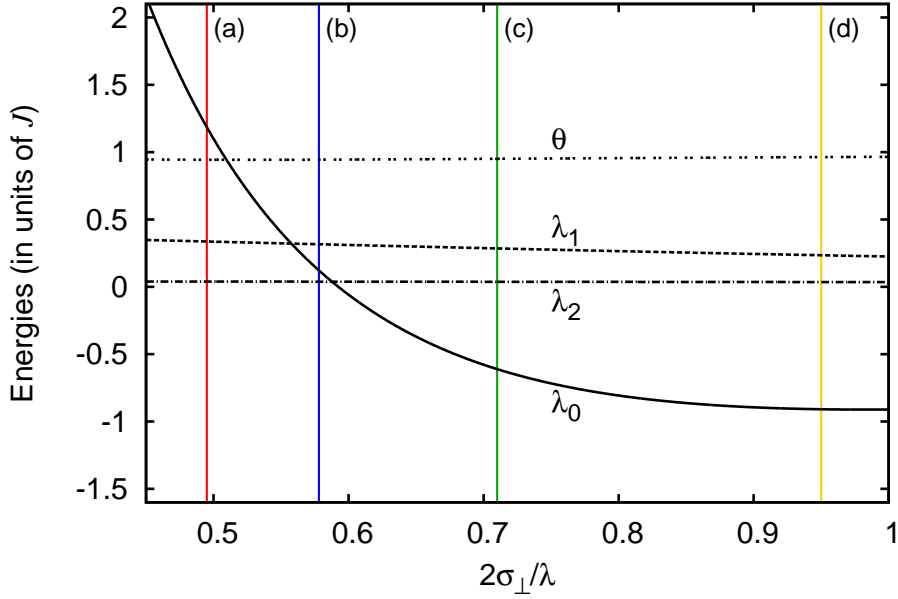
Figure 6.3: *Site energies λ_0, λ_1 and λ_2, and hopping energy θ as function of $\sigma_\perp$ in units of $\lambda/(2\pi)$, for the dipolar coupling of Dysprosium atoms corresponding to $\mathcal{A}_{dd} = 0.49 \times \hbar^2 \lambda/m$, $\lambda = 570$, $s_{(T)} = 6$, $s_{(I)} = 30$ and $\alpha = \pi/2$. The colored vertical lines labelled by different letters represent the set of values that we used for the calculation of the localization properties of the system.*

and introducing a discretized impurity density ρ_l, which is equal to 1 for occupied sites and 0 otherwise. The final Hamiltonian takes the following form

$$H = -J \sum_n \left(| \, w_n \rangle\langle w_{n+1} \, | + | \, w_{n+1} \rangle\langle w_n \, | \right) + \sum_n \varepsilon_n \, | \, w_n \rangle\langle w_n \, | \, . \qquad (6.13)$$

6.3   Statistical properties of the random potential

We characterize the random potential generated by the dipolar impurities by calculating its average value $\langle \varepsilon_n \rangle$ and the two point correlation function $C_\varepsilon(\ell) = \langle \varepsilon_n \varepsilon_{n+\ell} \rangle$. To start with, let us study separately the properties of the density ρ_n and of the dipolar interaction u_n^{dd}.

The density ρ_n is a stochastic variable and we can introduce its average value and the two point correlation function:

$$\langle \rho_n \rangle = \mathcal{C} \qquad (6.14)$$

$$\langle \rho_n \rho_{n+\ell} \rangle = C_\rho(\ell) \qquad (6.15)$$

where $\mathcal{C}$ defines the impurity concentration. Note that, if we impose that the minimum distance between impurities is two sites, then the maximum value allowed for

the concentration is $\mathcal{C} = 1/3$. We can also introduce two quantities associated to the shape of the interaction potential between the test dipole and a single impurity, u_n^{dd}:

$$\overline{u^{dd}} = \sum_n u_n^{dd} \tag{6.16}$$

$$C_u(\ell) = \sum_n u_n^{dd} u_{n+\ell}^{dd} \tag{6.17}$$

which can be thought as an average value and a two point correlation function.

The statistical properties of the full potential can be derived from those of ρ_n and from the shape of u_n^{dd}. In particular one can prove that

$$\langle \varepsilon_l \rangle = \mathcal{C} \overline{u^{dd}} \tag{6.18}$$

$$C_\varepsilon(\ell) = \sum_j C_\rho(\ell - j) C_u(j). \tag{6.19}$$

Therefore the average value of the full potential is simply given by the product of the impurity concentration and the average value of the interaction potential $\overline{u_{dd}}$, while the two point correlation function is given by the convolution of $C_u(\ell)$ and $C_\rho(\ell)$. For the full potential let us also introduce the reduced correlation function, defined as

$$c_\varepsilon(\ell) = \frac{\langle \varepsilon_l \varepsilon_{l+\ell} \rangle - \langle \varepsilon_l \rangle^2}{\langle \varepsilon_l^2 \rangle - \langle \varepsilon_l \rangle^2} \tag{6.20}$$

and the associated spectral density

$$S(k) = \sum_\ell c_\varepsilon(\ell) e^{ik\ell}. \tag{6.21}$$

In the following we will use the square root of the variance of the full potential to quantify the potential strength $W = \sqrt{\langle \varepsilon_n^2 \rangle - \langle \varepsilon_n \rangle^2}$.

For our specific case, where the random impurities have a minimum distance which is equal to two sites, the quantity $C_\rho(\ell)$ satisfies the following recursive relation:

$$C_\rho(\ell) = \frac{1}{1 - 2\mathcal{C}} \left[\mathcal{C} C_\rho(\ell - 3) + (1 - 3\mathcal{C}) C_\rho(\ell - 1) \right]. \tag{6.22}$$

Solving this equation with the assumption that $C_\rho(0) = \mathcal{C}$, $C_\rho(1) = 0$, $C_\rho(2) = 0$ one obtains

$$C_\rho(\ell) = \mathcal{C}^2 + \left(\frac{\mathcal{C}}{1 - 2\mathcal{C}} \right)^{\ell/2} \left[A \cos(\kappa \ell) + B \sin(\kappa \ell) \right], \tag{6.23}$$

with

$$\begin{aligned} \kappa &= \pi - \operatorname{atan}\left(\sqrt{(4 - 9\mathcal{C})/\mathcal{C}} \right) \\ A &= \mathcal{C} - \mathcal{C}^2 \\ B &= -[\sqrt{\mathcal{C}^3(1 - 2\mathcal{C})} + (\mathcal{C} - \mathcal{C}^2)\cos(\kappa)]/\sin(\kappa). \end{aligned} \tag{6.24}$$

Eq. (6.23) represents an oscillating function whose envelope decays exponentially. For large values of ℓ it tends to the value which is expected for uncorrelated sites, i.e., $\mathcal{C}^2$.

As regards $C_u(\ell)$, its form depends on the specific parameters of the system. However, as a general result, by approximating the sum in (6.17) with an integral, one can show that at large distances its behaviour is determined by the typical shape of the dipolar interaction, i.e., $C_u(\ell)$ decays with the cube of the distance, $\lim_{\ell \to \infty} C_u(\ell) \propto 1/\ell^3$.

Thus we can conclude that the impurity distribution introduces short-range correlations, while the shape of the interaction u_n^{dd} is responsible for long-range correlations. The role and the competition between these two effects will be extensively discussed in the next sections.

6.4 Nature of the spectrum

We study the nature of the test dipole spectrum by evaluating the Lyapunov exponent $\Lambda(E)$, which is equal to the inverse of the localization length $L_{loc}(E)$, by means of a renormalization-decimation scheme (see appendix B for an introduction on the method). The method allows us to reduce the original system composed by N lattice sites to an effective dimer composed by just two sites. This is done with a renormalization procedure that removes one site of the chain and describes the remaining sites with an effective Hamiltonian. A recursive application of this renormalization procedure permits to remove all the internal sites of the chain and to describe the whole system with a single dimer formed by the first and the last site of the chain, with on-site energies that we indicate with $\tilde{\varepsilon}_1$ and $\tilde{\varepsilon}_N$, and the relative effective hopping between those two sites $\tilde{J}_{1,N}$.

The Lyapunov exponent can be calculated as

$$\Lambda(E) = [L_{loc}(E)]^{-1} = \lim_{N \to \infty} \frac{1}{N} \ln \left| \frac{G_{N,N}(E)}{G_{1,N}(E)} \right| \tag{6.25}$$

$$= -\lim_{N \to \infty} \frac{1}{N} \ln \left| \tilde{J}_{1,N}(E) \right|, \tag{6.26}$$

where $G(E) = (E - H)^{-1}$ is the Green's function associated to H at energy E, and $G_{i,j}(E) = \langle i | G(E) | j \rangle$ are the corresponding matrix elements. The first expression for $\Lambda(E)$ is a general expression [58], while the second one, which gives a direct connection between the effective hopping amplitude $\tilde{J}_{1,N}$ and the Lyapunov exponent, applies within the renormalization-decimation approach [177].

The results for the localization length $L_{loc}(E)$ of our model, obtained with a numerical implementation of the renormalization-decimation approach, are shown in the top row of Fig. 6.4. We consider increasing values of $\sigma_\perp$, corresponding to the vertical lines in Fig. 6.3 (we use a color code among figures and moreover corresponding simulations are labelled by the same letters (a), (b), (c) and (d)). Here and in the following we fix $\mathcal{C} = 1/4$, average over 100 configurations and consider system
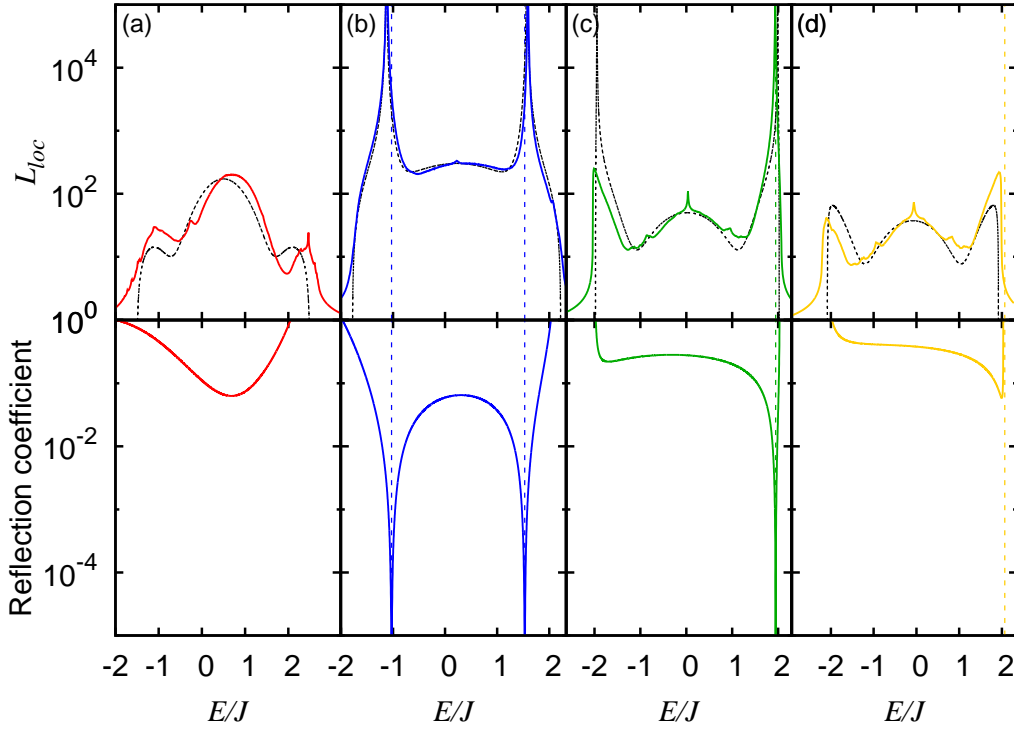
Figure 6.4: *Top panel: localization length L_{loc} in units of the lattice spacing d as a function of the energy in units of J for Hamiltonian (6.13). The black dotted lines correspond to the localization length calculated in Born approximation $L_{loc}^{(2)}$. Bottom panel: reflection coefficient $\mathcal{R}$ of the single impurity as functions of the energy in units of J. The vertical dashed lines indicates the energies for which the reflection coefficient vanishes $\mathcal{R}(E) = 0$. From left to right, different plots refers to increasing values of $\sigma_\perp$, corresponding to the vertical lines in Fig. 6.3.*

sizes up to 10^7. As the value of $\sigma_\perp$ is increased we observe very different localization regimes. Notably for certain values of $\sigma_\perp$ we observe divergences of the localization length, corresponding to the appearance of metallic states in the spectrum. This suggests the presence of delocalization effects induced by the correlations of the physical model under consideration.

More precisely, for large positive values of λ_0 all states are clearly localized since the localization length is always finite (first panel, (a)). By increasing $\sigma_\perp$, for vanishing values of λ_0 the localization length exhibits two well defined peaks in two regions of the spectrum (second panel, (b)). Increasing $\sigma_\perp$ further, corresponding to negative values of λ_0, we observe the disappearance first of one of the two divergences (third panel, (c)), and then of both of them (fourth panel, (d)). In this last panel no divergences of the localization length are observed but there are still peaks at the band edges, that recall the diverging behaviour previously observed.

The dotted black lines correspond to the localization length $L_{loc}^{(2)}$ evaluated in

Born approximation, which corresponds to a second order perturbative calculation in the disorder strength [178, 160, 30]. This calculation gives a direct connection between the spectral function $S(k)$ and the Lyapunov exponent

$$\Lambda^{(2)}(E) = [L_{loc}^{(2)}(E)]^{-1} = \frac{W^2}{J^2} \frac{S(2k(E))}{8\sin^2(k(E))} \tag{6.27}$$

where the connection between $k(E)$ and the energy is given by the following relation $E = \langle \varepsilon_n \rangle + 2J\cos(k)$. Let us note that the Born approximation gives, by construction, a symmetric localization length around the average value of the disorder $\langle \varepsilon_n \rangle$. In fact the spectral density $S(k)$ associated to $c(\ell)$ is always a symmetric function of k. Despite this fact, there is a noticeable agreement between the Born approximation and the exact numerical results.

6.5 Role of correlations

With the aim to understand why we are observing the appearance and the disappearance of metallic states in the spectrum by varying the radial confinement (and thus the 1D dipolar interaction) we analyse separately the effects due to short-range correlations and long-range correlations.

6.5.1 Short range correlations

In order to isolate the role of short range correlations in our model, we calculate the reflection coefficient for the case of a single impurity as in Eq. (6.10) and moreover we neglect the on-site contributions beyond nearest neighbour. Therefore we assume that a single dipolar impurity modifies just a trimer of on-site energies $\{\lambda_1, \lambda_0, \lambda_1\}$ and moreover we generally assume that it can modify also the hopping with nearest neighbouring sites θ.

In general, the transport properties of a system of N sites described by an Hamiltonian H are obtained by embedding it in an infinite perfect lattice with on-site energies ε and hopping energies J (see appendix B for details). This leads to a new extended Hamiltonian that we call H_{ext}. The scattering of an incoming wave $|q\rangle$ with energy $E = \varepsilon + 2J\cos(q)$ results in a reflection amplitude r that can be expressed as

$$r = G_{1,1}^0 T_{1,1} + G_{N,1}^0 T_{1,N} + G_{1,N}^0 T_{1,N} + G_{1,1}^0 T_{1,1} e^{+2iq(N-1)}, \tag{6.28}$$

T being the scattering matrix defined by

$$T = H^I \left(1 - G^0 H^I\right)^{-1}, \tag{6.29}$$

with $H^I = H_{ext} - H^0$, $H^0 = \sum_n -J(\mid w_n \rangle\langle w_{n+1} \mid + \mid w_{n+1}\rangle\langle w_n \mid)$ and G^0 is the Green's function associated to H^0. From an operational point of view, since we need to know the matrix elements of the scattering matrix T in the subspace $\xi = \{1, N\}$, we use again the renormalization procedure to evaluate them. One has to apply the

renormalization-decimation approach separately on H_{ext} and H^0 and then calculate the renormalized H^I subtracting the two. Therefore one reduces to the calculation of the reflection and transmission properties of an effective dimer.

In our specific case we are considering a single dipolar impurity and we assume it modifies just the on-site energy, the nearest neighbouring energies and the tunneling with the nearest neighbours. We have therefore a system of size $N = 3$ and we can reduce to an effective dimer with just one iteration of the renormalization procedure and this can be done analytically.

Applying the renormalization-decimation scheme and using Eq. (6.28) one obtains the following analytical formula for the reflection coefficient $\mathcal{R} = |r|^2$ of the single dipolar impurity

$$\mathcal{R} = \frac{\{\lambda_1 \left(\frac{E}{J}\right)^2 - \frac{E}{J}[1 - \theta^2 + \lambda_1^2 + \lambda_1\lambda_0] - 2\theta^2\lambda_1 + \lambda_0 + \lambda_1^2\lambda_0\}^2}{\{\lambda_1 \left(\frac{E}{J}\right)^2 - \frac{E}{J}[1 - \theta^2 + \lambda_1^2 + \lambda_1\lambda_0] - 2\theta^2\lambda_1 + \lambda_0 + \lambda_1^2\lambda_0\}^2 + \theta^4 \left[4 - \left(\frac{E}{J}\right)^2\right]}.$$
(6.30)

In the bottom row of Fig. 6.4 we plot $\mathcal{R} = |r|^2$ for the same parameters used for the calculation of the localization length, i.e. $\theta = 1$ and λ_0 and λ_1 taken from the curves in Fig. 6.3. We observe that the calculation of the reflection coefficient of the single impurity provides a very good understanding of the behaviour of the localization length: the energies where $\mathcal{R}$ tends to zero are exactly those where the localization length exhibits very large anomalous values. There is therefore a direct connection between the appearance of metallic states in the spectrum and the scattering properties of the single impurity. It has been previously shown by Dunlap *et al.* [158] that this kind of single impurity analysis can be used to interpret the transport properties of a system of size N where there are several randomly placed impurities. More precisely they proved that in such systems the number of single-particle states that show a metallic behaviour, being extended over the full system, is of the order of $\sqrt{N}$. Notably this number of delocalized states is large enough to induce transport in the system and initially localized wavepackets show a superdiffusive spreading in the disordered potential. This means that this type of extended states are detectable in typical expansion experiments that can be performed with ultracold atomic gases [24, 25].

It is remarkable that making use of the simple analytical expression (6.30) we can predict the localization properties of a rather complex system and the occurrence of metallic states in the spectrum. Studying the solutions of the equation

$$\mathcal{R}(E) = 0 \tag{6.31}$$

as a function of λ_0 and λ_1, one can extract the "phase" diagram in Fig. 6.5. We identify four different regions in the diagram depending on the number of solutions of Eq. (6.31) and on their values. More precisely, if the solutions are both imaginary, no divergences are expected and all the states are exponentially localized (red region). If the solutions are real divergences are expected, but we need to check whether they are inside or outside the single impurity spectrum $E = 2J\cos(q)$. In other words,
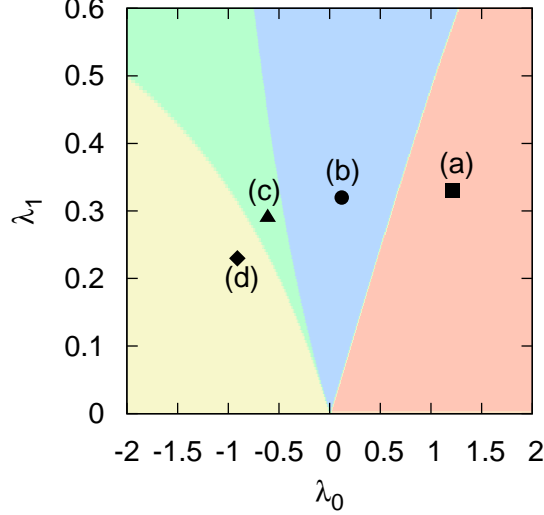
Figure 6.5: *"Phase" diagram induced by short range correlations extracted from the reflection coefficient, Eq. (6.30), for the single impurity case. Different colours correspond to different localization regimes obtained from the solution of Eq. (6.31). No real solutions of Eq. (6.31) correspond to the red region. If Eq. (6.31) has real solutions we can distinguish three cases: no solutions are in the single particle spectrum (yellow region), one solution is in the spectrum (green region), two solutions are in the spectrum (blue region). The four points in the diagram correspond to the simulations presented in Fig. 6.4 and to the values of $\sigma_\perp$ indicated by vertical lines in Fig. 6.3.*

one observes real divergences only when the roots satisfy the additional condition $|E| < 2J$. Therefore, when the solutions are real, we can identify three additional scenarios: both solutions lie outside the spectrum (yellow region), one lies inside and one outside the spectrum (green region), both lie inside the spectrum (blue region).

In the diagram we also identify with points the values of λ_0 and λ_1 corresponding to the different plots of Fig. 6.4. In Fig. 6.4 the dashed vertical lines mark the energies which verify the condition $\mathcal{R}(E) = 0$. In particular the square in the red region (a) of Fig. 6.5 corresponds to the first plot of Fig. 6.4 where all states are localized; the circle in the blue region corresponds to the second plot (b) where we observe two resonances; the triangle in the green region (c) corresponds to the third plot where we observe one resonance; and the diamond in the yellow region (d) corresponds to the last plot where there are no resonances but the peak on the right shows a tendency to diverge due to the fact that the resonance lies just outside the single impurity spectrum.

Let us recall that, in our single impurity analysis, we considered the case where one isolated dipole induces just a trimer of site energies $\{\lambda_1, \lambda_0, \lambda_1\}$ and we neglected beyond nearest neighbour contributions. In other words, we neglected the effect of long range correlations. Nonetheless the single impurity analysis describes very well the position of the resonances calculated with numerical simulations that account for the full dipolar interaction.

In the next section we study in detail the role played by the dipolar tails that we neglected in this simplified calculation and we highlight the role played by long range correlations.
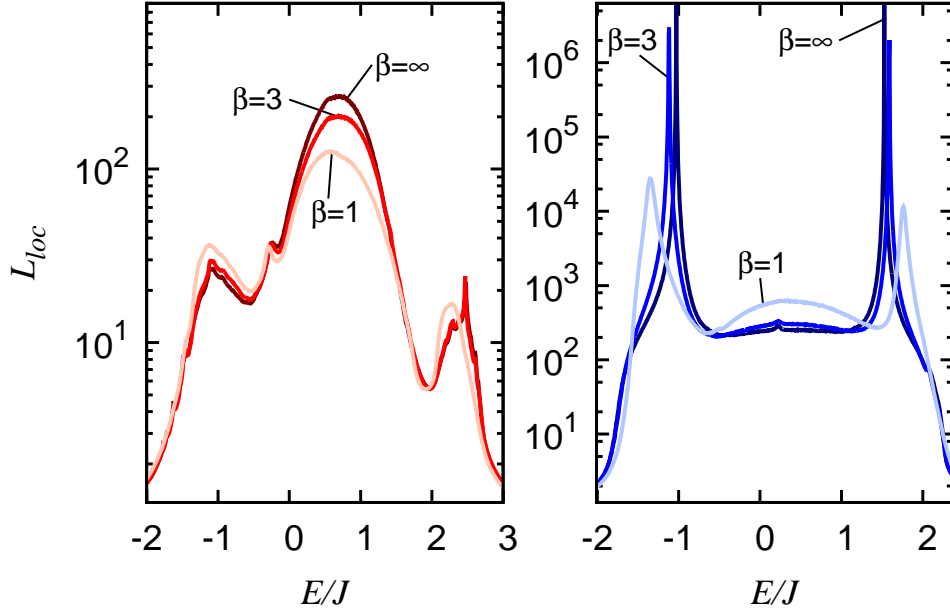
6.5.2   Long range correlations

In order to understand the role played by long range correlations and place the dipolar case in a wider context, we investigate the localization properties of a set of disordered potentials generated by impurities that interact with the test particle with an effective interaction with tails decaying as $u_n^\beta \sim 1/|n|^\beta$ where $\beta \geq 1$.

This is done placing the impurities exactly as done in the dipolar case, keeping fixed the values of λ_0 and λ_1 and choosing $\lambda_n = u_n^\beta/J = \lambda/|n|^\beta$ for $n \geq 2$. The case $\beta = 3$ ($u_n^3 = u_n^{dd}$) recovers our physical model with dipolar interactions. Moreover, once we created the potential with this procedure, we shift and normalize the on-site energies in order to obtain the same average value $\langle \varepsilon_n \rangle$ and disorder strength W that we had in the dipolar case. Following this procedure we can really analyze the effect of long range correlations keeping fixed the disorder strength W. In particular we considered values of β ranging from 1 up to 5 and we also considered the case of $\beta = \infty$ that corresponds to $\lambda_n = 0$ for $n \geq 2$.

The potential generated with this procedure has $C_\rho(\ell)$ which is unchanged and decays exponentially as previously discussed. This is due to the fact that the impurities are placed exactly in the same way as before. The correlation function associated to the interaction potential $C_u(\ell)$ is instead modified and using Eq. (6.17) one can show that it decays at large distances as $C_u(\ell) \sim 1/\ell^\beta$ for $\beta > 1$ and as $C_u(\ell) \sim \log(\ell)/\ell$ for $\beta = 1$. This asymptotic expression determines also the shape of the tails of the reduced correlation function associated to the full potential $c_\varepsilon(\ell)$.

The effects played by long range correlations are again studied by calculating numerically the localization length with the renormalization-decimation approach. In Fig. 6.6 we show the localization length L_{loc} calculated for different values of β. In particular we show a comparison between the two limiting cases of $\beta = \infty$ and $\beta = 1$ and the physical case under consideration, i.e. the dipolar case $\beta = 3$. We considered also other values of β but we do not show the results here since they are not particularly instructive. They just show an intermediate behaviour between the two limiting cases reported here.

The two panels in Fig. 6.6 correspond to two different set of parameters taken from Fig. 6.3, in the left panel we considered the case where the localization length is always finite while in the right panel the case where there are two resonances in the spectrum. Therefore the two curves for $\beta = 3$ are exactly the same curves which

Figure 6.6: *Localization length L_{loc} in units of lattice spacing as a function of the energy in units of J for different type of long range correlations identified by the asymptotic decay of the tails of the two point correlation function $C(\ell) \sim 1/\ell^{\beta}$. The two different panels correspond to two different localization regimes induced by short range correlations (see text for more details).*

are shown in the upper row of Fig. 6.4 and those are compared with the case of complete absence of long range correlations ($\beta = \infty$) and the case of very slowly decaying correlations ($\beta = 1$).

There are two main features of Fig. 6.6 that we would like to discuss here. The first is the effect introduced by long range correlations on the divergences that we have discussed in the previous section. We observe that they tend to be beveled. In fact in the $\beta = \infty$ case the localization length takes values of the order of the system size $N = 10^7$ signalling the presence of real metallic states in the system which extend over the full lattice. As the value of β is decreased the peaks in the localization length are still there but their height is decreased and they are shifted towards the band edges. This behaviour is somehow expected, since the perfect resonance condition, obtained with the single impurity calculation presented in the previous section, was neglecting the slowly decaying tails. When those tails are taken into account they tend to restore interference effects in the scattering process and reintroduce localization in the system. However, let us stress that the effect of the short range correlations remain clearly visible also in presence of long range correlations.

The second feature that we would like to highlight is the counterintuitive behaviour of L_{loc} introduced by long range correlations at the center of the band. In fact depending on the set of parameters under consideration long range correlations have an opposite effect on the localization length. In the left panel they introduce a decrease of the localization length while in the right panel they have the tendency to enhance it. This observation shows the highly nontrivial role played by long range correlations in determining the localization properties of a disordered system and indicates a richer behaviour with respect to what has been observed so far in the literature [163].

These features that we extracted from the numerical simulations reported in Fig. 6.6 are also captured within the Born approximation. We do not report the curves for $L_{loc}^{(2)}$ calculated in Born approximation, we just comment that the agreement between those curves and the exact numerical results is good, similar to what observed in Fig. 6.4.

Finally we would like to comment that we do not find the presence of mobility edges induced by long range correlations as suggested in [164, 167].

Conclusions

The observation of Anderson localization in ultracold atomic gases [24, 25] represented a turning point for the study of disordered quantum systems and provided the route for tackling a number of open questions of the theory of localization.

Stimulated by this remarkable result, in this thesis we have investigated the properties of a Bose gas in presence of quasiperiodic and random potentials. Special focus has been given to the interplay between localization and interaction and to the delocalization effects induced by the correlations of the disorder. The main results of this work are the following.

In chapter 3 we introduced quasiperiodic potentials and their implementation with bichomatic optical lattices acting on a gas of noninteracting particles. We clarified the connection of this physical problem with the discrete Aubry-André model and reviewed its localization properties showing that a transition from extended to localized states occurs already in one dimension at a critical disorder strength. One of the main goals was to fill the gap between the well known properties of the Aubry-André model and what can be actually observed in realistic experiments with ultracold gases. As a first step in this direction, we studied the diffusion of noninteracting wavepackets in a commensurate (periodic) lattice and we compared it with the case of an incommensurate (quasiperiodic) lattice. We showed that the spatial periodicity of the commensurate lattice plays a key role in determining the type of approach to the quasiperiodic limit in a sequence of commensurate approximants. This part of our analysis confirmed that the transition from diffusion to localization observed in Ref. [25] can correctly be interpreted in terms of the predictions of the Aubry-André model. As a second step we considered the properties of the same model but in momentum space. We showed the occurrence of interesting periodic oscillations in the time evolution of the momentum distribution of an expanding wavepacket. We numerically calculated the frequency and visibility of these oscillations and we introduced a simple few-mode approximation that gives a consistent interpretations of this behavior. Our analysis suggests that the oscillations of the central and side peaks in the momentum distribution can be used efficiently to probe the transition from diffusion to localization in the Aubry-André model. Our results are relevant for feasible experiments with ultracold atoms, where the momentum distribution can be detected with good resolution by performing time-of-flight measurements.

In chapters 4 and 5 we considered a weakly interacting Bose gas in a bichromatic optical lattice and dealt with the problem of the interplay between disorder induced localization and delocalization caused by repulsive interactions. In chapter 4 we

introduced the method which is used to study the expansion of an initially localized wavepacket, namely a discrete nonlinear Schrödinger equation which generalizes the Aubry-André model by introducing the interaction at the mean-field level. We numerically simulated the dynamics of matter waves starting from either a δ-function localized in a single lattice site or a Gaussian wavepacket. In the former case, we found that the dynamics is dominated by self-trapping processes in a wide range of parameters even for weak interaction. Conversely, in the latter case, self-trapping is significantly suppressed and the destruction of localization by interaction is more easily observable. In particular, we found that Gaussian wavepackets, which remain localized for noninteracting particles, start to spread subdiffusively (i.e., the width of the wavepacket grows as $w(t) \sim t^\gamma$ with $\gamma < 0.5$) in the presence of interaction. We also compared the results extracted from our theoretical model with an experimental study performed in Florence [33] that considers the expansion of a Bose-Einstein condensate with tunable interactions in a bichromatic optical lattice. Notably, a destructive effects of interactions on localization is observed also experimentally. The measured values of the spreading exponent γ indicate a subdiffusive expansion of the cloud, consistently with our numerical observations. The values of γ observed both in the numerical and experimental data show a clear deviation from those obtained for random systems and, in particular, larger values of γ are detected in the quasiperiodic case, indicating a nontrivial role played by the correlations of the potential.

In chapter 5 we focused on the phenomenon of destruction of localization in quasiperiodic systems and we characterized in detail the subdiffusive spreading for large asymptotic times. We gave particular attention to the comparison with the random case. We interpreted the spreading process in terms of resonances in the mode-mode coupling. In particular, by comparing the frequency shift induced by the interaction (nonlinearity) with the energy scales extracted from the spectrum of the underlying noninteracting (linear) system, we predicted the occurrence of three different spreading regimes. In addition to the regime of self-trapping, we identified the regimes of strong chaos and weak chaos. We also predicted the spreading exponents $\gamma = 1/6$, for weak chaos, and $\gamma = 1/4$, for strong chaos. We performed numerical simulations which last for much longer times than the simulations presented in the previous chapter 4, and we averaged our results over many realizations. This gave us the possibility to accurately calculate the spreading exponent γ and observe the weak chaos regime. A key difference with respect to random systems is the occurrence of transient overshooting regimes that we interpreted as due to the peculiar structure of the linear spectrum of the quasiperiodic system, which is separated into mini-bands. These mini-bands are responsible for peculiar mechanisms of partial self-trapping. Signatures of strong chaos have also been observed, but the temporal overlap of strong chaos and partial self-trapping makes the analysis of the spreading more complex than for random systems. We also verified that our main results do not depend on the details of the shape of the initial wavepacket. This suggests that the nonlinear frequency shift is the only parameter that controls the dynamics. Finally we compared the results obtained with the discrete nonlinear

Schrödinger equation with those obtained with a quasiperiodic version of the quartic Klein-Gordon lattice model. The results of the two models are quite similar and this supports the generality of our predictions.

In chapter 6 we considered the problem of localization of noninteraction particles in a correlated random disorder. To face this issue we proposed a novel model which is relevant both from a theoretical and an experimental point of view. From the theoretical side it presents a nontrivial interplay between the role played by short and long range correlations. From the experimental side it can be realized using a gas of ultracold dipolar atoms. We considered a set of dipolar impurities pinned in the wells of a deep optical lattice that acts as a random potential for another atom (test particle) in another internal state that feels a weaker optical lattice. An analysis of the statistical properties of the model showed that short-range correlations are due to the fact that the occupation of neighboring sites are forbidden because of repulsive dipolar interactions between impurities, while long-range correlations are due to the dipolar interaction between the test dipole and the impurities. The localization properties of the model were calculated by means of a renormalization-decimation technique which allowed us to calculate properties of very large systems and study the extended or localized nature of the states. We found that the presence of short range correlations can give rise to different regimes of localization. In particular, as the parameter of the system are changed, we observed regimes where all the states are exponentially localized and regimes where one or more discrete sets of extended states appear in the spectrum. The occurrence of the different regimes can be predicted starting from an analytical expression obtained from the scattering of a single impurity. Notably, the different localization regimes could be explored experimentally simply by changing the strength of the radial harmonic confinement. Long range correlations were studied not only for the dipolar case but also for a more general two point correlation function decaying as $C(\ell) \sim 1/\ell^\beta$ (the case $\beta = 3$ correspond to the dipolar case). We saw that long range correlations tend to restore localization in the spectrum and lead to counterintuitive behaviours of the localization length. More precisely, depending on the localization regime that are considered, they can enhance or reduce the localization length at the center of the band.

Outlooks

After the first observations of 1D Anderson localization of matter waves, the experimental activity in ultracold atoms aimed to better understand the physics of disordered systems has grown significantly. Part of the community focused on the problem of the combined effects of disorder and interaction. Some experiments considered the equilibrium properties of a Bose gas, looking for the transition from superfluid to Bose glass [67, 98, 67]. Others considered the dynamical properties focusing on the expansion of an initially localized wavepacket [33, 69]. Other groups investigated the role of dimensionality considering two dimensional and three dimen-

sional disorder. In the two dimensional case, the regime of Anderson localization has not yet been reached [179], but recently the observation of coherent backscattering of ultracold atoms has been reported [180]. This phenomenon is responsible for the so called weak localization, which can be considered as a precursor of Anderson localization. In the three dimensional case two different experiments managed to observe Anderson localization of matter waves with noninteracting bosons [71] and fermions [70].

As suggested by this stimulating scenario there are several directions that can be investigated from the theoretical point of view. A direct extension of the investigation of the interplay between interaction and localization would consists of comparing our results for the expansion of an initially localized wavepacket with those that can be found by using different approaches like, for instance, the investigation of the properties of a Bose gas at equilibrium in a box of finite size in the presence of a quasiperiodic potential and of interaction between atoms. Alternatively one may look for signatures of the destructive effect of the interactions on localization by considering the time evolution in momentum space. Another important task would be the development of beyond-mean-field theories, allowing for the investigation not only of weakly interacting, but also strongly interacting gases.

As regards the role of the correlations, there are several extensions that can be considered. Remaining in the one dimensional case, the study of the dynamics of wavepackets would provide another possible way to detect the delocalization induced by the correlations. We expect that the different localization regimes that we have predicted can lead to localization of wavepackets but also to diffusive and superdiffusive expansions. A detailed characterization of these dynamical regimes would complement our analysis and provide another input on how to detect the different regimes in feasible experiments. Another possibility is the extension of our analysis to higher dimensions. The model that we proposed can indeed be extended to 2D and 3D and, in this sense, it may serve as a powerful tool to shed light on the role played by correlations in these systems.

Wannier functions

In this appendix we give a brief introduction to the concept of Wannier functions and we explain some of their properties.

Let us consider a single particle in a one dimensional periodic potential $V(x)$ of period d, $V(x) = V(x+jd)$. This problem is described by the following Hamiltonian

$$H = -\frac{\hbar^2}{2m}\frac{\partial^2}{\partial x^2} + V(x).$$

The Bloch theorem [40] states that the eigenstates associated to H have the following form

$$\psi_{n,k}(x) = e^{ikx}u_{n,k}(x) \tag{A.1}$$

where k is the quasi-momentum, n is the band index and $u_{n,k}(x)$ is a function with the same periodicity of the potential, $u_{n,k}(x+jd) = u_{n,k}(x)$. The quasi-momentum is restricted to the first Brillouin zone $k \in [-\pi/d, \pi/d]$ and, in a finite system, it can assume N different values, where N is the number of periodic repetitions of the potential. One can easily verify that

$$\psi_{n,k}(x + jd) = e^{ijnd}\psi_{n,k}(x). \tag{A.2}$$

Any Bloch function, $\psi_{n,k}(x)$, considered as a function of k and for a fixed value of x, represents a periodic function with period $2\pi/d$. It therefore has a Fourier series expansion in plane waves with wavevectors in real space. For a fixed value of x we can write:

$$\psi_{n,k}(x) = \frac{1}{\sqrt{N}}\sum_j w_{n,j}(x)e^{ikjd}. \tag{A.3}$$

The coefficients $w_{n,j}(x)$, depend on x, on the lattice site j and on the band index n and are called *Wannier functions*. They can be calculated by the inversion formula

$$w_{n,j}(x) = \frac{1}{\sqrt{N}}\sum_k \psi_{n,k}(x)e^{-ijkd} \tag{A.4}$$

where the sum includes all the values of k in the Brillouin zone. When N is large one can substitute the sum in equation (A.4) with an integral over k.

The Wannier functions obey the following properties:

1. Their shape does not depend separately on j and x separately but only on the difference $x - jd$. This can be expressed as

$$w_{n,j+l}(x + ld) = w_{n,j}(x) \tag{A.5}$$
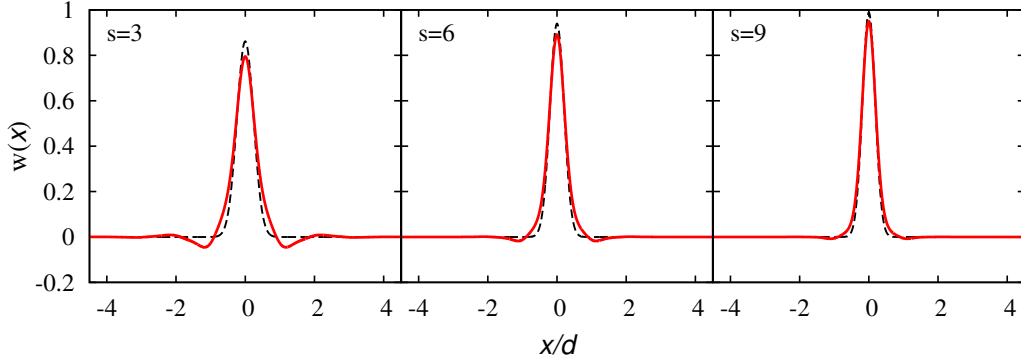
Figure A.1: *Wannier function of the lowest band $w(x)$ for a periodic potential of the form $V(x) = sE_R \sin^2(kx)$ for different values of s. The exact numerical result (red lines) is compared with the Gaussian approximation (black lines) described by Eq. (A.10)*

and it is a direct consequence of Eq. (A.4) and of the Bloch theorem. Therefore we can introduce the following notation

$$w_{n,j}(x) = w_n(x - ja). \tag{A.6}$$

2. They form a complete orthonormal set. The completeness follows from the fact that we expressed the basis of the Bloch functions as a linear combination of the Wannier functions. The orthogonality is given by

$$\int w_{j,n}^*(x)w_{j',n'}(x)\,dx = \delta_{n,n'}\delta_{j,j'}. \tag{A.7}$$

This relation can be verified using Eq. (A.4) and the orthogonality of the Bloch functions.

3. The Wannier functions of the lowest band are centered around the lattice site jd. Moreover choosing appropriate phases for the Bloch functions they are real, symmetric around jd and they rapidly go to zero away from jd [181].

Let us now consider the specific case where the potential is an optical lattice described by

$$V(x) = sE_R \sin^2(kx) \tag{A.8}$$

where $k = \pi/d$, $E_R = \hbar^2 k^2/2m$ is the recoil energy and s is the dimensionless lattice strength. Moreover we focus on the Wannier functions of the lowest band that we indicate removing the band index $w_{n=0,j}(x) = w_j(x)$. In Fig. A.1 we show a numerical calculation of the Wannier function of the lowest band $w(x)$ for different values of the strength of the optical lattice s (red solid lines). We note that $w(x)$ is symmetric and localized around the lattice site $j = 0$. As the lattice strength s is increased the Wannier function becomes more and more localized. An analytical

estimation of $w(x)$ can be obtained approximating the wells of the optical lattice with an harmonic potential

$$V(x) \approx \frac{1}{2}m\omega^2 x^2 \qquad (A.9)$$

of frequency $w = \sqrt{s}\hbar k^2/m$. The ground state of the harmonic confinement provides A Gaussian approximation of $w(x)$ and has the following form

$$w(x) \approx \left(\frac{\sqrt{s}k^2}{\pi}\right)^{1/4} \exp\left(\frac{-\sqrt{s}k^2}{2}x^2\right). \qquad (A.10)$$

In Fig. A.1 we compare this analytical expression (black dashed lines) with the exact numerical result. We observe a general good agreement between the two curves that improves for large values of s. It is important to note, anyway, that the tails of the Gaussian approximation gives always a poor description of the tails of the Wannier functions. In fact $w(x)$ decays exponentially rather than in a Gaussian manner and always has nodes in order to satisfy the orthogonality condition (A.7) [21].

Renormalization-decimation approach

This appendix is devoted to an introduction to the renormalization-decimation method. This method represents a powerful tool for the calculation of the Green's function operator based on the central idea of lowering the number of degrees of freedom of a physical system, reducing to a smaller renormalized subspace. This is done in an exact way eliminating the part of the system we are not interested in. This renormalization approach has been applied in different fields of physics as for instance the calculation of the band structure of crystals and microstructures (e.g. [182, 183]) or to the problem of localization of quantum particles in disordered or quasiperiodic systems (e.g. [184, 177]). Exhaustive introductions on this topic can be found in the literature (see for instance [185] and references therein).

This appendix is organized as follows: first we introduce the theoretical formalism of the renormalization-decimation approach. We then apply it to a specific problem which is the analysis of the localization properties of a one-dimensional tight binding Hamiltonian, focusing on the calculation of the density of states, of the Lyapunov exponent and of the transmission and reflection coefficients.

B.1 Renormalization scheme: the theoretical framework

Let us discuss the renormalization scheme in the case of a generic Hamiltonian H with N degrees of freedom. We indicate with $\mid \phi_i \rangle$ an orthonormal basis associated to this Hamiltonian

$$H = \sum_{i,j} H_{i,j} \mid \phi_i \rangle \langle \phi_j \mid, \tag{B.1}$$

where $H_{i,j} = \langle \phi_i \mid H \mid \phi_j \rangle$, and with $G(E)$ the Green's function, or resolvent, associated with H

$$G(E) = \frac{1}{E - H}. \tag{B.2}$$

Suppose now, without any loss of generality, that H can be written as the sum of two operators

$$H = H' + W \tag{B.3}$$

and indicate with G the Green's function of the full system and with G' the Green's function of H'. Then one can apply the Dyson equation

$$G = G' + G'WG \tag{B.4}$$

which is an exact relation connecting G, G' and W.

We partition now the space where H is defined into two arbitrary complementary parts that we indicate with A and B and we introduce the projection operators associated to these subspaces

$$P_A = \sum_{i \in A} \mid \phi_i \rangle \langle \phi_i \mid \tag{B.5}$$

$$P_B = \sum_{i \in B} \mid \phi_i \rangle \langle \phi_i \mid = 1 - P_A \tag{B.6}$$

Using the projector operators one can rewrite the Hamiltonian as follows

$$H = H_{AA} + H_{BB} + H_{AB} + H_{BA} \tag{B.7}$$

where $H_{I,J} = P_I H P_J$. Let us now choose explicitly the operators H' and W as follows

$$H' = H_{AA} + H_{BB} \qquad \text{and} \qquad W = H_{AB} + H_{BA}. \tag{B.8}$$

The projection procedure (B.7) can be applied also to the Green's function G and G'. Note that in the G' case the cross terms (AB and BA) are zero because the Hamiltonian H' does not include any mixing between the two subspaces A and B.

Starting from the Dyson equation and using the expression for W one can show that

$$G_{AA} = G'_{AA} + G'_{AA} H_{AB} G_{BA} \tag{B.9}$$

$$G_{BA} = G'_{BB} H_{BA} G_{AA}. \tag{B.10}$$

Combining these two equations one obtains

$$\left[(G'_{AA})^{-1} - H_{AB} G'_{BB} H_{BA} \right] G_{AA} = 1. \tag{B.11}$$

At this point writing the explicit expressions for G'_{AA} and G'_{BB} we find

$$G_{AA}(E) = \frac{1}{E - \tilde{H}_{AA}} \tag{B.12}$$

where we have introduced $\tilde{H}_{AA}$ which can be interpreted as a renormalized Hamiltonian and has the following form

$$\tilde{H}_{AA} = H_{AA} + H_{AB} \frac{1}{E - H_{BB}} H_{BA}. \tag{B.13}$$

Eqs. (B.12) and (B.13) represent an exact result which is the heart of the renormalization approach. The physical meaning is that we have eliminated one of the two subspaces of the system (B) and this allow us to describe the physics of the remaining subspace (A, which is the subspace which we are interested in) with a new renormalized Hamiltonian. The price to pay is that this new Hamiltonian is energy dependent.

B.2 Application to tight binding Hamiltonians: the decimation technique

Let us now apply the renormalization method to a tight binding Hamiltonian of form (2.9). In particular we consider the one dimensional case and we restrict hopping just to nearest neighbouring sites

$$H = \sum_j \varepsilon_j \mid j \rangle\langle j \mid + J \sum_j \mid j \rangle\langle j+1 \mid + \mid j+1 \rangle\langle j \mid \qquad (B.14)$$

with $j = 0, 1, \ldots, N$. Here, for simplicity, we have chosen, a site independent hopping energy, J, but the formalism can be easily generalized to the case where J is site dependent. The on-site energies ε_n can be chosen at will, usually the method is applied when ε_n are randomly or quasiperiodically distributed so that the localization properties becomes interesting.

The renormalization method that we introduced in the previous section can be efficiently applied if one chooses the system B in such a way that G'_{BB} is explicitly known so that the calculation of the renormalized Hamiltonian becomes straightforward. In our specific case we choose a single site of the chain. Doing this we reduce the dimensionality of the problem by one degree of freedom. Let us start removing the second site of the chain $j = 1$. In this case the renormalized Hamiltonian describing the system A is unchanged a part from three terms: the on-site energies of the sites $j = 0$ and $j = 2$ and the hopping energy connecting those two sites. Using the fact that $G'_{BB} = \frac{1}{E - \varepsilon_1} \mid 1 \rangle\langle 1 \mid$ and Eq. (B.13) we obtain

$$\varepsilon_0^{(1)} = \varepsilon_0 + J \frac{1}{E - \varepsilon_1} J$$
$$\varepsilon_2^{(1)} = \varepsilon_2 + J \frac{1}{E - \varepsilon_1} J \qquad (B.15)$$
$$J_{0,2}^{(1)} = J_{2,0}^{(1)} = J \frac{1}{E - \varepsilon_1} J$$

where the superscript (1) indicates that we are in the first iteration of the renormalization-decimation procedure. The idea is now to repeat this procedure removing sites $2, 3, \ldots$ and reducing to an effecting dimer after $N - 1$ iterations. The recursive equations that connect the renormalized quantities at the step $(i-1)$ of the procedure with those at step (i) are given by

$$\varepsilon_0^{(i)} = \varepsilon_0^{(i-1)} + J_{0,i}^{(i-1)} \frac{1}{E - \varepsilon_i^{(i-1)}} J_{0,i}^{(i-1)}$$
$$\varepsilon_{i+1}^{(i)} = \varepsilon_i + J \frac{1}{E - \varepsilon_i^{(i-1)}} J \qquad (B.16)$$
$$J_{0,i+1}^{(i)} = J_{i+1,0}^{(i)} = J_{0,i}^{(i-1)} \frac{1}{E - \varepsilon_i^{(i-1)}} J,$$

while the Hamiltonian of the effective dimer obtained after $N - 1$ iterations can be written as

$$\tilde{H}(E) = \begin{pmatrix} \varepsilon_0^{(N-1)}(E) & J_{0,N}^{(N-1)}(E) \\ J_{0,N}^{(N-1)}(E) & \varepsilon_N^{(N-1)}(E) \end{pmatrix}. \tag{B.17}$$

Using this effective Hamiltonian, which is very easy to handle since it is a simple 2×2 matrix, it is now possible to extract many interesting physical quantities related to the localization properties of the system. In the following we briefly explain how to calculate the density of states, the Lyapunov exponent and the transmission properties.

Density of states

The density of states of a system $\rho(E)$ for a non-degenerate Hamiltonian can be calculated as

$$\rho(E) = \sum_n \delta(E - E_n). \tag{B.18}$$

where E_n is an energy that belongs to the spectrum of the system. It can be related to the Green's function of the system by the following relation

$$\rho(E) = -\frac{1}{\pi} \lim_{\varepsilon \to 0^+} \text{Im} \left\{ \text{Tr} \left[G\left(E + i\varepsilon\right) \right] \right\}, \tag{B.19}$$

The connection between Eqs. (B.18) and (B.19) can be established starting from Eq. (B.19) and writing the trace on the basis of the eigenstates of the system, where H is diagonal. One gets

$$\rho(E) = \sum_n \lim_{\varepsilon \to 0^+} \frac{1}{\pi} \frac{\varepsilon}{(E - E_n)^2 + \varepsilon^2}. \tag{B.20}$$

This expression represents a sum of many Lorentzian functions $L(E - E_n; \varepsilon)$. Using that $L(x; \varepsilon) \to \delta(x)$ for $\varepsilon \to 0$ one has shown the equivalence of Eqs. (B.18) and (B.19). In the case of a tridiagonal Hamiltonian one can also show that

$$\frac{\partial}{\partial E} \ln\left[G_{0,N}(E + i\varepsilon)\right] = -\text{Tr}\left[G(E + i\varepsilon)\right]. \tag{B.21}$$

Combining this equation with (B.20) we obtain an expression for the density of states which is extremely useful for our purposes [186]:

$$\rho(E) = \frac{1}{\pi} \lim_{\varepsilon \to 0^+} \text{Im} \left\{ \frac{\partial}{\partial E} \ln\left[G_{0,N}(E + i\varepsilon)\right] \right\}. \tag{B.22}$$

This relation requires the knowledge of just one matrix element of the Green's function $G_{0,N}$ and this can be easily calculated form a direct inversion of the renormalized Hamiltonian (B.17).

Lyapunov exponent

For a 1D disordered disordered system as (B.14), a general expression of the Lyapunov exponent in terms of the Green's function matrix elements is given by [58, 177]:

$$\Lambda(E) = \lim_{N \to +\infty} \frac{1}{N} \ln \left| \frac{G_{N,N}(E)}{G_{0,N}(E)} \right|, \tag{B.23}$$

which is valid as long as the limit is well defined. This equation can be rewritten in a much more effective form substituting the explicit expressions for $G_{N,N}$ and $G_{0,N}$, obtained inverting $\tilde{H}$

$$\Lambda(E) = \lim_{N \to +\infty} \frac{1}{N} \ln \left| \frac{E - \varepsilon_0^{(N-1)}(E)}{J_{0,N}^{(N-1)}(E)} \right|. \tag{B.24}$$

In an energy region where localized states are present, this expression can be further simplified by noting that the numerator is finite, while the denominator $J_{0,N}^{(N-1)}(E) \to 0$

$$\Lambda(E) = - \lim_{N \to +\infty} \frac{1}{N} \ln \left| J_{0,N}^{(N-1)}(E) \right|, \tag{B.25}$$

this relation creates a direct and intuitive relation between the Lyapunov exponent and the effective tunneling associated to the effective dimer that represents our system.

Reflection and Transmission coefficients

In order to discuss the transmission properties of a finite size system as (B.14) we need to describe, not only the system itself, but also the incoming and the outgoing waves that are involved in the scattering process.

In our case this can be done by extending the system under consideration (formed by $N+1$ sites, form 0 to N) on the left and on the right with two semi-infinite perfect lattices. Let us therefore add at the edges of the system described by the Hamiltonian (B.14), H, two infinite series of sites with on-site energies ε and tunneling J, as illustrated in Fig. B.1 a). The new extended Hamiltonian, H_{ext}, is then decomposed in two parts: i) an infinite perfect lattice, that we indicate with H^0 ii) the remaining part of the Hamiltonian, that we indicate with H^I and is given by the difference of H_{ext} and the perfect lattice H^0

$$H_{ext} = H^0 + H^I \tag{B.26}$$

This procedure is schematically illustrated in Fig. B.1.

The transmission and reflection coefficients are then calculated using standard scattering theory. If one considers an incoming Bloch wave $| k \rangle$, eigenstate of H^0, of the form

$$\langle n | k \rangle = e^{ikn}, \tag{B.27}$$
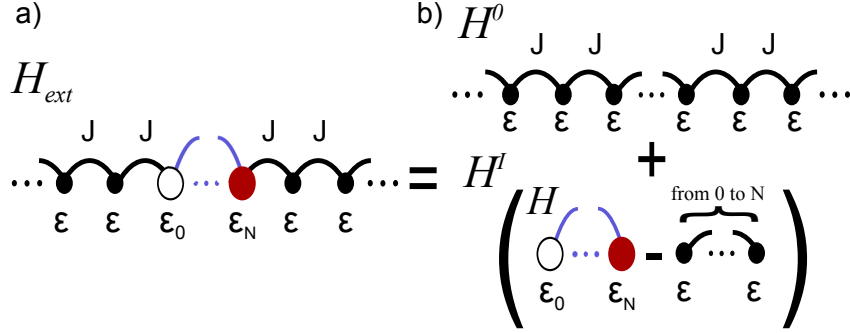
Figure B.1: *Schematic representation of the procedure used for the computation of the transmission coefficient. (a) The system under study, which extends from site 0 to site N, is connected to two semi-infinite perfect lattices on both sides. (b) This new system is formally decomposed into a perfect lattice and a perturbation responsible for the scattering of the incoming wave.*

labelled by k and with energy $E = \varepsilon + 2J\cos(k)$, then the scattering of this state produced by H^I yields the wavefunction

$$| \, \varphi \rangle = \left(1 + G^0 T\right) | \, k \rangle, \tag{B.28}$$

where G^0 is the Green's function operator associated to the perfect lattice H^0 and its matrix elements are given by [187]

$$G^0_{n,m}(E) = \left(\frac{1}{2|J|}\right)^{|n-m|} \frac{\left[-(E-\varepsilon) + \sqrt{(E-\varepsilon)^2 - 4J^2}\right]^{|n-m|}}{\sqrt{(E-\varepsilon)^2 - 4J^2}} \tag{B.29}$$

and T is the scattering matrix, which is given by

$$T = H^I \left(1 - G^0 H^I\right)^{-1}. \tag{B.30}$$

We can now combine this formalism with the renormalization-decimation approach, which allows to reduce an arbitrary Hamiltonian to an effective dimer. The effective dimer associated to H^I can be calculated by applying the renormalization-decimation procedure separately on H_{ext} and H^0 and then subtracting the two results.

At this point we are left with the calculation of the transmission and reflection coefficients of a single dimer, we can restrict our analysis to the subspace formed by the sites $[0, N]$ and H^I and T are simple 2×2 matrices. Combining expressions (B.28), (B.29) and (B.30) one can show that the scattered wavefunction takes the form $\langle n \, | \, \varphi \rangle = \tau e^{+ikn}$ in the forward direction ($n \geq N$), where τ is the transmission amplitude

$$\tau = 1 + G^0_{0,0} T_{0,0} + G^0_{0,N} T_{0,N} + G^0_{N,0} T_{N,0} e^{-2iNk} + G^0_{N,N} T_{N,N}. \tag{B.31}$$
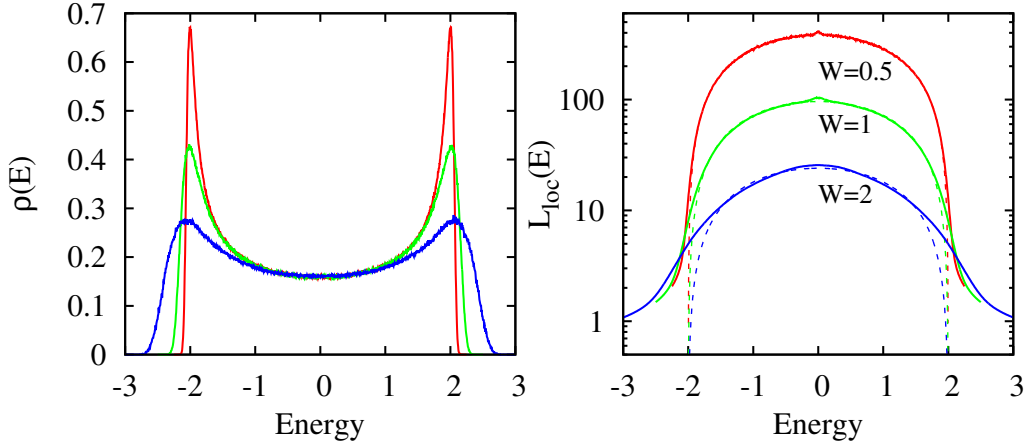
Figure B.2: *Density of states (left panel) and localization length (right panel) for the one dimensional Anderson model for different values of the disorder strength W. The solid lines are the numerical results obtained with the renormalization-truncation approach, while the dashed lines in the right panel represent a perturbative calculation for the localization length given by* (2.16).

Similarly, in the backward direction $(n \leq 0)$, $\langle n \mid \varphi \rangle = e^{+ikn} + re^{-ikn}$, r being the reflection amplitude

$$r = G^0_{0,0}T_{0,0} + G^0_{N,0}T_{0,N} + G^0_{0,N}T_{N,0} + G^0_{N,N}T_{N,N}e^{+2iNk}. \tag{B.32}$$

The transmission and the reflection coefficients are then given by $\mathcal{T} = |\tau|^2$ and $\mathcal{R} = |r|^2$.

An example of application of the renormalization-decimation approach to the one dimensional Anderson model is shown in Fig. B.2. In this case ε_n are random variables uniformly distributed in the interval $[-W/2, W/2]$, where W represents the disorder strength. We show the results of numerical calculations where we applied recursively Eqs. (B.16) and then we used expressions (B.18) and (B.23) for the calculation of the density of states $\rho(E)$ and of the localization length $L_{loc}(E) = 1/\Lambda(E)$ respectively. We also compare the numerical results for the localization length with the analytical expression (2.16) obtained in second order perturbation theory. The agreement between the two curves is very good especially where the perturbation theory is expected to give accurate results, i.e. for small values of W and close to the center of the band.

Ringraziamenti

Eccoci giunti alla fine della tesi e del mio dottorato. Guardandomi indietro posso dire di ritenermi fiero e soddisfatto del lavoro svolto e dei risultati ottenuti. A volte non è stato facile, mi sono imbattuto in ostacoli e difficoltà, ma quello che più conta è essere arrivati alla fine. Ci tengo però a sottolineare che, senza il supporto e l'aiuto di una serie di persone, non sarebbe stato possibile arrivare fin qui.

Grazie al mio supervisor, *Franco Dalfovo*, per essere stato sempre presente e per avermi seguito con costanza e dedizione. La sua esperienza in ambito accademico mi ha insegnato tanto sul mondo della ricerca e su come diventare un buon ricercatore.

Grazie a *Michele Modugno* per la fruttuosa collaborazione di questi anni, che è stata fondamentale per la realizzazione di questo lavoro di tesi.

Grazie a *Patrizia Vignolo* che si è rivelata essere una preziosa collaboratrice, ma non solo: mi ha anche aiutato al di fuori dell'ambito lavorativo con i suoi incoraggiamenti e il suo ottimismo.

Grazie a tutto il *gruppo BEC*, sia ai membri attutali, sia alle persone che sono passate da Trento durante il mio dottorato. L'atmosfera amichevole e ospitale, unita alla competenza e alla qualità dei suoi componenti, lo rendono un ambiente ottimale e stimolante per fare ricerca e discutere di fisica. Un grazie speciale ad *Alessio*, *Chiara* e *Iacopo*.

Grazie agli *amici del LENS* per l'ospitalità che mi hanno sempre offerto nelle mie visite a Firenze e per la collaborazione di questi anni. In particolare vorrei ringraziare *Giovanni Modugno*, *Eleonora*, *Marco*, *Giacomo*, *Luca* e *Chiara*.

Grazie ai miei genitori, *Sandra* e *Lino*, per avere sempre creduto in me e per avermi sostenuto in ogni momento del mio percorso universitario, a partire dai primi anni fino ad arrivare al termine del dottorato. Il loro affetto e la loro presenza non sono mai mancati e mi hanno permesso di superare momenti di stress e di difficoltà. Senza di loro il raggiungimento di questo traguardo non sarebbe stato possibile.

Grazie al mio "fratellone", *Roberto*, con il quale ho condiviso moltissimo durante il mio precorso universitario. Lo ringrazio per essere stato un fratello e anche un amico e per essere sempre stato disponibile a darmi un aiuto o un consiglio. Grazie alla mia "cognatina", *Vale Pa.*, per essersi presa mio fratello e per averlo reso così felice.

Grazie a *nonna Emilia* per il grande orgoglio dimostrato per ogni piccolo successo raggiunto dai suoi nipoti.

Grazie agli *amici fisici e matematici* con i quali ho iniziato la mia avventura universitaria; grazie perchè, nonostante siano passati nove lunghi anni e nonostante la compagnia abbia subito svariati cambiamenti, la nostra amicizia dura ancora, ed è sempre un piacere ritrovarsi per passare una serata insieme. In particolare grazie a *Stefano*, *Cri*, *Lara*, *Dalbo*, *Vale Pu.*, *Marco*, *Laura* e *Erik*. Grazie anche alle persone che sono arrivate un po' più tardi nella nostra compagnia, ma con le quali ho condiviso molto; grazie in particolare a *Poli*, *Benetti*, *Ema* e *Giacomino*.

Un ringraziamento speciale volevo dedicarlo a *Chiara*, amica sempre presente, un po' bacchettona, ma i cui consigli mi sono stati sempre preziosi. Amiche come lei non si trovano tutti i giorni.

Grazie a *Rota* e *Tenga* per portare spensieratezza e ilarità nelle mie giornate lavorative e per essere i più convinti sostenitori del Paganella basket. Menzione speciale a Rota per il supporto che mi ha fornito durante la stesura di questa tesi, il suo aiuto è stato molto apprezzato.

Grazie a *Simone* perchè le amicizie, quelle vere, sopravvivono anche a 300 Km di distanza.

Grazie a *Valentina* per l'entusiasmo e la carica che mi trasmette quotidianamente. Avere lei al mio fianco mi rende felice e mi riempie di positività. La ringrazio, in particolare, per essermi stata vicina e avermi fatto sentire il suo sostegno durante gli ultimi mesi di dottorato. Si è sempre dimostrata disponibile ad ascoltarmi e prendersi cura di me nei momenti difficili e incoraggiarmi quando più ne avevo bisogno. Le persone speciali si riconoscono anche da questi piccoli gesti.

Bibliography

[1] P. Anderson, "Absence of diffusion in certain random lattices", *Physical Review*, **109**, 1492 (1958).

[2] B. Kramer and A. MacKinnon, "Localization: theory and experiment", *Reports on Progress in Physics*, **56**, 1469 (1993).

[3] P. Lee and T. Ramakrishnan, "Disordered electronic systems", *Reviews of Modern Physics*, **57**, 287 (1985).

[4] N. F. Mott and W. Twose, "The theory of impurity conduction", *Advances in Physics*, **10**, 107 (1961).

[5] R. Borland, "The Nature of the Electronic States in Disordered One-Dimensional Systems", *Proceedings of the Royal Society of London. Series A, Mathematical and Physical Sciences*, **274**, 529 (1963).

[6] N. F. Mott, "Metal-Insulator Transition", *Review of Modern Physics*, **40**, 677 (1968).

[7] E. Abrahams, P. Anderson, D. Licciardello and T. Ramakrishnan, "Scaling theory of localization: Absence of quantum diffusion in two dimensions", *Physical Review Letters*, **42**, 673 (1979).

[8] S. John, "Electromagnetic absorption in a disordered medium near a photon mobility edge", *Physical Review Letters*, **53**, 2169 (1984).

[9] P. Anderson, "The question of classical localization A theory of white paint?", *Philosophical Magazine B*, **52**, 505 (1985).

[10] R. Dalichaouch, J. Armstrong, S. Schultz, P. Platzman and S. McCall, "Microwave localization by two-dimensional random scattering", *Nature*, **354**, 53 (1991).

[11] D. Wiersma, P. Bartolini, R. Righini and A. Lagendijk, "Localization of light in a disordered medium", *Nature*, **390**, 671 (1997).

[12] R. Weaver, "Anderson localization of ultrasound", *Wave motion*, **12**, 129 (1990).

[13] M. Anderson, J. Ensher, M. Matthews, C. Wieman and E. Cornell, "Observation of Bose-Einstein Condensation in a Dilute Atomic Vapor", *Science*, **269**, 14 (1995).

[14] K. Davis, M. Mewes, M. Andrews, N. Van Druten, D. Durfee, D. Kurn and W. Ketterle, "Bose-Einstein condensation in a gas of sodium atoms", *Physical Review Letters*, **75**, 3969 (1995).

[15] C. Bradley, C. Sackett, J. Tollett and R. Hulet, "Evidence of Bose-Einstein condensation in an atomic gas with attractive interactions", *Physical Review Letters*, **75**, 1687 (1995).

[16] M. Andrews, C. Townsend, H. Miesner, D. Durfee, D. Kurn and W. Ketterle, "Observation of interference between two Bose condensates", *Science*, **275**, 637 (1997).

[17] M. Matthews, B. Anderson, P. Haljan, D. Hall, C. Wieman and E. Cornell, "Vortices in a Bose-Einstein condensate", *Physical Review Letters*, **83**, 2498 (1999).

[18] T. Kinoshita, T. Wenger and D. Weiss, "Observation of a one-dimensional Tonks-Girardeau gas", *Science*, **305**, 1125 (2004).

[19] B. Paredes, A. Widera, V. Murg, O. Mandel, S. Fölling, I. Cirac, G. Shlyapnikov, T. Hänsch and I. Bloch, "Tonks–Girardeau gas of ultracold atoms in an optical lattice", *Nature*, **429**, 277 (2004).

[20] M. Greiner, O. Mandel, T. Esslinger, T. Hänsch, I. Bloch *et al.*, "Quantum phase transition from a superfluid to a Mott insulator in a gas of ultracold atoms", *Nature*, **415**, 39 (2002).

[21] I. Bloch, J. Dalibard and W. Zwerger, "Many-body physics with ultracold gases", *Reviews of Modern Physics*, **80**, 885 (2008).

[22] R. Grimm, M. Weidemüller and Y. Ovchinnikov, "Optical dipole traps for neutral atoms", *Advances in atomic, molecular, and optical physics*, **42**, 95 (2000).

[23] L. Fallani, C. Fort and M. Inguscio, "Bose–Einstein condensates in disordered potentials", *Advances In Atomic, Molecular, and Optical Physics*, **56**, 119 (2008).

[24] J. Billy, V. Josse, Z. Zuo, A. Bernard, B. Hambrecht, P. Lugan, D. Clément, L. Sanchez-Palencia, P. Bouyer and A. Aspect, "Direct observation of Anderson localization of matter waves in a controlled disorder", *Nature*, **453**, 891 (2008).

[25] G. Roati, D. Chiara, L. Fallani, M. Fattori, C. Fort, M. Zaccanti, G. Modugno, M. Modugno and M. Inguscio, "Anderson localization of a non-interacting Bose-Einstein condensate", *Nature*, **453**, 895 (2008).

[26] A. Aspect and M. Inguscio, "Anderson localization of ultracold atoms", *Physics today*, **62**, 30 (2009).

[27] G. Modugno, "Anderson localization in Bose–Einstein condensates", *Reports on Progress in Physics*, **73**, 102401 (2010).

[28] L. Sanchez-Palencia and M. Lewenstein, "Disordered quantum gases under control", *Nature Physics*, **6**, 87 (2010).

[29] P. Anderson, *Nobel Lectures in Physics 1971-1980*, vol. 1, (World Scientific Publishing Company Incorporated, 1992).

[30] F. Izrailev, A. Krokhin and N. Makarov, "Anomalous localization in low-dimensional systems with correlated disorder", *Physics Reports*, **512**, 125 (2012).

[31] M. Larcher, F. Dalfovo and M. Modugno, "Effects of interaction on the diffusion of atomic matter waves in one-dimensional quasiperiodic potentials", *Physical Review A*, **80**, 053606 (2009).

[32] M. Larcher, M. Modugno and F. Dalfovo, "Localization in momentum space of ultracold atoms in incommensurate lattices", *Physical Review A*, **83**, 013624 (2011).

[33] E. Lucioni, B. Deissler, L. Tanzi, G. Roati, M. Zaccanti, M. Modugno, M. Larcher, F. Dalfovo, M. Inguscio and G. Modugno, "Observation of sub-diffusion in a disordered interacting system", *Physical Review Letters*, **106**, 230403 (2011).

[34] M. Larcher, T. Laptyeva, J. Bodyfelt, F. Dalfovo, M. Modugno and S. Flach, "Subdiffusion of nonlinear waves in quasiperiodic potentials", *New Journal of Physics*, **14**, 103036 (2012).

[35] M. Larcher, C. Menotti, B. Tanatar and P. Vignolo, "A metal-insulator transition induced by random dipoles", *In Preparation* (2012).

[36] A. Lagendijk, B. van Tiggelen and D. Wiersma, "Fifty years of Anderson localization", *Physics Today*, **62**, 24 (2009).

[37] E. Akkermans and G. Montambaux, *Mesoscopic physics of electrons and photons*, (Cambridge University Press, 2007).

[38] B. Kramer and A. MacKinnon, "Localization: theory and experiment", *Reports on Progress in Physics*, **56**, 1469 (1999).

[39] C. Mueller and D. Delande, "Disorder and interference: localization phenomena", *Les Houches 2009 - Session XCI: Ultracold Gases and Quantum Information* (2010).

[40] N. Ashcroft and N. Mermin, *Solid State Physics*, (Harcourt College Publisher, 1976).

[41] D. Vollhardt and P. Wölfle, "Self-consistent theory of Anderson localization", *Electronic phase transitions*, **1** (1992).

[42] D. Vollhardt and P. Wölfle, "Scaling equations from a self-consistent theory of Anderson localization", *Physical Review Letters*, **48**, 699 (1982).

[43] J. E. Lye, L. Fallani, M. Modugno, D. S. Wiersma, C. Fort and M. Inguscio, "Bose-Einstein Condensate in a Random Potential", *Physical Review Letters*, **95**, 070401 (2005).

[44] D. Clément, A. Varon, M. Hugbart, J. Retter, P. Bouyer, L. Sanchez-Palencia, D. Gangardt, G. Shlyapnikov and A. Aspect, "Suppression of transport of an interacting elongated Bose-Einstein condensate in a random potential", *Physical Review Letters*, **95**, 170409 (2005).

[45] C. Fort, L. Fallani, V. Guarrera, J. Lye, M. Modugno, D. Wiersma and M. Inguscio, "Effect of optical disorder and single defects on the expansion of a Bose-Einstein condensate in a one-dimensional waveguide", *Physical Review Letters*, **95**, 170410 (2005).

[46] L. Sanchez-Palencia, D. Clément, P. Lugan, P. Bouyer and A. Aspect, "Disorder-induced trapping versus Anderson localization in Bose–Einstein condensates expanding in disordered potentials", *New Journal of Physics*, **10**, 045019 (2008).

[47] P. Lugan, A. Aspect, L. Sanchez-Palencia, D. Delande, B. Grémaud, C. Müller and C. Miniatura, "One-dimensional Anderson localization in certain correlated random potentials", *Physical Review A*, **80**, 023605 (2009).

[48] D. Jaksch, C. Bruder, J. Cirac, C. Gardiner and P. Zoller, "Cold bosonic atoms in optical lattices", *Physical Review Letters*, **81**, 3108 (1998).

[49] L. Fallani, J. Lye, V. Guarrera, C. Fort and M. Inguscio, "Ultracold atoms in a disordered crystal of light: Towards a Bose glass", *Physical Review Letters*, **98**, 130404 (2007).

[50] P. Vignolo, Z. Akdeniz and M. Tosi, "The transmittivity of a Bose–Einstein condensate on a lattice: interference from period doubling and the effect of disorder", *Journal of Physics B: Atomic, Molecular and Optical Physics*, **36**, 4535 (2003).

[51] U. Gavish and Y. Castin, "Matter-wave localization in disordered cold atom lattices", *Physical Review Letters*, **95**, 20401 (2005).

[52] I. M. Lifshitz, S. A. Gredeskul and L. A. Pastur, *Introduction to the Theory of Disordered Systems*, (Wiley, New York, 1988).

[53] K. Ishii, "Localization of eigenstates and transport phenomena in the one-dimensional disordered system", *Progress of Theoretical Physics Supplement*, **53**, 77 (1973).

[54] N. Mott and W. Twose, "The theory of impurity conduction", *Advances in Physics*, **10**, 107 (1961).

[55] H. Furstenberg, "Noncommuting random products", *Transactions of the American Mathematical Society*, 377–428 (1963).

[56] V. Oseledec, "A multiplicative ergodic theorem. Lyapunov characteristic numbers for dynamical systems", *Transactions of the Moscow Mathematical Society*, **19**, 197 (1968).

[57] D. Herbert and R. Jones, "Localized states in disordered systems", *Journal of Physics C Solid State Physics*, **4**, 1145 (1971).

[58] D. Thouless, "A relation between the density of states and range of localization for one dimensional random systems", *Journal of Physics C: Solid State Physics*, **5**, 77 (1972).

[59] D. Thouless, R. Balian, R. Maynard and G. Toulouse, "Lectures on Amorphous Systems", *Les Houches 1979 - Session XXXI* (1979).

[60] H. Hu, A. Strybulevych, J. Page, S. Skipetrov and B. van Tiggelen, "Localization of ultrasound in a three-dimensional elastic network", *Nature Physics*, **4**, 945 (2008).

[61] A. Chabanov, M. Stoytchev and A. Genack, "Statistical signatures of photon localization", *Nature*, **404**, 850 (2000).

[62] F. Scheffold, R. Lenke, R. Tweer and G. Maret, "Localization or classical diffusion of light?", *Nature*, **398**, 206 (1999).

[63] M. Störzer, P. Gross, C. Aegerter and G. Maret, "Observation of the Critical Regime Near Anderson Localization of Light", *Physical Review Letters*, **96**, 63904 (2006).

[64] T. Schwartz, G. Bartal, S. Fishman and M. Segev, "Transport and Anderson localization in disordered two-dimensional photonic lattices", *Nature*, **446**, 52 (2007).

[65] Y. Lahini, A. Avidan, F. Pozzi, M. Sorel, R. Morandotti, D. Christodoulides and Y. Silberberg, "Anderson localization and nonlinearity in one-dimensional disordered photonic lattices", *Physical Review Letters*, **100**, 13906 (2008).

[66] Y. Lahini, R. Pugatch, F. Pozzi, M. Sorel, R. Morandotti, N. Davidson and Y. Silberberg, "Observation of a localization transition in quasiperiodic photonic lattices", *Physical Review Letters*, **103**, 13901 (2009).

[67] B. Deissler, M. Zaccanti, G. Roati, C. D'Errico, M. Fattori, M. Modugno, G. Modugno and M. Inguscio, "Delocalization of a disordered bosonic system by repulsive interactions", *Nature Physics*, **6**, 354 (2010).

[68] B. Deissler, E. Lucioni, M. Modugno, G. Roati, L. Tanzi, M. Zaccanti, M. Inguscio and G. Modugno, "Correlation function of weakly interacting bosons in a disordered lattice", *New Journal of Physics*, **13**, 023020 (2011).

[69] C. D'Errico, M. Moratti, E. Lucioni, L. Tanzi, B. Deissler, M. Inguscio, G. Modugno, M. Plenio and F. Caruso, "Quantum diffusion with disorder, noise and interaction", *e-print arXiv:1204.1313* (2012).

[70] S. Kondov, W. McGehee, J. Zirbel and B. DeMarco, "Three-dimensional Anderson localization of ultracold matter", *Science*, **334**, 66 (2011).

[71] F. Jendrzejewski, A. Bernard, K. Mueller, P. Cheinet, V. Josse, M. Piraud, L. Pezzé, L. Sanchez-Palencia, A. Aspect and P. Bouyer, "Three-dimensional localization of ultracold atoms in an optical disordered potential", *Nature Physics*, **8**, 398 (2012).

[72] F. Moore, J. Robinson, C. Bharucha, P. Williams and M. Raizen, "Observation of dynamical localization in atomic momentum transfer: A new testing ground for quantum chaos", *Physical Review Letters*, **73**, 2974 (1994).

[73] F. Moore, J. Robinson, C. Bharucha, B. Sundaram and M. Raizen, "Atom optics realization of the quantum δ-kicked rotor", *Physical Review Letters*, **75**, 4598 (1995).

[74] J. Chabé, G. Lemarié, B. Grémaud, D. Delande, P. Szriftgiser and J. Garreau, "Experimental observation of the Anderson metal-insulator transition with atomic matter waves", *Physical Review Letters*, **101**, 255702 (2008).

[75] G. Lemarié, H. Lignier, D. Delande, P. Szriftgiser and J. Garreau, "Critical state of the Anderson transition: between a metal and an insulator", *Physical Review Letters*, **105**, 90601 (2010).

[76] M. Lopez, J. Clément, P. Szriftgiser, J. Garreau and D. Delande, "Experimental Test of Universality of the Anderson Transition", *Physical Review Letters*, **108**, 95701 (2012).

[77] B. Simon, "Almost periodic Schrödinger operators: a review", *Advances in Applied Mathematics*, **3**, 463 (1982).

[78] H. Hiramoto and M. Kohmoto, "Electronic Spectral and Wavefunction Properties of One-Dimensional Quasiperiodic Systems: a Scaling Approach", *International Journal of Modern Physics B*, **6**, 281 (1992).

[79] H. Hiramoto and S. Abe, "Dynamics of an Electron in Quasiperiodic Systems. II. Harper's Model", *Journal of the Physical Society of Japan*, **57**, 1365 (1988).

[80] H. Hiramoto and S. Abe, "Dynamics of an electron in quasiperiodic systems. I. Fibonacci model", *Journal of the Physical Society of Japan*, **57**, 230 (1988).

[81] D. Shechtman, I. Blech, D. Gratias and J. Cahn, "Metallic phase with long-range orientational order and no translational symmetry", *Physical Review Letters*, **53**, 1951 (1984).

[82] D. Levine and P. J. Steinhardt, "Quasicrystals: A New Class of Ordered Structures", *Physical Review Letters*, **53**, 2477 (1984).

[83] Z. Stadnik, *Physical properties of quasicrystals*, vol. 126, (Springer, 1998).

[84] P. Harper, "Single Band Motion of Conduction Electrons in a Uniform Magnetic Field", *Proceedings of the Physical Society. Section A*, **68**, 874 (1955).

[85] S. Aubry and G. Andrè, "Analyticity breaking and Anderson localization in incommensurate lattices", *Annals of the Israel Physical Society*, **3**, 133 (1980).

[86] M. Kohmoto, L. Kadanoff and C. Tang, "Localization problem in one dimension: Mapping and escape", *Physical Review Letters*, **50**, 1870 (1983).

[87] S. Ostlund, R. Pandit, D. Rand, H. Schellnhuber and E. Siggia, "One-dimensional Schrödinger equation with an almost periodic potential", *Physical Review Letters*, **50**, 1873 (1983).

[88] H. Hiramoto and M. Kohmoto, "Scaling analysis of quasiperiodic systems: Generalized Harper model", *Physical Review B*, **40**, 8225 (1989).

[89] R. B. Diener, G. A. Georgakis, J. Zhong, M. Raizen and Q. Niu, "Transition between extended and localized states in a one-dimensional incommensurate optical lattice", *Physical Review A*, **64**, 033416 (2001).

[90] J. Lye, L. Fallani, C. Fort, V. Guarrera, M. Modugno, D. Wiersma and M. Inguscio, "Effect of interactions on the localization of a Bose-Einstein condensate in a quasiperiodic lattice", *Physical Review A*, **75**, 061603 (2007).

[91] M. Modugno, "Exponential localization in one-dimensional quasi-periodic optical lattices", *New Journal of Physics*, **11**, 033023 (2009).

[92] J. Sokoloff, "Unusual band structure, wave functions and electrical conductance in crystals with incommensurate periodic potentials", *Physics Reports*, **126**, 189 (1985).

[93] S. Jitomirskaya, "Metal-insulator transition for the almost Mathieu operator", *Annals of Mathematics-Second Series*, **150**, 1159 (1999).

[94] M. Albert and P. Leboeuf, "Localization by bichromatic potentials versus Anderson localization", *Physical Review A*, **81**, 013614 (2010).

[95] G. Ingold, A. Wobst, C. Aulbach and P. Hänggi, "Delocalization and Heisenberg's uncertainty relation", *The European Physical Journal B-Condensed Matter and Complex Systems*, **30**, 175 (2002).

[96] C. Tang and M. Kohmoto, "Global scaling properties of the spectrum for a quasiperiodic schrödinger equation", *Physical Review B*, **34**, 2041 (1986).

[97] C. Aulbach, A. Wobst, G. Ingold, P. Hänggi and I. Varga, "Phase-space visualization of a metal–insulator transition", *New Journal of Physics*, **6**, 70 (2004).

[98] M. Pasienski, D. McKay, M. White and B. DeMarco, "A disordered insulator in an optical lattice", *Nature Physics*, **6**, 677 (2010).

[99] T. Paul, P. Schlagheck, P. Leboeuf and N. Pavloff, "Superfluidity versus Anderson localization in a dilute Bose gas", *Physical Review Letters*, **98**, 210602 (2007).

[100] T. Paul, M. Albert, P. Schlagheck, P. Leboeuf and N. Pavloff, "Anderson localization of a weakly interacting one-dimensional Bose gas", *Physical Review A*, **80**, 033615 (2009).

[101] M. Albert, T. Paul, N. Pavloff and P. Leboeuf, "Breakdown of the superfluidity of a matter wave in a random environment", *Physical Review A*, **82**, 11602 (2010).

[102] P. Lugan, D. Clément, P. Bouyer, A. Aspect, M. Lewenstein and L. Sanchez-Palencia, "Ultracold bose gases in 1d disorder: From lifshits glass to bose-einstein condensate", *Physical Review Letters*, **98**, 170403 (2007).

[103] G. Falco, T. Nattermann and V. Pokrovsky, "Localized states and interaction-induced delocalization in Bose gases with quenched disorder", *EPL (Europhysics Letters)*, **85**, 30002 (2009).

[104] L. Fontanesi, M. Wouters and V. Savona, "Superfluid to Bose-glass transition in a 1D weakly interacting Bose gas", *Physical Review Letters*, **103**, 30403 (2009).

[105] L. Fontanesi, M. Wouters and V. Savona, "Mean-field phase diagram of the one-dimensional Bose gas in a disorder potential", *Physical Review A*, **81**, 053603 (2010).

[106] I. Aleiner, B. Altshuler and G. Shlyapnikov, "A finite-temperature phase transition for disordered weakly interacting bosons in one dimension", *Nature Physics*, **6**, 900 (2010).

[107] F. Dalfovo, S. Giorgini, L. Pitaevskii and S. Stringari, "Theory of Bose-Einstein condensation in trapped gases", *Reviews of Modern Physics*, **71**, 463 (1999).

[108] C. Pethick and H. Smith, *Bose-Einstein condensation in dilute gases*, (Cambridge university press, 2001).

[109] L. Pitaevskii and S. Stringari, *Bose-einstein condensation*, vol. 116, (Oxford University Press, 2003).

[110] E. Gross, "Structure of a quantized vortex in boson systems", *Il Nuovo Cimento (1955-1965)*, **20**, 454 (1961).

[111] L. Pitaevskii, "Vortex lines in an imperfect Bose gas", *Soviet Physics JETP*, **13**, 451 (1961).

[112] M. Olshanii, "Atomic scattering in the presence of an external confinement and a gas of impenetrable bosons", *Physical Review Letters*, **81**, 938 (1998).

[113] D. Petrov, D. Gangardt and G. Shlyapnikov, "Low-dimensional trapped gases", *Journal de Physique IV (Proceedings)*, **116**, 5 (2004).

[114] A. Trombettoni and A. Smerzi, "Discrete solitons and Breathers with Diluite Bose-Einstein Condensates", *Physical Review Letters*, **100**, 2353 (2001).

[115] T. Anker, M. Albiez, R. Gati, S. Hunsmann, B. Eiermann, A. Trombettoni and M. Oberthaler, "Nonlinear self-trapping of matter waves in periodic potentials", *Physical Review Letters*, **94**, 20403 (2005).

[116] M. Johansson, M. Hörnquist and R. Riklund, "Effects of nonlinearity on the time evolution of single-site localized states in periodic and aperiodic discrete systems", *Physical Review B*, **52**, 231 (1995).

[117] M. Rosenkranz, D. Jaksch, F. Lim and W. Bao, "Self-trapping of Bose-Einstein condensates expanding into shallow optical lattices", *Physical Review A*, **77**, 063607 (2008).

[118] A. Smerzi, S. Fantoni, S. Giovanazzi and S. Shenoy, "Quantum Coherent Atomic Tunneling between Two Trapped Bose-Einstein Condensates", *Physical Review Letters*, **79**, 4950 (1997).

[119] S. Raghavan, A. Smerzi, S. Fantoni and S. Shenoy, "Coherent oscillations between two weakly coupled Bose-Einstein condensates: Josephson effects, π oscillations, and macroscopic quantum self-trapping", *Physical Review A*, **59**, 620 (1999).

[120] F. Meier and W. Zwerger, "Josephson tunneling between weakly interacting Bose-Einstein condensates", *Physical Review A*, **64**, 033610 (2001).

[121] M. Albiez, R. Gati, J. Fölling, S. Hunsmann, M. Cristiani and M. Oberthaler, "Direct observation of tunneling and nonlinear self-trapping in a single bosonic Josephson junction", *Physical Review Letters*, **95**, 10402 (2005).

[122] S. Levy, E. Lahoud, I. Shomroni and J. Steinhauer, "The ac and dc Josephson effects in a Bose–Einstein condensate", *Nature*, **449**, 579 (2007).

[123] G. Kopidakis, S. Komineas, S. Flach and S. Aubry, "Absence of Wave Packet Diffusion in Disordered Nonlinear Systems", *Physical Review Letters*, **100**, 84103 (2008).

[124] G. Ng and T. Kottos, "Wavepacket dynamics of the nonlinear Harper model", *Physical Review B*, **75**, 205120 (2007).

[125] Z. Zhang, P. Tong, J. Gong and B. Li, "Wave packet dynamics in one-dimensional linear and nonlinear generalized Fibonacci lattices", *Physical Review E*, **83**, 056205 (2011).

[126] S. Flach, D. Krimer and C. Skokos, "Universal spreading of wave packets in disordered nonlinear systems", *Physical Review Letters*, **102**, 24101 (2009).

[127] A. Pikovsky and D. Shepelyansky, "Destruction of Anderson Localization by a Weak Nonlinearity", *Physical Review Letters*, **100**, 94101 (2008).

[128] I. García-Mata and D. Shepelyansky, "Delocalization induced by nonlinearity in systems with disorder", *Physical Review E*, **79**, 026205 (2009).

[129] C. Skokos, D. Krimer, S. Komineas and S. Flach, "Delocalization of wave packets in disordered nonlinear chains", *Physical Review E*, **79**, 056211 (2009).

[130] S. Flach, "Spreading of waves in nonlinear disordered media", *Chemical Physics*, **375**, 548 (2010).

[131] T. Laptyeva, J. Bodyfelt, D. Krimer, C. Skokos and S. Flach, "The crossover from strong to weak chaos for nonlinear waves in disordered systems", *EPL (Europhysics Letters)*, **91**, 30001 (2010).

[132] J. Bodyfelt, T. Laptyeva, C. Skokos, D. Krimer and S. Flach, "Nonlinear waves in disordered chains: Probing the limits of chaos and spreading", *Physical Review E*, **84**, 016205 (2011).

[133] W. Zwerger, "Mott–Hubbard transition of cold atoms in optical lattices", *Journal of Optics B: Quantum and Semiclassical Optics*, **5**, S9 (2003).

[134] F. Gerbier, A. Widera, S. Fölling, O. Mandel, T. Gericke and I. Bloch, "Interference pattern and visibility of a Mott insulator", *Physical Review A*, **72**, 53606 (2005).

[135] H. Veksler, Y. Krivolapov and S. Fishman, "Spreading for the generalized nonlinear Schrödinger equation with disorder", *Physical Review E*, **80**, 037201 (2009).

[136] C. Skokos and S. Flach, "Spreading of wave packets in disordered systems with tunable nonlinearity", *Physical Review E*, **82**, 016208 (2010).

[137] J. Bodyfelt, T. Kottos and B. Shapiro, "One-Parameter Scaling Theory for Stationary States of Disordered Nonlinear Systems", *Physical Review Letters*, **104**, 164102 (2010).

[138] D. Krimer and S. Flach, "Statistics of wave interactions in nonlinear disordered systems", *Physical Review E*, **82**, 046221 (2010).

[139] E. Michaely and S. Fishman, "Effective noise theory for the nonlinear Schrödinger equation with disorder", *Physical Review E*, **85**, 046218 (2012).

[140] T. Laptyeva, J. Bodyfelt and S. Flach, "Do nonlinear waves in random media follow nonlinear diffusion equations?", *e-print arXiv:1206.6085* (2012).

[141] S. Fishman, Y. Krivolapov and A. Soffer, "Perturbation theory for the nonlinear Schrödinger equation with a random potential", *Nonlinearity*, **22**, 2861 (2009).

[142] J. Laskar and P. Robutel, "High order symplectic integrators for perturbed Hamiltonian systems", *Celestial Mechanics and Dynamical Astronomy*, **80**, 39 (2001).

[143] Y. Castin and R. Dum, "Instability and depletion of an excited Bose-Einstein condensate in a trap", *Physical Review Letters*, **79**, 3553 (1997).

[144] S. Gardiner, D. Jaksch, R. Dum, J. Cirac and P. Zoller, "Nonlinear matter wave dynamics with a chaotic potential", *Physical Review A*, **62**, 023612 (2000).

[145] C. Weiss and N. Teichmann, "Differences between mean-field dynamics and N-particle quantum dynamics as a signature of entanglement", *Physical Review Letters*, **100**, 140408 (2008).

[146] J. Reslen, C. Creffield and T. Monteiro, "Dynamical instability in kicked Bose-Einstein condensates", *Physical Review A*, **77**, 043621 (2008).

[147] I. Březinová, L. Collins, K. Ludwig, B. Schneider and J. Burgdörfer, "Wave chaos in the nonequilibrium dynamics of the Gross-Pitaevskii equation", *Physical Review A*, **83**, 043611 (2011).

[148] M. Heimsoth, C. Creffield, L. Carr and F. Sols, "Orbital Josephson effect and interactions in driven atom condensates on a ring", *New Journal of Physics*, **14**, 075023 (2012).

[149] I. Březinová, A. Lode, A. Streltsov, O. Alon, L. Cederbaum and J. Burgdörfer, "Wave chaos as signature for depletion of a Bose-Einstein condensate", *Physical Review A*, **86**, 013630 (2012).

[150] A. Ovchinnikov, N. Erikhman and K. Pronin, *Vibrational-Rotational Excitations in Nonlinear Molecular Systems*, (Springer, 2001).

[151] Y. Kivshar and M. Peyrard, "Modulational instabilities in discrete lattices", *Physical Review A*, **46**, 3198 (1992).

[152] Y. Kivshar, "Localized modes in a chain with nonlinear on-site potential", *Physics Letters A*, **173**, 172 (1993).

[153] M. Johansson, "Discrete nonlinear Schrödinger approximation of a mixed Klein–Gordon/Fermi–Pasta–Ulam chain: Modulational instability and a statistical condition for creation of thermodynamic breathers", *Physica D: Nonlinear Phenomena*, **216**, 62 (2006).

[154] V. Bellani, E. Diez, R. Hey, L. Toni, L. Tarricone, G. Parravicini, F. Domínguez-Adame and R. Gómez-Alcalá, "Experimental evidence of delocalized states in random dimer superlattices", *Physical Review Letters*, **82**, 2159 (1999).

[155] U. Kuhl, F. M. Izrailev and A. A. Krokhin, "Enhancement of Localization in One-Dimensional Random Potentials with Long-Range Correlations", *Physical Review Letters*, **100**, 126402 (2008).

[156] L. Sanchez-Palencia, D. Clément, P. Lugan, P. Bouyer, G. Shlyapnikov and A. Aspect, "Anderson localization of expanding Bose-Einstein condensates in random potentials", *Physical Review Letters*, **98**, 210401 (2007).

[157] J. Flores, "Transport in models with correlated diagonal and off-diagonal disorder", *Journal of Physics Condensed Matter*, **1**, 8471 (1989).

[158] D. H. Dunlap, H.-L. Wu and P. W. Phillips, "Absence of localization in a random-dimer model", *Physical Review Letters*, **65**, 88 (1990).

[159] J. Schaff, Z. Akdeniz and P. Vignolo, "Localization-delocalization transition in the random dimer model", *Physical Review A*, **81**, 041604 (2010).

[160] F. Izrailev and A. Krokhin, "Localization and the mobility edge in one-dimensional potentials with correlated disorder", *Physical Review Letters*, **82**, 4062 (1999).

[161] L. Tessieri, "Delocalization phenomena in one-dimensional models with long-range correlated disorder: a perturbative approach", *Journal of Physics A: Mathematical and General*, **35**, 9585 (2002).

[162] E. Gurevich and O. Kenneth, "Lyapunov exponent for the laser speckle potential: A weak disorder expansion", *Physical Review A*, **79**, 063617 (2009).

[163] C. A., C. P. and S. M., "Anderson localization in 1D systems with correlated disorder", *European Physical Journal B*, **82**, 107 (2011).

[164] F. de Moura and M. Lyra, "Correlation-induced metal-insulator transition in the one-dimensional Anderson model", *Physica A: Statistical Mechanics and its Applications*, **266**, 465 (1999).

[165] J. Kantelhardt, S. Russ, A. Bunde, S. Havlin and I. Webman, "Comment on: Delocalization in the 1D Anderson Model with Long-Range Correlated Disorder", *Physical Review Letters*, **84**, 198 (2000).

[166] F. de Moura and M. Lyra, "de Moura and Lyra reply on: Delocalization in the 1D Anderson Model with Long-Range Correlated Disorder", *Physical Review Letters*, **84**, 199 (2000).

[167] A. M. García-García and E. Cuevas, "Differentiable potentials and metallic states in disordered one-dimensional systems", *Physical Review B*, **79**, 073104 (2009).

[168] C. Menotti, M. Lewenstein, T. Lahaye, T. Pfau *et al.*, "Dipolar interaction in ultra-cold atomic gases", in "AIP Conference Proceedings", vol. 970 (2008).

[169] T. Lahaye, C. Menotti, L. Santos, M. Lewenstein and T. Pfau, "The physics of dipolar bosonic quantum gases", *Reports on Progress in Physics*, **72**, 126401 (2009).

[170] A. Griesmaier, J. Werner, S. Hensler, J. Stuhler and T. Pfau, "Bose-Einstein condensation of chromium", *Physical Review Letters*, **94**, 160401 (2005).

[171] Q. Beaufils, R. Chicireanu, T. Zanon, B. Laburthe-Tolra, E. Maréchal, L. Vernac, J. Keller and O. Gorceix, "All-optical production of chromium Bose-Einstein condensates", *Physical Review A*, **77**, 061601 (2008).

[172] M. Lu, N. Burdick, S. Youn and B. Lev, "Strongly dipolar Bose-Einstein condensate of dysprosium", *Physical Review Letters*, **107**, 190401 (2011).

[173] M. Lu, N. Burdick and B. Lev, "Quantum degenerate dipolar Fermi gas", *Physical Review Letters*, **108**, 215301 (2012).

[174] K. Aikawa, A. Frisch, M. Mark, S. Baier, A. Rietzler, R. Grimm and F. Ferlaino, "Bose-Einstein Condensation of Erbium", *Physical Review Letters*, **108**, 210401 (2012).

[175] T. Koch, T. Lahaye, J. Metz, A. G. B. Fröhlich and T. Pfau, "Stabilization of a purely dipolar quantum gas against collapse", *Nature Physics*, **4**, 218 (2008).

[176] S. Sinha and L. Santos, "Cold dipolar gases in quasi-one-dimensional geometries", *Physical Review Letters*, **99**, 140406 (2007).

[177] R. Farchioni, G. Grosso and G. Parravicini, "Electronic structure in incommensurate potentials obtained using a numerically accurate renormalization scheme", *Physical Review B*, **45**, 6383 (1992).

[178] J. M. Luck, "Cantor spectra and scaling of gap widths in deterministic aperiodic systems", *Physical Review B*, **39**, 5834 (1989).

[179] M. Robert-De-Saint-Vincent, J. Brantut, B. Allard, T. Plisson, L. Pezzé, L. Sanchez-Palencia, A. Aspect, T. Bourdel and P. Bouyer, "Anisotropic 2d diffusive expansion of ultracold atoms in a disordered potential", *Physical Review Letters*, **104**, 220602 (2010).

[180] F. Jendrzejewski, K. Müller, J. Richard, A. Date, T. Plisson, P. Bouyer, A. Aspect and V. Josse, "Coherent Backscattering of Ultracold Atoms", *Physical Review Letters*, **109**, 195302 (2012).

[181] W. Kohn, "Analytic properties of Bloch waves and Wannier functions", *Physical Review*, **115**, 809 (1959).

[182] R. Graft, D. Lohrmann, G. Parravicini and L. Resca, "Renormalization formalism in the theory of the electronic structure of superlattices: Application to silicon superlattices", *Physical Review B*, **36**, 4782 (1987).

[183] P. Giannozzi, G. Grosso and G. Parravicini, "Theory of electronic states in lattices and superlattices", *La Rivista del Nuovo Cimento (1978-1999)*, **13**, 1 (1990).

[184] H. Aoki, "Real-space renormalization-group theory for Anderson localization: Decimation method for electron systems", *Journal of Physics C*, **13**, 3369 (1980).

[185] G. Grosso and G. Pastori Parravicini, "Memory Function Methods in Solid State Physics", *Advances in Chemical Physics: Memory Function Approaches to Stochastic Problems in Condensed Matter*, **62**, 133 (2007).

[186] P. Kirkman and J. Pendry, "The statistics of one-dimensional resistances", *Journal of Physics C Solid State Physics*, **17**, 4327 (1984).

[187] E. Economou, *Green's functions in quantum physics*, vol. 7, (Springer Berlin, 1979).